MULTI-RESOLUTION STUDY OF TOPOGRAPHICAL AND ZONAL PROPERTIES OF OSTEOARTHRITIS IN ARTICULAR CARTILAGE USING MICROSCOPIC MRI AND POLARIZED LIGHT MICROSCOPY

by

FARID-AHMED WAJIHUDDIN BADAR

A dissertation submitted in partial fulfillment of the
requirements for the degree of

DOCTOR OF PHILOSOPHY IN BIOMEDICAL SCIENCES: MEDICAL PHYSICS

2022

Oakland University
Rochester, Michigan

Doctoral Advisory Committee:

Yang Xia, Ph.D., Chair
Bradley J. Roth, Ph.D.
Evgeniy Khain, Ph.D.
Quan Jiang, Ph.D.
Susan M. Bowyer, Ph.D.

Dedicated to

My late mother, Firoza, whose prayers have always been with me.

My ever-supporting father, Wazir, who has always been secretly proud.

My loving wife, Hina, whose love, affection and encouragement has held me through it all.

My courageous and genius daughter, Zara, who will one day write her own book.

ACKNOWLEDGMENTS

This research was conducted in the Department of Physics, Oakland University, Rochester, MI. I give my greatest gratitude to my advisor and mentor, Yang Xia Ph.D., for his most valuable and continual professional support. I thank the members of my Doctoral Dissertation Committee, Bradley Roth Ph.D., Evgeniy Khain Ph.D., Quan Jiang Ph.D., and Susan Bowyer Ph.D. for their consistent support and guidance. I thank James Ewing Ph.D. and Gary Ding Ph.D. at Henry Ford Hospital (Detroit, MI) for aiding in the use of the small-animal 7T MRI, and John Matyas Ph.D. at the University of Calgary for providing the ACL transected osteoarthritic canine joints for this project. During my study, I had the privilege to work with several postdocs, graduate, and undergraduate students in the lab. In particular, I would like to thank two postdocs in the lab, Shaokuan Zheng Ph.D., and Nian Wang Ph.D., for their expertise in μMRI and imaging. I thank my fellow graduate students, Ji Hyun Lee Ph.D., Daniel Mittelstaedt Ph.D., and David Kahn Ph.D., whom I worked closely with on this project. I express my gratitude to the faculty and staff in the Physics Department who helped me over the years. I acknowledge the journals for permission to reproduce my publications in this dissertation. Finally, I wish to thank the financial support from the National Institutes of Health (NIH, AR 045172, AR 052353) and the Research Excellence Fund in Biotechnology from Oakland University, which enabled this cartilage research at Oakland University.

Farid-Ahmed Wajihuddin Badar

ABSTRACT

MULTI-RESOLUTION STUDY OF TOPOGRAPHICAL AND ZONAL PROPERTIES OF OSTEOARTHRITIS IN ARTICULAR CARTILAGE USING MICROSCOPIC MRI AND POLARIZED LIGHT MICROSCOPY

by

Farid-Ahmed Wajihuddin Badar

Advisor: Yang Xia, Ph.D.

Articular cartilage is a thin layer of connective tissue found in diarthrodial joints that overlay the opposing ends of bones and acts as lubricating surfaces to distribute stress and reduce friction with the help of synovial fluid. Hyaline cartilage contains an abundance of water molecules that are essential to the behavior and function of cartilage, the negatively charged proteoglycans that influence the biomechanical properties of the tissue, and the collagen fibers that act as the rebar or reinforcement bars to preserve the structural integrity of the tissue. Cartilage supports the applied load and distributes stress based on its intrinsic material properties, together with its underlying bone. At different surface locations of any single diarthrodial joint, the properties of cartilage are prone to have many morphological and molecular variations topographically, which are mainly due to the patterns of mechanical loading for any specific joint. Any change in the morphological and molecular properties of the cartilage and bone is likely to directly impact the clinical diagnoses of joint diseases such as osteoarthritis (OA).

In addition to the topographical variations, cartilage also has a number of depth-dependent variations over its thin thickness, which begins in the non-calcified cartilage

with articular laminae and the unequal thickness of sub-tissue zones. Conceptually, the non-calcified cartilage is commonly subdivided based on the orientations of collagen fibers and chondrocytes, into three histological zones. They are the superficial (SZ), transitional (TZ), and radial (RZ) zones. The non-calcified cartilage interfaces with the calcified cartilage and subchondral bone plate (SBP) through the tidemark (TM).

This dissertation has seven chapters, which describe a number of multi-resolution projects that use high-resolution imaging to determine the topographical and depth-dependent variations in cartilage, in order to diagnose OA at its earliest stages. The dissertation begins with a brief introduction of background and literature review (Chapters 1-2), continues with the description of the materials and methods (Chapter 3), and summarizes three published peer-reviewed journal articles (Chapters 4-6). The dissertation ends with a summary and comments on future directions (Chapter 7).

Among the three research projects described in this dissertation, the first project (Chapter 4) investigates the improvement in the OA detection in cartilage by the interpolation of T2 images, in the situation when the native MRI resolution is insufficient to resolve the depth-dependent T2 characteristics in articular cartilage. The second project (Chapter 5) establishes the topographical and zonal T2 patterns of multi-resolution MRI in medial tibial cartilage in a canine model of OA, initiated by anterior cruciate ligament (ACL) transection surgery, which was studied after 8-weeks and 12-weeks post-surgery. The third project (Chapter 6) quantifies the interface region between the non-calcified cartilage and the subchondral bone plate, which includes the deep portion of the non-calcified articular cartilage and the zone of calcified cartilage (ZCC) using a dual-modality microscopic imaging study.

TABLE OF CONTENTS

TABLE OF CONTENTS—Continued

TABLE OF CONTENTS—Continued

LIST OF TABLES

LIST OF FIGURES

LIST OF ABBREVIATIONS

AC	Articular cartilage
ACL	Anterior cruciate ligament
AMT	Anterior medial tibia
AS	Articular Surface
AZ	Azimuth, collagen fiber orientation (deg^{o})
B_0	Magnetic field
C	Meniscus-covered area
CMT	Central medial tibia
CPMG	Carr-Purcell-Meiboom-Gill Sequence
CT	Computed tomography
dGEMRIC	Delayed gadolinium-enhanced MRI of cartilage
ECM	Extracellular matrix
EMT	Exterior medial tibia
FCD	Fixed charge density
FID	Free induction decay
FTIRI	Fourier-transform infrared imaging
GAG	Glycosaminoglycan
Gd-DTPA	Gadopentetate Dimeglumine (Magnevist ®)
GE	Gradient echo sequence
IMT	Interior medial tibia
MRI	Magnetic Resonance Imaging

mMRI	macro-MRI
MSME	multi-slice multi-echo
N	Normal (healthy) tissue
NMR	Nuclear magnetic resonance
OA	Osteoarthritis
PG	Proteoglycan
PLM	Polarized light microscopy
PMT	Posterior medial tibia
R	Relaxivity
Ret	Retardation, collagen fiber organization (nm)
RF	Radio frequency
RZ	Radial zone
RZI	Upper radial zone
RZII	Lower radial zone
SBP	Subchondral Bone Plate
S.E.	Standard Error
SNR	Signal-to-noise ratio
SPECT	Single photon emission computed tomography
SPGR	Spoiled gradient-recalled echo
SZ	Superficial zone
T1	The spin-lattice (longitudinal) relaxation

T2	The spin-spin (transverse) relaxation
TM	Tidemark
TR	Repetition Time
TZ	Transitional zone
UTE	Ultra-short echo time sequence
ZCC	Zone of Calcified Cartilage
μMRI	micro-MRI
2D	2 dimensions
8C	8-weeks contralateral
8OA	8-weeks OA
12C	12-weeks contralateral
12OA	12-weeks OA

CHAPTER ONE

INTRODUCTION

The term “articular cartilage” and the pathology of the cartilage disease were first described in a 1743 scientific publication by William Hunter, in which he described the avascular and aneural tissue as “universally allowed to be a very troublesome disease; that it admits of a cure with more difficulty than carious bone; and that, then destroyed, it is never recovered” (Hunter, 1743). This finding still holds true, after nearly two hundred and seventy nine years, where the scientific research community studying osteoarthritis (OA) still struggles in finding effective methods of early detection and non-invasive cure of the disease (Collins, Hart, & Mills, 2019). In a recent report, the Centers for Disease Control and Prevention (CDC) has reported that 1 in 7 adults has osteoarthritis ("United States Bone and Joint Initiative: The Burden of Musculoskeletal Diseases in the United States (BMUS)," 2020). This debilitating disease thus affects around 18.7 million people in the working age group, which puts a large strain on the economy, an annual medical cost around 65.5 billion dollars due to various cartilage diseases (Barbour, Helmick, Boring, & Brady, 2017). Hence, there is a great importance and urgency in the measurement of the structural and compositional property changes in articular cartilage, in order to detect the early signs of osteoarthritis for clinical diagnosis and reversible preventive care.

Articular cartilage is a heterogeneous tissue crucial for the functionality and mobility of a diarthrodial joint (Buckwalter, Mankin, & Grodzinsky, 2005; Maroudas, 1979; Zernia & Huster, 2006). It provides a smooth bearing surface with low net friction

allowing for free motion of joint and maintenance of mechanical stress and strain without any long-term deformation. Morphologically, cartilage is a thin layer of soft tissue covering the ends-of-joints. The tissue contains a small number of chondrocytes (cells), and an extensive extracellular matrix that is mainly comprised of collagen fibrils, negatively charged proteoglycans, and water (Ficat & Maroudas, 1975; Venn & Maroudas, 1977). Along its thin thickness (depth), cartilage is commonly subdivided into three histological zones, which starts with a layer of finely packed fibers called the lamina and the superficial zone (SZ) in which the collagen fibers are aligned parallel to the tissue surface. The collagen fibers within the tissue below the SZ change their orientation rather randomly, appropriately labelled as the transitional zone (TZ). The tissue ends with relatively thicker fibers that are aligned perpendicular to the tissue surface in the radial or deep zone (RZ) whose ends are bound into the cartilage-bone interface (i.e. tidemark) and a relatively thin layer of calcified cartilage below the RZ (Benninghoff, 1925; Buckwalter & Mankin, 1998b; Xia, 2008).

Many morphological changes that arise in any of these zones are early signs of cartilage degradation, which causes the tissue to further lose its load-bearing ability. Such degradation in cartilage eventually leads to the most common degenerative joint disease, called osteoarthritis (Spandonis, Heese, & Hall, 2004; Turkiewicz et al., 2014). The most investigated and commonly found OA is in the tibiofemoral joint (knee joint) where the tibial joint surface can have varying amounts of concentrations and interactions among the molecular constituents and have complex topographical variations at different surface locations, even just a few millimeters apart (Brama et al., 2009; Jurvelin, Arokoski, Hunziker, & Helminen, 2000; Weiss, Rosenberg, & Helfet, 1968; Xia, 2000a; Xia,

Moody, Alhadlaq, & Hu, 2003). Subtle modifications to the molecular environment and ultrastructure in cartilage eventually leads to OA (Armstrong & Mow, 1982; Buckwalter & Martin, 1995).

Radiographic tools, such as X-ray or computer tomography (CT), can at best detect late or advanced stages of OA, due to their insensitivity to the water molecules and proteins in cartilage (Buckland-Wright, Macfarlane, Williams, & Ward, 1995; Hunter et al., 2015; Ley, Bjornsdottir, Ekman, Boyde, & Hansson, 2016; Vignon et al., 2003). In contrast, magnetic resonance imaging (MRI) is one of the few diagnostic tools that can assess the integrity of articular cartilage without any invasive methods, due to its excellent sensitivity to the dynamic environment of water molecules in the tissue. MRI has been used extensively in various musculoskeletal systems for clinical and research-based diagnosis of morphological and molecular changes. Being non-invasive and sensitive to the motions of water molecules, MRI has the undisputable potential to become the leading diagnostic tool for cartilage health (Choi & Gold, 2011; Conaghan, 2006; Huang & Schweitzer, 2014; Matzat, Van Tiel, Gold, & Oei, 2013; Mosher, Walker, Petscavage-Thomas, & Guermazi, 2013; Nemec et al., 2011; Pakin, Cavalcanti, La Rocca, Schweitzer, & Regatte, 2006; Wang, Teichtahl, & Cicuttini, 2016; Wang, Wang, Deng, Liu, & Ling, 2015). Several MRI protocols such as T2 (T2 anisotropy), T1ρ, T1 with the use of contrast agents, and diffusion can in principle detect the changes in cartilage health due to the development of musculoskeletal diseases, osteoarthritis in particular (Alhadlaq, Xia, Moody, & Matyas, 2004; Binks et al., 2013; Matzat, Kogan, Fong, & Gold, 2014; Newbould, Miller, Tielbeek, et al., 2012; Regatte, Akella, Lonner, Kneeland, & Reddy, 2006; Smith et al., 2001; Welsch et al., 2008).

The clinical method of OA detection using different MRI protocols, however, still requires further improvement and statistical justification. A major cause of this insufficient diagnostic ability is the relatively large voxel size in clinical MRI, in comparison with the relatively thin thickness of cartilage over which there is notable change in the molecular concentration and fiber orientation (Xia, 2007). Consequently, many properties that change naturally in the tissue, such as topographical distributions of the collagen orientation and proteoglycan concentration, can mask the changes in cartilage caused by the degradation processes when the MRI resolution is insufficient (Badar & Xia, 2017; Greaves, Gilbart, Yung, Kozlowski, & Wilson, 2009; Pakin et al., 2006; Regatte & Schweitzer, 2007; Wyatt et al., 2015). With the implementation of the knowledge gathered by many animal studies including this dissertation, we aim to contribute to the improvement of clinical MRI for the early detection of osteoarthritis.

1.1 Specific Aims

In this dissertation, several multi-resolution studies of osteoarthritic cartilage in canines were carried out to demonstrate the required resolution and the importance of topographical variations in the detection of early-stage osteoarthritis. To mimic the clinical MRI setting for the diagnosis of osteoarthritis, a large-bore-size magnet for animal MRI was also used in order to correlate the whole-joint MRI properties with the microscopic MRI (μMRI) properties measured from smaller cartilage-bone specimens in our own lab. Quantitative T2 data was collected from five sites over the medial tibia to build a topographical map of the disease progression, which considered the measurement of zonal variations. Statistical analysis was carried out to detect the differences in the topographical and zonal changes in cartilage across the medial tibial plateau from the

early to late-stages of osteoarthritis, using the Pond-Nuki model (Pond & Nuki, 1973) of ACL transection on a canine joint. μMRI and polarized light microscopy (PLM) were also used in this dissertation to determine the quantitative measure of T2 anisotropy in the calcified region of articular cartilage.

The specific objectives of the studies were as follows

1. To investigate the improvement in the detection of osteoarthritis in cartilage by the interpolation of T2 changes in the situation when the MRI resolution is insufficient to resolve the depth dependent T2 characteristics, with unequal division of tissue thickness. (Badar & Xia, 2017)
2. To evaluate the topographical and depth-dependent properties (T2) from the early- and late-stages of OA in canine articular cartilage over the medial tibial plateau using low- and high-resolution MRI (Badar, Lee, Qu, & Xia, 2021).
3. To investigate the dipolar interaction in the zone of calcified cartilage of a healthy canine humeral joint using the ultra-short echo (UTE) sequence in μMRI and correlating with optical retardation and azimuth with the use of PLM. (Badar & Xia, 2021)

1.2 Organization of the Dissertation

This dissertation is divided into seven chapters. Since a chapter represents an individual paper published in a journal, there is some repetition between the texts in these chapters.

Chapter 2 details the background of articular cartilage, clinical imaging of cartilage with osteoarthritis, and preclinical imaging tools for articular cartilage.

Chapter 3 is an overview of the materials and methods used in these studies of osteoarthritic cartilage. Section 3.1 describes the two 7T MRI systems used for the study and the application of image interpolation to improve the measurement of OA; section 3.2 describes the method of site and region-based disease progression analysis for the detection of OA progression; and section 3.3 describes the use of different MRI sequences to measure T2 anisotropy in the non-calcified and calcified cartilage. Polarized light microscopy was used to verify the quantitative measure of μMRI.

Chapter 4 describes how to improve the definition of zonal division in clinical like low-resolution MRI to accurately measure early-stage OA. With the aid of clinical like settings in an animal-whole-body MRI, this study was able to define the zonal tissue changes in articular cartilage at the least adequate resolution to study the changes due to OA. This result has been published in *Quantitative Imaging in Medicine and Surgery* (Badar & Xia, 2017)

Chapter 5 evaluates the osteoarthritic progression of articular cartilage over the canine medial tibia as a function of low- and high-resolution MRI. Using quantitative T2 data from gradient echo and spin echo sequences respectively, across five topographical locations across the medial tibia and four histological zonal sections of the articular cartilage. The T2 data was used to compare the progression of OA across four stages of osteoarthritis to healthy knee joints. Complex relationships were found in the tissue properties as a function of disease progression based on the topographical and zonal properties of the tissues. This study was the first quantitative and highest multi-resolution characterization of cartilage at five topographical locations over the medial tibial plateau with fine zonal resolution in an animal model of OA, which would benefit future

investigations of human OA in clinical settings. This study has been published recently in *Magnetic Resonance Imaging* (Badar et al., 2021).

Chapters 6 is a dual-modality microscopic imaging study that quantified the interface region between the non-calcified cartilage and the subchondral bone plate. The magic angle effect in the deep region of the non-calcified cartilage as well as the zone of calcified cartilage in μMRI is analyzed, which was further supported by quantitative polarized light microscopy. With an enhanced understanding of the tissue properties in this interface region, it will potentially be possible to monitor the changes that are instrumental to the initiation and development of osteoarthritis and other joint diseases. This work has been published in *Microscopy Research & Technique* (Badar & Xia, 2021).

Chapter 7 summarizes the dissertation and provides further discussions on future directions for ongoing research.

CHAPTER TWO

BACKGROUND

In this chapter, the backgrounds of osteoarthritic cartilage and experimental setups of cartilage imaging are discussed. It begins with the description of the morphology and structural aspects of articular cartilage that make it a unique system in mammalian joints. The chapter then introduces the fundamentals of MRI, microscopic MRI, and the application of MRI to articular cartilage. The magic angle effect and its implications to cartilage MRI are discussed. The final section of this chapter discusses PLM, together with its application to articular cartilage and the correlation between PLM and MRI.

2.1 Articular Cartilage

Articular cartilage is a connective tissue found in various diarthrodial joints in animals and human. Cartilage acts as an interface between the ends of bones to form the skeletal framework that supports the body as a whole (Buckwalter et al., 2005; Maroudas, 1979). The smooth and frictionless motion in joints is due to the properties of articular cartilage together with the viscous fluid in the joint cavity called synovial fluid (Mankin & Buckwalter, 1996). Since mature cartilage is avascular and aneural, the delivery of nutrients and the removal of metabolic wastes in cartilage are highly dependent upon the presence of the synovial fluid (Hall, Horwitz, & Wilkins, 1996; Mankin, 1994), via passive diffusion as well as active loading/unloading activities.

There are three distinct cartilage types: hyaline, named from the Latin word “hyalinus” which translates as “smooth” or “glass-like”, which is the most abundant type

of cartilage in the body (Gray, Burstein, Lesperance, & Gehrke, 1995); fibrocartilage, which can be found in intervertebral discs of the spine, the menisci of the knee, and on the opposing surfaces of bones with immovable joints (Benjamin & Evans, 1990; Gray et al., 1995); and elastic cartilage which is much like hyaline cartilage however has stretchable properties found in vocal chords in the larynx and forming parts of the ear. The focus for this study is the properties of hyaline cartilage which will be discussed further in detail in the rest of this dissertation.

2.1.1 Extracellular Matrix

Hyaline cartilage consists of a small number of chondrocytes (cells) embedded in an extensive extracellular matrix (ECM), which contains mainly water, collagen fibers and proteoglycans. The extracellular matrix of cartilage (Figure 2.1) provides the structural and physiological environment for the living chondrocytes. The water and macromolecules in ECM are synthesized and maintained by the cellular component of the tissue (Buckwalter & Mankin, 1998a). On a compositional level, the major components of the ECM are water (65-80% of the wet weight (w.w.)), collagen (~15% w.w.), and proteoglycans (PG) (~5% w.w.) (Ficat & Maroudas, 1975; Maroudas, Bayliss, & Venn, 1980; Maroudas & Venn, 1977; Venn & Maroudas, 1977). Chondrocytes are about 2% in weight/volume.

2.1.1.1 Water

Water is the most abundant component of the ECM, which has a depth dependent variation on a morphological scale, with its highest concentration at the articular surface that gradually decreases with the depth, until the lowest concentration at the calcified region. As a key contributor to the biomechanical properties of articular cartilage, water

provides hydro-like pressure that protects the structural integrity of cartilage under repetitive loading and shear forces. Most of the water molecules in healthy cartilage can be said to be able to move around relatively "freely" in the ECM, serving as a medium for the exchange of nutrients and waste between the cells and the synovial fluid. A small percentage of water can be said to be "bound" with the collagen molecules, which plays an important role in the structural organization of the collagen-proteoglycan network in the ECM (Torzilli, Rose, & Dethmers, 1982). The total water present in the ECM depends on the fixed-charge density and the organization of the collagen-proteoglycan matrix (Basser, Schneiderman, Bank, Wachtel, & Maroudas, 1998). In addition, water provides the ECM with its viscoelastic properties and maintains its shape and size-reversible properties (Buckwalter & Mankin, 1998a; Maroudas, Wachtel, Grushko, Katz, & Weinberg, 1991).

2.1.1.2 Collagen

Collagen, a protein, is the major macromolecular component of many connective tissues (e.g., cartilage, tendon, meniscus, skin, and blood vessels of most mammals). Cartilage can have several different types of collagen, with 80% to 90% of the total collagen being the type II fibers (Huber, Trattnig, & Lintner, 2000), which has a triple helix structure with three polypeptide chains (Eyre, 1991). The collagen fibers resist tensile loads, bind PGs, and withstand the swelling pressure (Maroudas, 1976). Morphologically, the collagen fibers in articular cartilage form a 3D organizational network, which gives the tissue along the depth its distinctive zonal structure. The integrity of the collagen matrix is critical to the balance between the fluid and solid components of tissue for its healthy function.

Defined by the orientation of the collagen fibers within a healthy non-calcified cartilage, the tissue is commonly subdivided into three distinct structural zones: the superficial (or tangential) zone (SZ) closer to the surface where the thin collagen fibers are packed and aligned parallel to the articular surface for a better sheer force dissipation; the transitional (intermediate) zone (TZ) where the fibers are loosely packed and are in a mostly random order of orientation; and lastly the radial (deep) zone (RZ) where gradually thickening collagen fibers are more densely packed and oriented perpendicular to the articular surface acting as anchors to the cartilage structure (Benninghoff, 1925; Huber et al., 2000).

2.1.1.3 Proteoglycans

Proteoglycans are a special class of aggregated glycoproteins (aggrecans) with numerous attached, unbranched, and highly charged glycosaminoglycan chains (Hardingham, 1999). Glycosaminoglycans (GAGs) are macromolecular polysaccharides with a linear-chain structure (Figure 2.1). Proteoglycans are a major contributor to the biomechanical properties of cartilage. In essences, the structures of the collagen matrix in cartilage gives the tissue its unique shape; the filling of the highly charged GAG molecules between the fibers gives the tissue its unique biomechanical properties and makes articular cartilage tissue not only strong in tension but also resistant to compression (McDevitt, 1973). High concentration of aggrecans pulls water into the tissue and keeps it there, which creates a large osmotic pressure. This occurs due to the highly negatively charged anionic groups on the aggrecans that attracts counter-ions such as sodium (Na^+). A concentration difference of ions within cartilage and outside of cartilage creates an imbalance between freely diffusible ions and anions causing the water

to be drawn into the tissue. The water thus swells the tissue, which puts the collagen network under tension and therefore creating an equilibrium (Maroudas & Venn, 1977). Hence, articular cartilage provides and sustains a rigid but yielding load-bearing property, dependent on the characteristics of the collagen network and the retention of aggrecans due to the high concentration of proteoglycans.

2.1.1.4 Chondrocytes

Cells in human articular cartilage account for about 2% of the total volume in adult human cartilage (Hunziker, Quinn, & Häuselmann, 2002). It is these small amounts of cells, named chondrocytes, that are responsible for the synthesis and overall maintenance of the tissue over a lifetime. The concentration of the cells decreases gradually from the surface of the tissue, where the cells are densely packed, to the deep region of the tissue, accounting for just a third of cells that are found in the surface region of the tissue (Mitrovic, Quintero, Stankovic, & Ryckewaert, 1983). The shape of the cells is highly dependent on the local alignment and packing of the collagen. In the superficial zone, the chondrocytes are thin and flattened due to the highly packed parallel collagen fibers. In the transitional zone, more round-shaped cells can be found as the fibers within this region are more randomly arranged. In the radial zone, the cells have a more ellipsoid shape due to the incrementally thicker collagen fibers that are anchored into the tidemark. It has been reported that changes to the ECM environment due to high stress factors (such as impact injury or tissue wear and tear) or chemical changes can lead to cell synthesis responses (Urban, 1994).

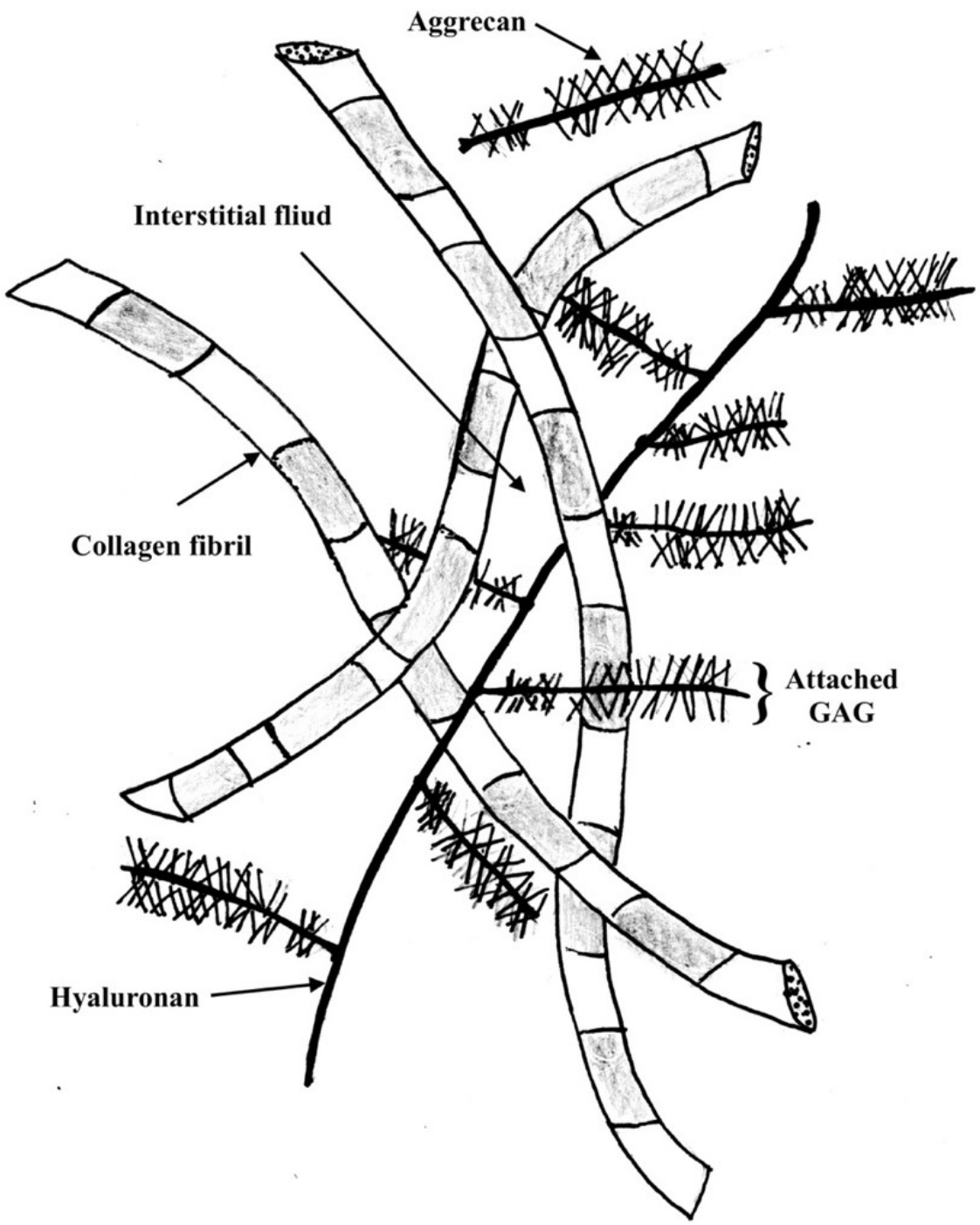

Figure 2.1 Extracellular matrix of articular cartilage has three major components, collagen (type II), proteoglycans (aggrecan), and water (not shown). Highly negatively charged proteoglycans and collagen fibrils interact to provide articular cartilage its compressive and tensile properties.

2.1.2 Histological Composition of Articular Cartilage

Articular cartilage at a histological level is very heterogenous and highly ordered (Figure 2.2). Since cartilage is firmly attached to the underlying subchondral bone, the tissue has a non-calcified region and a calcified region. This calcification-based division is indicated by the tidemark, which is a wavy and often irregular line that can often be observed in hematoxylin and eosin stained sections (Redler, Mow, Zimny, & Mansell, 1975). As we have mentioned before, the non-calcified cartilage is commonly sub-divided based on the orientation and the structure of the collagen matrix into three zones: the superficial zone (SZ), the transitional zone (TZ), and the radial zone (RZ). Since RZ is the thickest among the three zones, RZ in this dissertation is further subdivided into two sub-zones as the collagen properties vary across the zone (Buckwalter & Mow, 1992; Lee & Xia, 2013). A thin layer of mineralized tissue lies below the tidemark, which is called as the zone of calcified cartilage (ZCC) and serves as the structural interface or buffer to the subchondral bone plate (Brighton, Kitajima, & Hunt, 1984; Hunziker et al., 2002). In traumatic events, such as sport or battlefield injuries, damage to ZCC can initiate the cartilage degradation (Li et al., 2013; Radin & Rose, 1986). The zone of calcified cartilage has been studied insufficiently for its roles in cartilage disease progression, mainly due to its very thin thickness (Aizah, Chong, & Kamarul, 2019; Brandt, Radin, Dieppe, & Van de Putte, 2006; Deng et al., 2016; Findlay & Kuliwaba, 2016).

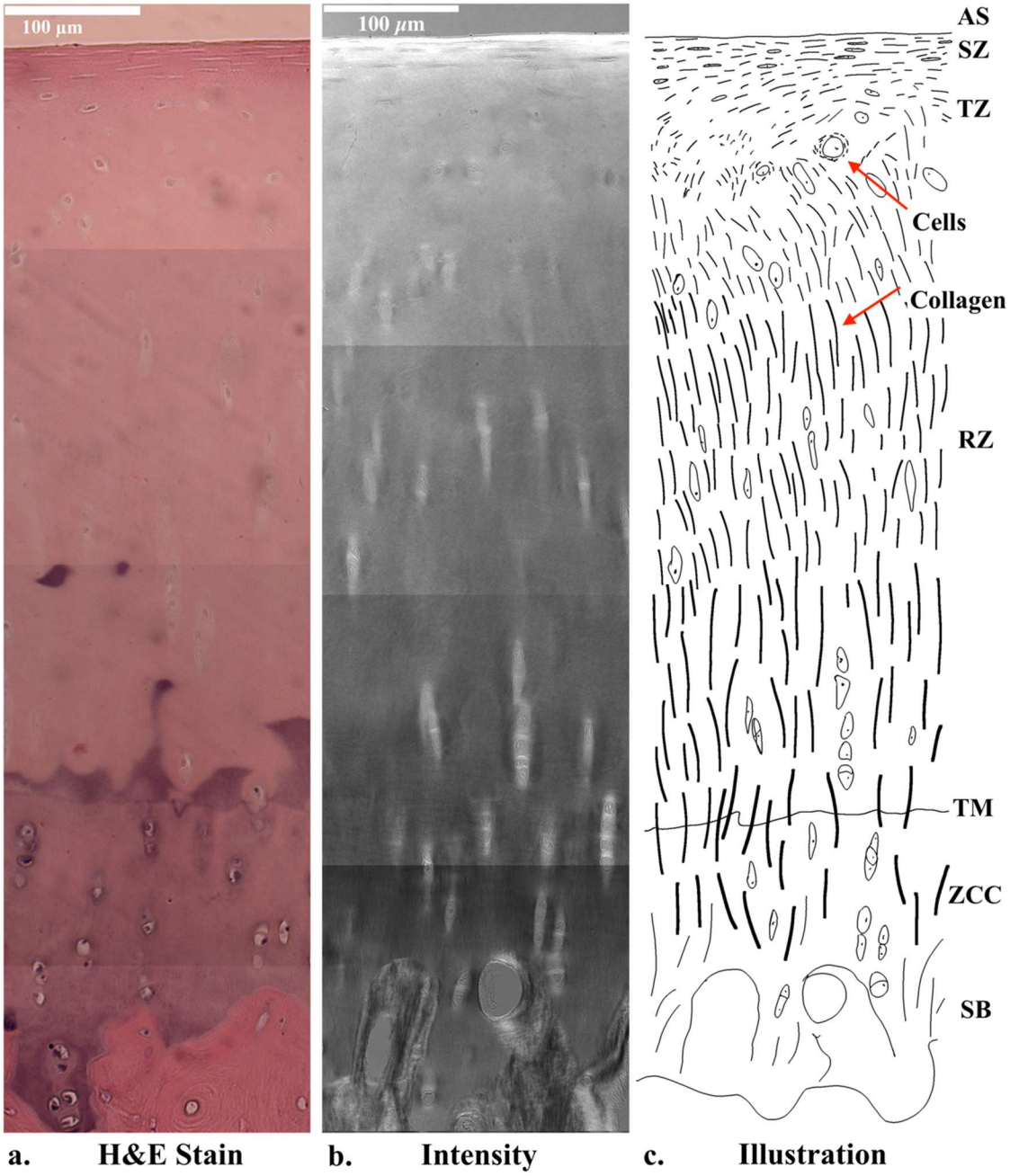

Figure 2.2 a) Hematoxylin and eosin section of AC, b) light intensity image of AC and c) schematic representation of articular cartilage showing the relative thickness and orientation of the collagen fibers (short lines) in different histological zones (SZ, TZ, RZ and ZCC) and the size and orientation of the chondrocytes (traced cell shapes). (The collagen fibers and chondrocytes are not drawn to scale.)

2.1.3 Topographical Properties of Tibiofemoral and Humeral Joints

The knee (tibiofemoral) joint is probably the most studied joint in OA research because of the high incidence of OA associated with the joint (and its easy access). The knee joint is a complex mechanical organ, the smooth movement of which is supported and controlled by multiple structural components (femur, tibia, patella, ligaments, and tendons). Different surfaces of cartilage within any single knee joint can have different modes of contact and motion (e.g., rolling, sliding, twisting) during physiological activities such as walking, which are likely tailored to different reactions to an applied load (Bullough, Yawitz, Tafra, & Boskey, 1985). Figure 2.3 shows the top view of a canine tibia, where the topographical surface variation is clearly visible over the entire tibial plateau. The cross-sectional slices from anterior to posterior directions reveal clearly the significant topographical (i.e., site to site) variations of both lateral and medial tibial plateaus, which likely provides effective load dissipation (Koo & Andriacchi, 2007).

There are large variations in the cartilage thickness from lateral to central direction on the lateral plateau and central to medial on the medial plateau. In canine tibia, cartilage around the central region (not covered by the meniscus) is thicker than in the periphery region (covered by the meniscus). Cartilage thickness also varies from the anterior to posterior direction. Topographical variations have been found in many properties of tibial and condyle cartilage, including thickness, shear modulus, birefringence, water content, GAG content and collagen content (Alhadlaq et al., 2004; Appleyard et al., 2003; Anders Bjelle, 1975; Bjelle, 1976; Lee et al., 2014; Lee et al., 2015; Terukina et al., 2003; Weiss et al., 1968; Zimny & Redler, 1974). Multidisciplinary

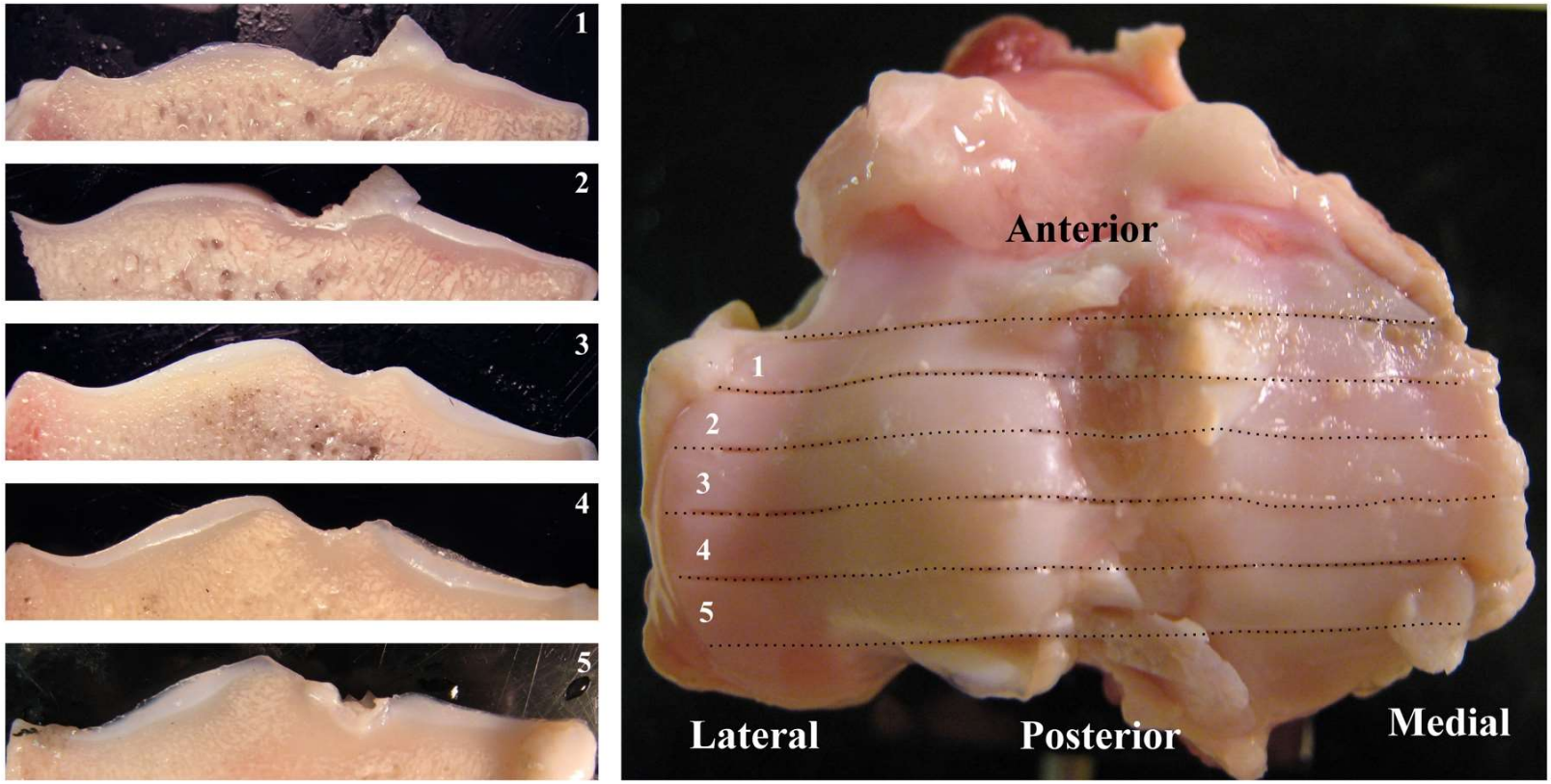

Figure 2.3 Topographical nature of articular cartilage in canine tibia. Tibial plateau surface without the menisci and the respective slices (1-5) cut from the tibia. The slices show the variations in the cartilage thickness and topographical variations from medial to lateral are significant. Cartilage is the opaque (milky color) tissue above the bone.

correlations among the tibial parameters have been well documented (Lee et al., 2014; Lee et al., 2015; Lee, Badar, Matyas, Qu, & Xia, 2016). Chapter 5 in this dissertation is a study of the importance of the topography of canine tibial joint as a function of MRI resolution based on disease progression (Badar et al., 2021). As OA progresses, the differences between healthy and OA tissues could become increasingly site-specific and load dependent. Even with the progress of age, there are site-specific changes in water and collagen content in asymptomatic cartilage (Brama, TeKoppele, Bank, Van Weeren, & Barneveld, 1999).

Cartilage from the shoulder joint (a ball and socket joint between the scapula and the humeral head) has also been well-documented in many animal cartilage studies, which is probably due to its availability as an easily accessible spare tissue. Compared to the knee cartilage, humeral cartilage has a much simpler contour as shown in Figure 2.4, which has been used as a classical three-layer model of AC in several studies (Xia, Moody, Burton-Wurster, & Lust, 2001). However, topographical variations are also known in humeral cartilage, including morphological, biochemical and biomechanical properties (Armstrong, Read, & Price, 1995; Bullough et al., 1985; Farquhar, Bertram, Todhunter, Burton-Wurster, & Lust, 1997; Fragonas et al., 1998; Kiviranta, Tammi, Jurvelin, & Helminen, 1987; Korvick & Athanasiou, 1997; Meachim, 1971; Rogers, Murphy, Cannon, & Briggs, 2006; Xia, Moody, Alhadlaq, Burton-Wurster, & Lust, 2002). These variations are also age- and sex-dependent (Kincaid & Van Sickle, 1981; Meachim, 1971; Xia, 2003), which show the complexity of the issue.

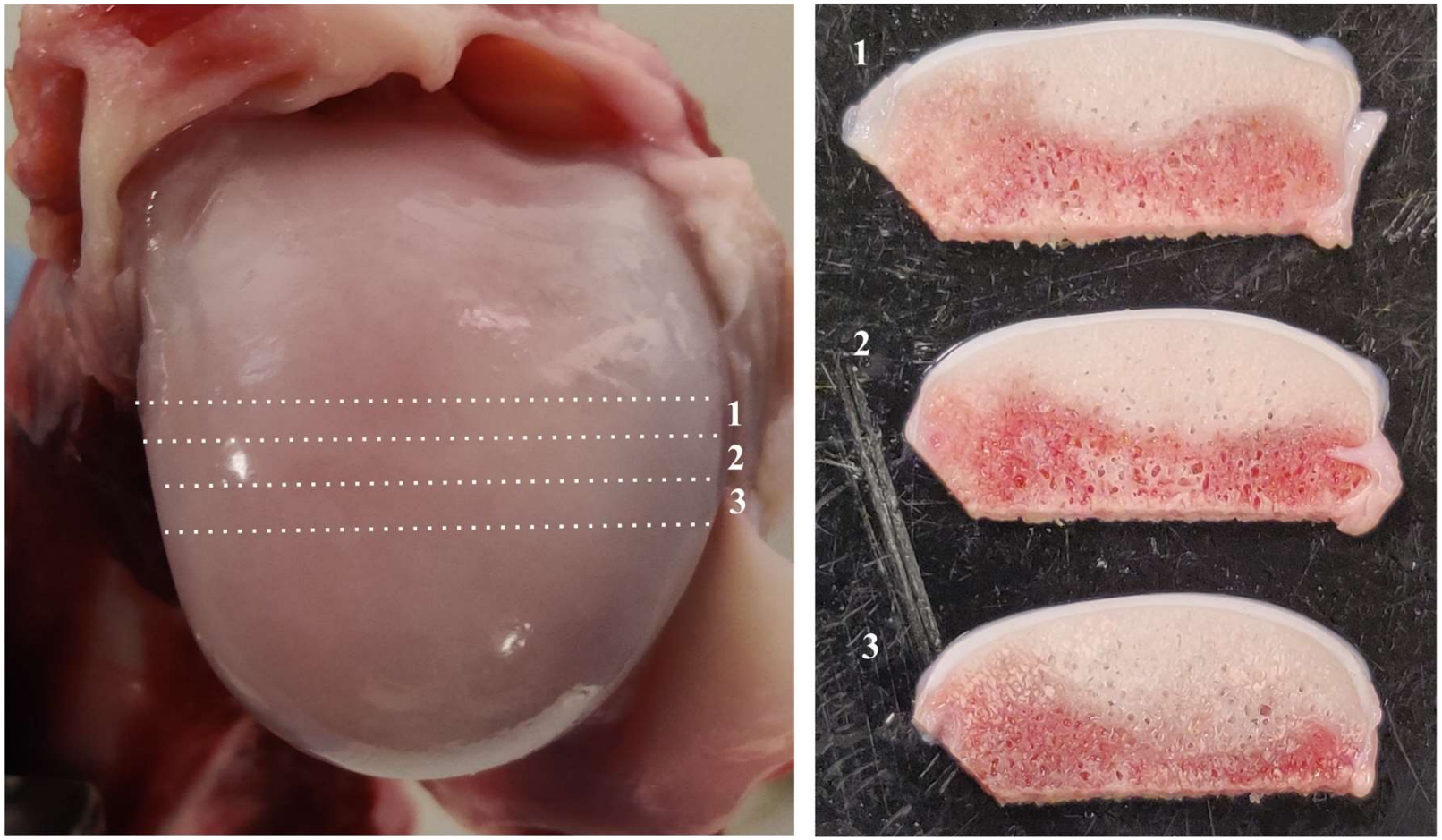

Figure 2.4 Topographical nature of articular cartilage in canine humeral head. Three slices from the central location of the humeral head are shown (1-3). The respective slices (1-3) of the humeral joint cut show little variations in the cartilage thickness and topographical variations are insignificant.

2.2 Osteoarthritis

The degradation of cartilage is the hallmark of osteoarthritis, which is the most common musculoskeletal disease that affects millions of people in our society (Buckland-Wright, Macfarlane, Lynch, Jasani, & Bradshaw, 1995; Huang & Schweitzer, 2014; Matyas, Ehlers, Huang, & Adams, 1999; Vignon et al., 2003; Watson, Carpenter, Hall, & Tyler, 1996). OA is a progressively degenerative disorder of the diarthrodial joints with damage occurring from the articular cartilage to the subchondral bone. OA can be classified into a long-term or a short-term disease, where the long-term is defined by the "wear and tear" of articular cartilage due to the repetitive use of the joints over many decades mostly occurring in seniors, whereas the short-term should have an identifiable cause due to localized trauma (e.g., sport injuries, battlefield injuries) or weight or genetic disorders. While long-term OA in most cases is the result of one or multiple short-term events that have been neglected for long periods of time. OA is characterized in pathology by an imbalance in the ECM leading to proteoglycan loss, osteophyte formation, synovitis, and subchondral bone changes. A gradually progressive OA allows for different pathological degradations of cartilage at different time points, at lesion sites on a joint surface, and in different histological zones, which makes an accurate diagnostic standard difficult to establish (McDevitt, Gilbertson, & Muir, 1977).

2.2.1 Diagnostic Classification

Clinically, the disease is characterized by a number of individual disorders such joint pain, stiffness, limitation of movement and local inflammation. These disorders have little systemic effect (Flores & Hochberg, 1998). Structurally OA can affect not only the articular cartilage but also the subchondral bone, ligaments, and synovial

membranes (Wenham & Conaghan, 2013). A clear and precise diagnosis of early OA is important for two reasons. Firstly, it allows for an early identification of disease before advanced degeneration occurs. And secondly, it also identifies patients with high risk of progression (Kon, Filardo, & Marcacci, 2011). The study of OA for its natural progression and diagnostic interventions in humans is a complicated, mainly because OA is mostly commonly presented to physicians in its late stages and any measure of early OA is highly unachievable. Hence, animal models have been used over many decades where a detailed evaluation of early to late stages of disease progression for diagnostic and/or therapeutic strategies is possible. These animal model studies provide a bridge between animal findings and the process of OA in humans (Seibel, Robins, & Bilezikian, 1999).

2.2.2 Animal Models of Osteoarthritis

Canine models are advantageous in OA studies over other animal models, mainly due to the vast amount of data available from previous cartilage studies. A well-defined and studied model in canines is the Pond-Nuki model (Pond & Nuki, 1973), where the anterior cruciate ligament (ACL) is transected in the stifle joint. Signs of early lesions include cartilage softening, fibrillation and erosion, which has been reported predominately in the medial tibial plateau. With similarities to human OA, the Pond-Nuki model is a practical and useful model to validate the study of OA progression and the diagnostic markers associated with OA (Seibel et al., 1999). This model has been used for the study of disease progression in this dissertation where the development of sensitive measures by a noninvasive MRI quantification of the topographical and

morphological changes in early OA would be valuable for monitoring disease progression and for evaluating the treatment efficacy.

2.2.3 Medical Imaging of Osteoarthritis

Although OA and other joint diseases have been studied extensively, there are no effective interventions that can hinder or even reduce the degradation progression. Both clinicians and researchers in the field of osteoarthritis recognize the ever-increasing importance of non-destructive and non-invasive imaging in OA for early diagnosis, prognosis, and follow-up care and treatment. One key reason that has prevented any successful diagnostic and interventional procedures is our inability to accurately detect the early diseases.

The most commonly used and cheaply available imaging metric for diagnosing and measuring clinical efficacy in OA is the joint space narrowing, which can be measured by radiographic procedures (Mazzuca et al., 2003). It can at best detect late stages of OA (Buckland-Wright, Macfarlane, Williams, et al., 1995; Hunter et al., 2015; Ley et al., 2016; Vignon et al., 2003). Other related measurements in radiography include abnormalities, such as cysts, osteophytes, and subchondral sclerosis (Guermazi et al., 2013). These measurements are unreliable as it must factor in the lack of pre-imaging markers for the patient before the onset of the disease. Despite these limitations, radiography remains a go-to standard for an imaging-based diagnosis of OA and a final assessment in the clinic for the measurable changes of the synovial joints due OA.

2.3 Magnetic Resonance Imaging

This section briefly describes the basic concepts of Magnetic Resonance Imaging that are needed to understand its application in osteoarthritic cartilage.

2.3.1 Nuclear Magnetic Resonance

Magnetic Resonance Imaging is the imaging version of a physics phenomenon called Nuclear Magnetic Resonance (NMR). The magnetic properties of atomic nuclei can be described by the means of their nuclear spin angular momentum (***S***) and their magnetic moment (***μ***). In the classical description of NMR, ***S*** can be considered as a vector that has a unique value for each particular nuclear spin — either an integer or half-integer. ***S*** is an intrinsic property of the nucleus, and its value depends on composition of the element. The magnitude of spin angular momentums is given by

$$|\boldsymbol{S}| = (s(s+1))^{1/2}\,(h/2\pi) \tag{2.1}$$

where s is the spin quantum number and has a half integer or integer value. Isotopes of the same element may have different spin number (i.e., s = ½ for hydrogen (^{1}H) and s = 1 for deuterium (^{2}H)). The z component of ***S*** is quantized as

$$\boldsymbol{S}_z = m\,(h/2\pi) \tag{2.2}$$

where h is Planck's constant an m is the magnetic quantum number which has (2s + 1) values between s and -s.

For hydrogen nuclei (spin = 1/2) in thermal equilibrium in an external magnetic field B_0, there are two allowed energy levels, hence two possible directions for the spin angular momentum, $S_z = \pm 1/2\ (h/2\pi)$. Since the lower energy level is more populated, a macroscopic magnetization forms in any practical specimen due to the population difference between the spins at the two allowed levels.

The magnetic moment (***μ***) of a nucleus is associated with its angular momentum

$$\boldsymbol{\mu} = \gamma \boldsymbol{S} \tag{2.3}$$

where γ is known as the gyromagnetic ratio.

In the absence of an external magnetic field B_0, the energy levels are degenerate for all nuclear spins. In the presence of an external magnetic field, a single nucleus with spin-1/2 can have one of the two allowed energy levels. The transition between the two levels can be induced by absorption or emission of quanta with the energy of

$$E = - m(h/2\pi)\gamma B_0 \tag{2.4}$$

The selection rule in quantum mechanics states that Δm must be ± 1, so transitions are only possible between adjacent energy levels. Therefore, the difference in energy for spin-½ nucleus should be

$$\Delta E = (h/2\pi)\ \gamma B_0 \tag{2.5}$$

and the resonance frequency is defined by

$$\omega_0 = \gamma B_0 \tag{2.6}$$

which is called Larmor frequency in NMR and MRI.

A complete (or partially) saturated system will return to the thermal equilibrium state in two different relaxation processes. Firstly, absorbed energy will redistribute within the spin system in which there is a transition of a nucleus from a higher to a lower level accompanied by a transition from a lower to a higher state, a process called spin—spin (transverse) relaxation. Secondly, there will be a gradual loss of energy to the neighboring nuclei in the system, collectively called the lattice, resulting from transitions of nuclei from the upper state to the lower state. This second process is spin—lattice (longitudinal) relaxation. The time constants that characterize these two processes are T2 and T1, respectively. The time constants T1 and T2 yield valuable information about the local interactions experienced by nuclei.

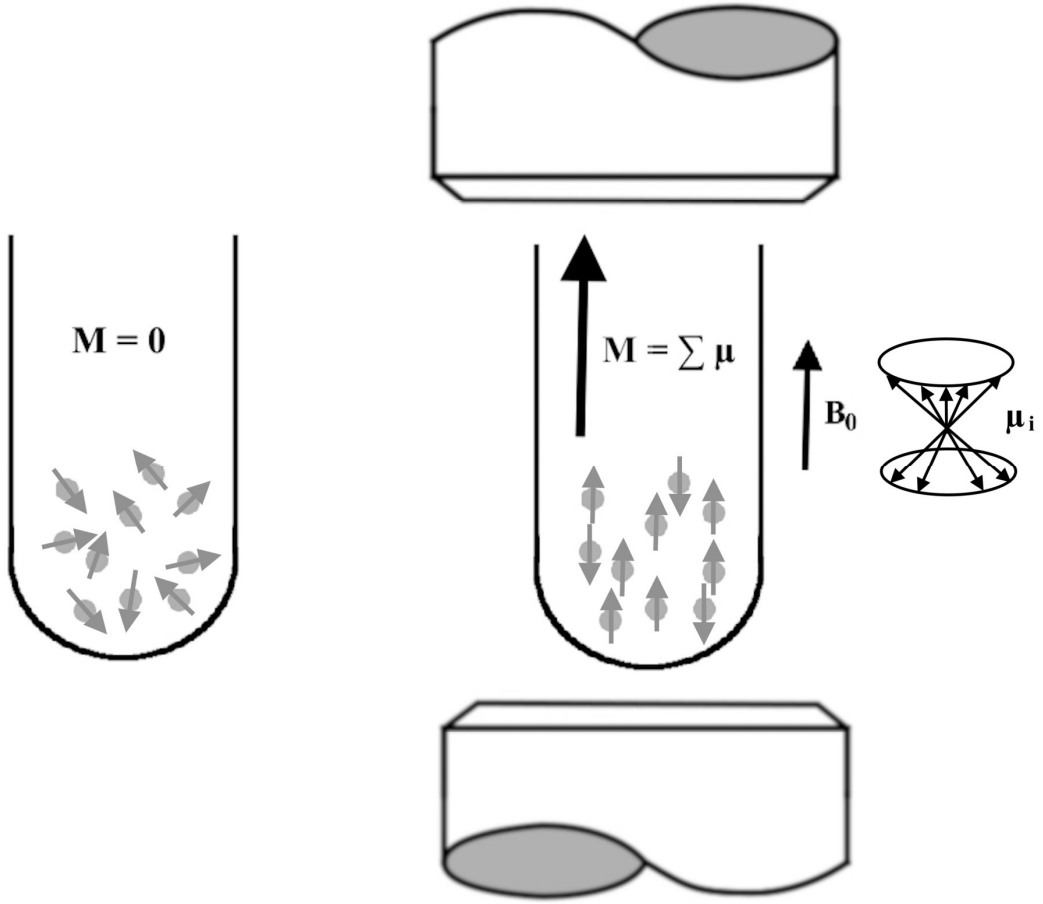

Figure 2.5 An illustration of the macroscopic magnetization of an ensemble in an external magnetic field (B_0). Without B_0 the spins are oriented randomly (left), and the net magnetic moment (M) is zero. The ensemble in B_0, the spins align with this field with a slight excess of spins aligning parallel to the field (right), leading to a non-zero net magnetic moment M_0. The magnitude of the net magnetic moment is approximately proportional to the magnitude of the external magnetic field.

2.3.2 Spin Relaxations

Any practical sample contains an enormous number of nuclei. The ensemble average of the nuclear spins in the sample is called the macroscopic magnetization **M**. Without an external magnetic field, all spins are randomly oriented, which results a net zero **M**. When the sample is placed in an external magnetic field $\mathbf{B}_0$ and under thermal equilibrium, each spin can be said to be in either spin up (+) or spin down (-) direction. Due to the large number of nuclear spins in any practical sample, the transverse component of **M** in the transverse plane is averaged to zero due to the even distribution of the phase angles of the nuclei. The longitudinal z component of **M** arises from the difference in the populations between the upper and lower energy states. Since there is an excess of spins that are aligned parallel to $\mathbf{B}_0$, a non-zero **M** occurs, which is parallel to with the direction of the external magnetic field $\mathbf{B}_0$. The magnitude of the equilibrium magnetic moment, $\mathbf{M}_0$, is proportional to the population difference between the spins in the two energy levels for spin-1/2 nuclei.

Newton's second law describes the time evolution of the macroscopic magnetization in an external magnetic field, by equating the torque to the rate of change of the angular momentum as:

$$\frac{d\boldsymbol{M}}{dt} = \boldsymbol{\gamma}(\boldsymbol{M} \times \boldsymbol{B}) \tag{2.7}$$

When $\mathbf{B}=B_0\mathbf{k}$, the above equation has a solution that corresponds to a processional motion about **k** at the rate ω_0 (Larmor frequency).

We can apply a second magnetic field $B_1(t)$ to the nuclear spins and introduce a frame of reference that rotates about B_0 at frequency ω that is close or at ω_0. In this

rotating frame, one component of $B_1(t)$ can become stationary, which interacts with the magnetization vector **M**.

Two distinct forms of relaxation occur to **M**, which now represents the individual nuclear spins in the specimen, after the application of a B_1 field (RF pulse) to the system. They are:

$$\frac{dM_z}{dt} = -\frac{M_z - M_0}{T_1} \tag{2.8}$$

and $$\frac{dM_\perp}{dt} = -\frac{M_\perp}{T_2} \tag{2.9}$$

where T1 and T2 have been defined earlier in this Chapter and $M_\perp$ is the transverse component of the magnetization **M**. The time that is required for the spin system to return to thermal equilibrium with its surroundings after the end of the excitation field $B_1(t)$ is defined by T1. The time that characterizes the decay of phase coherence between the individual spins in the transverse plane is defined by T2. Since T2 processes arise from both the fluctuations of local magnetic fields and the influence of static magnetic fields while T1 processes arise only due to the fluctuating magnetic field at the resonance frequency, $T1 \geq T2$ for any spin system.

The change in the magnetization following an excitation is independently caused by external magnetic fields and the relaxation processes, and can be described mathematically by the Bloch equation:

$$\frac{d\mathbf{M}}{dt} = \gamma(\mathbf{M} \times \mathbf{B}) - \left[\frac{M_x i + M_y j}{T_2} + \frac{(M_z - M_0)k}{T_1}\right] \tag{2.10}$$

In this equation, **B** is the sum of both the static and RF field components, and **M** is the net magnetization vector. Consider the situation (Figure 2.3) where a 90˚ pulse is applied by

the $\mathbf{B_1}$ field which causes the net magnetization to be rotated by 90˚ into the transverse plane. After the $\mathbf{B_1}$ pulse is turned off, the two relaxation processes can be characterized by the solutions to the Bloch equations as:

Transverse Relaxation: $$\mathbf{M}_{\perp}(\mathbf{t}) = \mathbf{M}_{\perp}(\mathbf{0})\boldsymbol{e}^{-\boldsymbol{t}/\boldsymbol{T_2}} \quad (2.11)$$

and

Longitudinal Relaxation: $$\mathbf{M}_{\boldsymbol{z}}(\mathbf{t}) = \mathbf{M}(\mathbf{0})(\mathbf{1} - \boldsymbol{e}^{-\boldsymbol{t}/\boldsymbol{T_1}}) \quad (2.12)$$

These equations can be incorporated into the MRI experiments, which generate either T1-weighted and T2-weighted images of the sample. These relaxation-weighted images are common in MRI and provide a measure of tissue characteristics via the signal intensity of MRI. Careful use of imaging parameters results in different tissue contrasts and is often helpful for gathering complementary information for diagnostic purposes.

Signal-to-noise ratio (SNR) is theoretically proportional to several fundamental quantities in the experiments, primarily the characteristics of the nuclear spins and the strength of B_0. Since protons have the highest gyromagnetic ratio (i.e., $\gamma^{H} > \gamma^{Na}$), the strongest signal intensity can be found in proton MRI (i.e., MRI of water-containing specimens). Other inherent cautions in practical experiments deal with the image artifacts, which include motion artifacts, inhomogeneities of either the B_0 or B_1 fields, and susceptibility artifacts caused by inhomogeneity of the specimen structures. The presence of metal in human body (i.e., an artificial joint or wires of heart pacemakers) can also distort the uniformity of the main magnetic field, hence producing image artifacts.

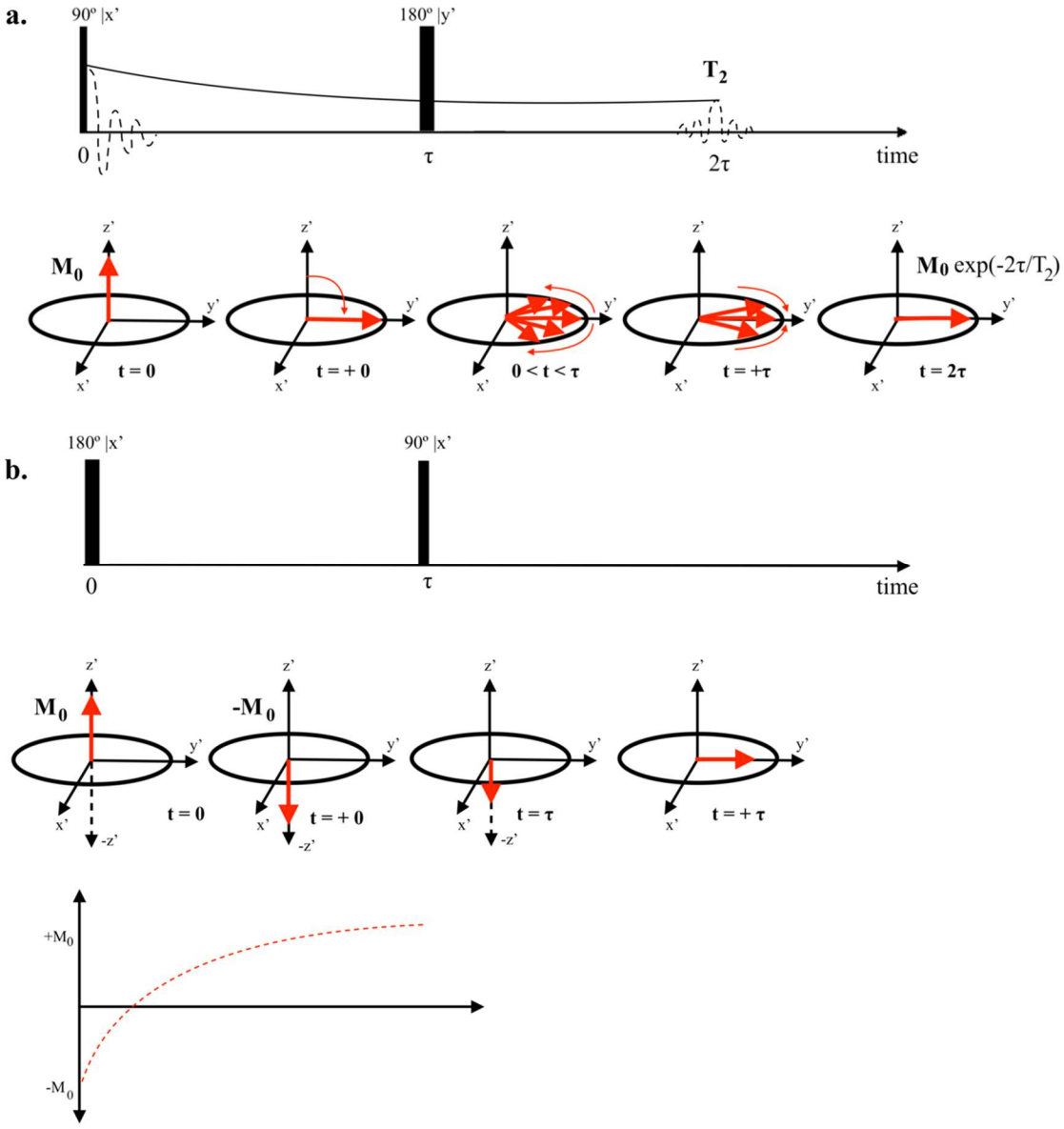

Figure 2.6 A classical view of a Spin echo (a) and Inversion Recovery (b) pulse sequence showing the evolution of the magnetization (**M**). T2 (spin-spin; transverse) and T1 (spin-lattice; longitudinal) are measured using the two sequences.

2.3.3 MRI of Articular Cartilage

Being non-invasive and sensitive to the molecular motions, MRI has undisputable potential to become the leading diagnostic tool for cartilage health (Choi & Gold, 2011; Conaghan, 2006; Huang & Schweitzer, 2014; Matzat et al., 2013; Mosher et al., 2013; Nemec et al., 2011; Pakin et al., 2006; Wang et al., 2016; Wang et al., 2015). In modern clinics, MRI is the best noninvasive imaging technique currently available for the assessment of articular cartilage because of its excellent soft-tissue contrast (Disler, Recht, & McCauley, 2000; Gold et al., 2006; Gold, Chen, Koo, Hargreaves, & Bangerter, 2009). MRI can detect a number of degradation biomarkers in joint tissues, including cartilage morphometry, fissuring, partial- or full-thickness cartilage defects, bone marrow lesions, bone shape/attrition, and subchondral bone area (Conaghan et al., 2006; Hunter et al., 2011). Although these MRI biomarkers measure tissue morphology, they have been used to monitor the progression of cartilage damage and the effectiveness of treatment. In addition, several quantitative MRI parameters can potentially measure biochemical and physiological information about articular cartilage (Burstein & Gray, 2006; Eckstein, Burstein, & Link, 2006).

2.3.4 Quantitative MRI Measures of Cartilage

Quantitative MRI parameters such as T2 relaxation time have been used extensively for the diagnostic assessment of OA cartilage (Alhadlaq & Xia, 2004; Kurkijarvi, Nissi, Kiviranta, Jurvelin, & Nieminen, 2004; Lee et al., 2015). T2 relaxation in cartilage can reflect the mobility of water molecules in their local environments, which show anisotropic properties in cartilage and other collagen-rich tissues (Xia, 1998; Xia, Zheng, Szarko, & Lee, 2012). For the simplest notion in relation to osteoarthritis

cartilage, a high T2 value implies a tissue having less proteoglycans, less organized collagen matrix, more extracellular water, and looser interactions between water and macromolecules (Hannila, Raina, Tervonen, Ojala, & Nieminen, 2009; Hanninen, Rautiainen, Rieppo, Saarakkala, & Nissi, 2017; Li et al., 2007; Millington et al., 2007; Stahl et al., 2007).

Since the dynamic motion of water molecules can be influenced by the structural properties of the collagen matrix in articular cartilage (Xia, Moody, & Alhadlaq, 2002), T2 in cartilage has strong depth and orientational dependencies (the magic angle effect), when standard spin-echo (SE) or gradient-echo (GE) based MRI sequences are used. This sequence-dependence in MRI makes the accurate measurement of tissue thickness difficult (Shao et al., 2017; Wang & Xia, 2012). In addition, the echo time in SE and GE based imaging sequences is a finite number in range of several 10s of milliseconds, which can lead to weak signals in the deep portion of articular cartilage, due to the densely packed collagen matrix. This low MRI signal can make the visualization and quantification of T2 in the deep RZ and ZCC impossible (Wang, Badar, & Xia, 2018). In order to visualize ZCC, special imaging sequences such as ultra-short echo time (UTE) imaging sequences can be used in MRI, which have a much shorter echo time (as short as a fraction of a millisecond) (Bae et al., 2010; Du et al., 2013; Nykänen et al., 2020; Shao et al., 2016).

In clinical MRI, study of the ZCC is mainly limited to qualitative comparisons between long and short echo-time images due to the resolution limitation and orientational limitation (Bae, Biswas, Chen, Chang, & Chung, 2014). In μMRI, both SE and UTE sequences have been used to study the deep cartilage and ZCC but without

complementary correlation at optical resolution (Mahar, Batool, Badar, & Xia, 2018). The use of UTE sequences helps in determining the very short T2 characteristic of biological tissue (Du et al., 2013; Fabich, Sederman, & Holland, 2016). In the cartilage-bone specimens, the deep portion of the non-calcified cartilage, ZCC and subchondral bone plate (SBP) have intermediate to short T2 due to the amount of the minerals and strong dipolar interaction (Shao et al., 2016). When the cartilage-bone specimens are oriented at 54.7º (magic angle) to the magnetic field, the tissue appears thicker and brighter in the GE/SE-based imaging sequences, which allows the accurate measurement of tissue thickness (Wang et al., 2018). To visualize and quantify the deep RZ and ZCC, one needs the UTE sequences, which could have TE as short as tens to hundreds of μs.

2.4 Polarized Light Microscopy

2.4.1 Polarized Light

Maxwell's theory defines light as an electromagnetic wave that oscillates in two component fields, an electric field and a magnetic field that are perpendicular to each other on the x-axis and y-axis respectively while propagation is along the z-axis. A beam of light in which all the vibrations are in one direction can be called linearly polarized light. Linearly polarized light propagates only along a single directional plane. Devices that transmit a beam of light in a single plane are called linear polarizers. The orientation of the plane of polarization can be adjusted by rotating the linear polarizer about its beam axis (Kliger, Lewis, & Randall, 1990a, 1990b). Measurement of birefringence in a specimen can be carried out when the plane of propagation of the analyzer (a linear polarizer placed after the specimen) is crossed to the plane of propagation of the polarizer (a linear polarizer placed before the specimen). For materials that have anisotropic

properties, intrinsic birefringence is observed when the plane of propagation of the polarizer and the reference axis of the materials are at 45˚ apart (Módis, 1991).

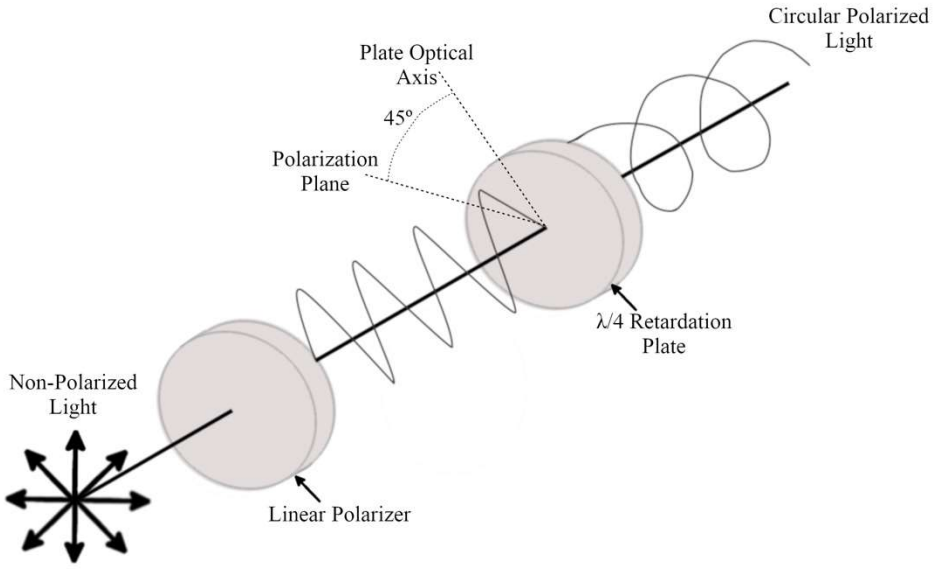

Figure 2.7 Illustration of the process of circularly polarized light produced from non-polarized light. By allowing light to pass through a combination of a linear polarizer followed by a quarter wavelength plate, circularly polarized light is produced.

Circularly polarized light is a particular case of polarized light when the x and y vectors of the electric components are 90˚ out of phase, therefore the tip of the resultant vector maps out a circle as it propagates along the z direction (Kliger et al., 1990b). The advantage of circularly polarized light over linearly polarized light is that circularly polarized light can observe birefringence of a specimen in any direction (Módis, 1991).

Therefore, it is a useful tool in the observation and measurements of materials or biological tissues that are intrinsic with isotropic or anisotropic properties.

Circularly polarized light is produced in practice with a combination of a linear polarizer and a quarter-wave plate. A quarter wave plate causes the phase of passing polarized light to be retarded by a quarter of a wavelength (90º). At an orientation of 45º, the plate forms circular polarized light (Figure 2.7). Hence, quarter wave plates are a useful tool to examine the optical path differences in materials with intrinsic birefringence. Polarized light microscopes are highly equipped and designed to provide high resolution 2D images of biological specimens. Most polarizing microscopes can be outfitted with a digital camera that is connected to a computer to capture and analyze high-resolution images from birefringent materials or biological samples.

2.4.2 Polarized Light Microscopy of Articular Cartilage

Polarized light microscopy is a gold standard measure of anisotropic properties in any biological as well as non-biological material (Oldenbourg & Mei, 1995). Due to its anisotropic nature associated by the depth-dependent collagen fiber orientations, articular cartilage requires a sensitive and high-resolution imaging technique to describe the morphological aspects of the overall histological variation from a healthy to an osteoarthritic cartilage. Polarized light microscopy can enhance the image contrast and aid in an indirect measure of the morphological characteristics of collagen fibers in cartilage (Xia et al., 2003). With the computation of birefringent images from PLM, quantitative high-resolution measurements can provide further insights into tissue structures measured by non-invasive μMRI (Xia, Moody, Alhadlaq, et al., 2002). The structural data from MRI T2 anisotropy generally requires validation through correlation

with data from an independent (and better resolution) method. For articular cartilage, PLM offers such a method for the quantitative validation and correlation of the MRI data.

Quantitative PLM can calculate two 2D images from the same tissue section, one image describes the collagen fiber orientations, and the second image describes the optical retardation. Figure 2.8 shows a pair of the retardation and azimuth (angle) maps from a histological section (6 μm in thickness), which were obtained from a normal canine cartilage-bone specimen. 1D profiles are also extracted. The azimuth or angle image/profiles is a representation of a voxel-averaged collagen fiber orientation, where the fibers in the superficial zone and radial zone are perpendicular to each other, which is a quantitative confirmation of the well-known feature of a healthy cartilage in which collagen fibers have a 90º orientational difference between the surface and deep tissues. The azimuth map has been used for the quantitative division of cartilage tissue into the histological sub-tissue zones (Lee & Xia, 2013; Xia et al., 2001). The second image/profile, the retardation, represents the voxel-averaged collagen fiber organization and packing density, which retards the polarized light from a quantitatively measured wavelength (nm).

For an osteoarthritic cartilage, the azimuth image/profile would show an overall change in the fiber orientation while the retardation changes would provide a detailed understanding of the changes to the fiber organization and packing density and the overall impact to the biomechanical structure of articular cartilage (Alhadlaq et al., 2004). A subtle feature about the azimuth map in cartilage is the randomization of the transitional zone, which from an overall point of view is not quite random but has an intrinsic orientation embedded within the whole cartilage. On the depth-dependent

profile, the 0º to 90º azimuth transition aligns well with the minimum retardation, which represents the transitional zone where the fibers are locally isotopic and randomly oriented.

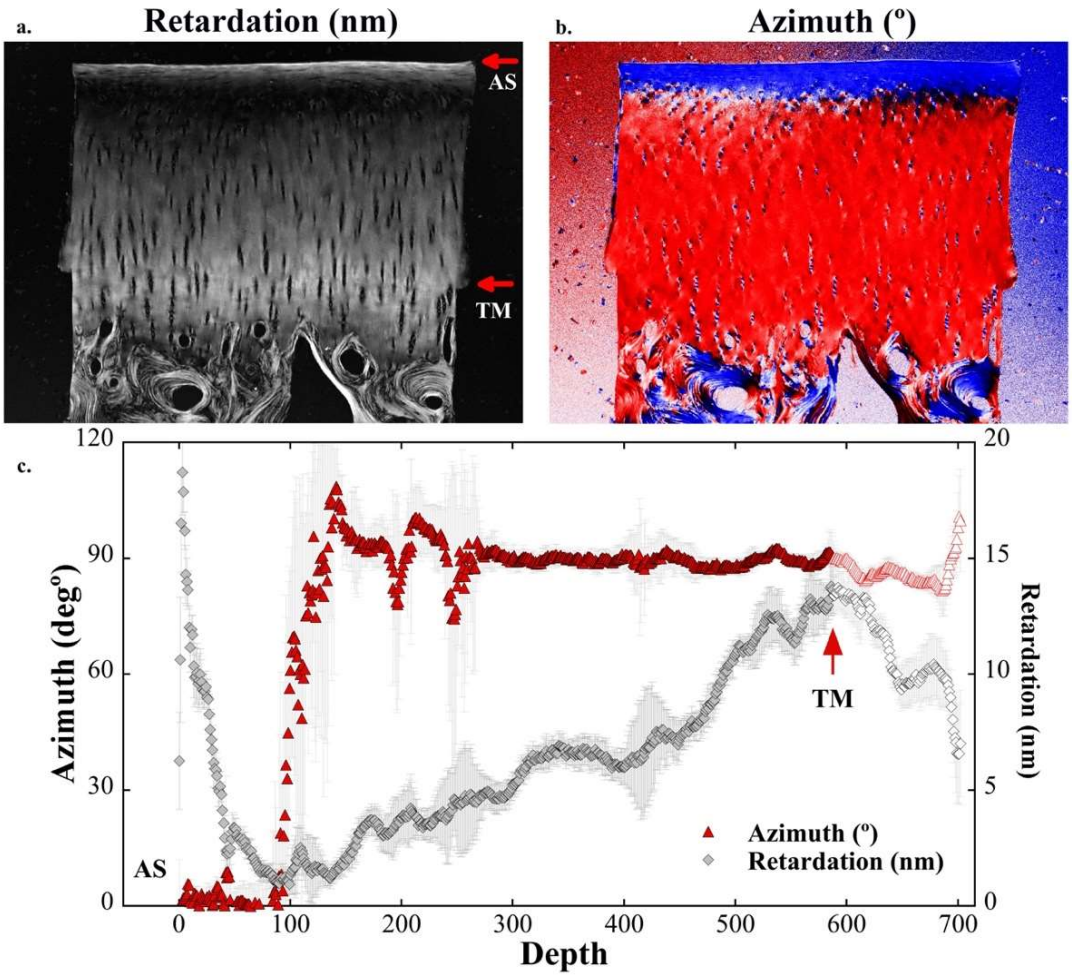

Figure 2.8 PLM images from a 6 µm thick articular cartilage histological section; a) retardation map, b) azimuth map, and c) 1D retardation and azimuth profiles represent the depth-dependent average from the ROI selected from the center of each map. Retardation map is represented as a grayscale image scaled from 0 to 20 nm, while the azimuth map is blue, white/black, and red colors representing the average collagen fiber orientation. Blue represents 0º while red represents 90º fiber orientation.

CHAPTER THREE

MATERIALS AND METHODS

This chapter describes the overview of materials and methods used in this study of the healthy and osteoarthritic canine articular cartilage. Section 3.1 investigates the improvement in the detection of osteoarthritis in cartilage by the interpolation of T2 images, in the situation when the native MRI resolution is insufficient to resolve the depth-dependent T2 characteristics in articular cartilage (Badar & Xia, 2017), which will be discussed further in Chapter 4. Section 3.2 describes the topographical and zonal T2 patterns of multi-resolution MRI in medial tibial cartilage in a canine model of osteoarthritis, initiated by the ACL transection surgery, and studied after 8-weeks and 12-weeks post-surgery (Badar et al., 2021), which will be discussed further in Chapter 5. Finally, section 3.3 describes the dual-modality microscopic imaging study quantifying the interface region between the non-calcified cartilage and the SBP, which includes the deep portion of the non-calcified articular cartilage and the zone of calcified cartilage (ZCC) with the aid of μMRI and PLM (Badar & Xia, 2021), which will be discussed further in Chapter 6.

3.1 Image Interpolation Improves the Zonal Analysis of Cartilage in MRI

3.1.1 Sample Preparation

Twelve mature canines, where six were non-operated controls and the other six each had the anterior cruciate ligament transected on one of the knees 12 weeks prior to sacrifice. One knee from each of the six non-operated canines was labeled as control (N) (three left knees and three right knees). Six operated knees from six animals were labeled

as OA and six non-operated adjacent knees were labeled as contralateral (C). These canine joints belonged to a multidisciplinary study of the OA progression in our lab, which was approved by the institutional animal care and use committee (IACUC). Recently, a blind study of the gross anatomic disease progression in these canine joints has been completed (Kahn et al., 2016). Using the OARSI scores of 0-4 that graded different parts of a joint (Cook et al., 2010), the 12-week contralateral tibias had a score of 1, while the 12-week transected tibias (OA) had a score of 2; the difference was statistically significant. After excess tissues (muscles and skin) were trimmed, all unopened knee capsules were placed in a sample holder and imaged (within 24 hours of sacrifice) in a Varian MRI system with a 7T/20 cm horizontal magnet (Henry Ford Hospital, Detroit, MI) – the system is termed as macro-MRI in this report. After the imaging of the intact joints, each joint capsule was opened to harvest rectangular cartilage-bone blocks from the medial tibial plateau, with each block representing a different topographical location on the joint surface. Each specimen had an intact interface between cartilage and bone, with an approximate size of 3x3x4~5 mm^3. The blocks were immersed in physiological saline solution, which also contained 1mM of Gd-$DTPA^{2-}$ contrast agent (pertaining to a T1 study (Lee et al., 2014)) and 1% protease inhibitor cocktail (Sigma, MO). The specimens were maintained at 4ºC (never frozen) and later imaged using μMRI.

3.1.2 MRI Protocols

Quantitative T2 imaging in macro-MRI used a commercial multi-slice multi-echo (MSME) pulse sequence on a 7T/20cm horizontal magnet. The field of view (FOV) was set at 5 cm with a matrix size of 256 x 256, which yielded an approx. 200 μm pixel size.

The repetition time was 3 sec with a total scan time of 51.2 minutes; and the ten echo times had an increment of 10 ms with the minimum echo time at 10ms. Ten image slices, each having a thickness of 1 mm, were acquired, approx. 2.5 mm apart from each other. Microscopic MRI (μMRI) experiments run at Oakland University (MI) on the specimens harvested from the same locations of the macro-MRI have been reported and were used as a reference (Lee et al., 2014; Lee et al., 2015; Lee et al., 2016). Briefly, quantitative T2 imaging used a magnetization-prepared imaging sequence on a Bruker AVANCE II system with a 7T/9 cm vertical magnet (Bruker Instrument, Billerica, MA). The FOV was set as 0.45 cm and a slice thickness of 0.8 mm, resulting in a 2D pixel size of 17.6 μm. Other experimental details can be found in the papers cited above. T2 images for both macro-MRI and μMRI were calculated using a single exponential model using MATLAB (MathWorks, Natick, MA) with a good correlation factor between data and model within the tissue region. Further explanation of the single exponential model using MATLAB (and other software) is presented in Appendix B of the dissertation.

3.1.3 Interpolation of Macro-MRI Images

The native image in macro-MRI (256x256 matrix, with a nominal pixel size of 200 μm) was reconstructed to 512x512 (nominal pixel size of 100 μm) using two different methods. The first method (termed "FID 512") was carried out on the Varian NMR spectrometer, utilizing the original time-domain Free Induction Decay (FID) data and the Fourier Transform reconstruction option (zero-filling). The second method (termed "ImageJ 512") was carried out utilizing the image-domain 2D T2 images (256x256) and the bicubic interpolation procedure in a public domain software ImageJ® (version 1.4.3, NIH, MD, USA).

3.1.4 Division of Sub-Tissue Zones in Cartilage

The T2 profiles at both 200 μm/pixel and 100 μm/pixel were extracted from the 2D T2 images from five topographical locations on the medial tibia for each of the six healthy (N), contralateral and OA knees and included the averaging of two adjacent columns to improve the signal to noise ratio (SNR). A count of sixty data points for each disease state resulted from six joints from five locations with two data pixels (ROI) per division. Since the column averaging was perpendicular to the direction of the cartilage depth, the depth resolution was still 200 μm or 100 μm. These T2 profiles were further analyzed using KaleidaGraph® (version 4.5.2, Synergy, PA, USA) by three methods of sub-tissue division. The first two methods divide the cartilage depth (thickness) into two equal-thickness divisions (Upper 1/2 and Lower 1/2), and three equal-thickness divisions (Upper 1/3, Middle 1/3, and Lower 1/3), respectively. These equal-thickness division methods are similar to the common practice implemented in clinical MRI diagnosis of cartilage OA, since accurate morphological division of human cartilage is not easily available in clinical MRI due to the low pixel resolution. Our method divided the cartilage depth into three unequal-thickness zones (SZ, TZ, RZ), based on the average zonal thickness data from the known imaging and morphological findings at 17.6 μm resolution (Lee et al., 2015; Lee et al., 2016; Lee & Xia, 2013), with the first two pixels each representing the SZ and TZ respectively and the remaining pixels being assigned (as average) to the RZ. To resolve the issue of varying thicknesses across the selected tibial ROI, the T2 profiles were scaled at relative thickness with the articular surface (AS) as 0 and the bone-tissue interface as 1.

3.1.4 Statistical Analysis

A one-way ANOVA with Tukey-Kramer HSD with α level of .017 (using JMP®) was performed on all specimens of the medial tibia, to pairwise compare T2 differences among healthy (N), contralateral (C) and OA samples at two different resolutions, with the three distinct types of division methods. For a highly effective result, a resultant p-value of less than 0.01 was considered significant.

3.2 Topographical and Zonal Patterns of T2 Relaxation in Osteoarthritic Tibial Cartilage by Low- and High-resolution MRI.

3.2.1 Sample Preparation

With the approval of the institutional review committees, nineteen mature canines were acquired from a dedicated facility, then quarantined onsite for two weeks with the proper care at the University of Calgary, Alberta. Prior to surgery, the conformation and gait of each animal was studied to exclude animals that had pre-existing anatomic or gait abnormalities. The surgical and care procedures, which are available upon request, satisfied the guidelines of the related regulatory agencies. Seven of the nineteen canines were non-operated healthy controls (N, 14 knees), and the rest of the twelve canines had the anterior cruciate ligament (ACL) in one knee transected 8 weeks (8OA, 6 knees) and 12 weeks (12OA, 6 knees) prior to sacrifice. The other knees in the surgical groups were untouched and labeled as the contralateral knee (8C and 12C, each 6 knees). After the excess tissues were trimmed off at sacrifice, all unopened knee capsules were imaged in a 7T MRI. Then each joint capsule was opened to harvest five rectangular cartilage-bone blocks from its medial tibia. Each block was about 3x3x5 mm^3 in size, representing a specific topographical location on the medial joint surface (Figure 3.1).

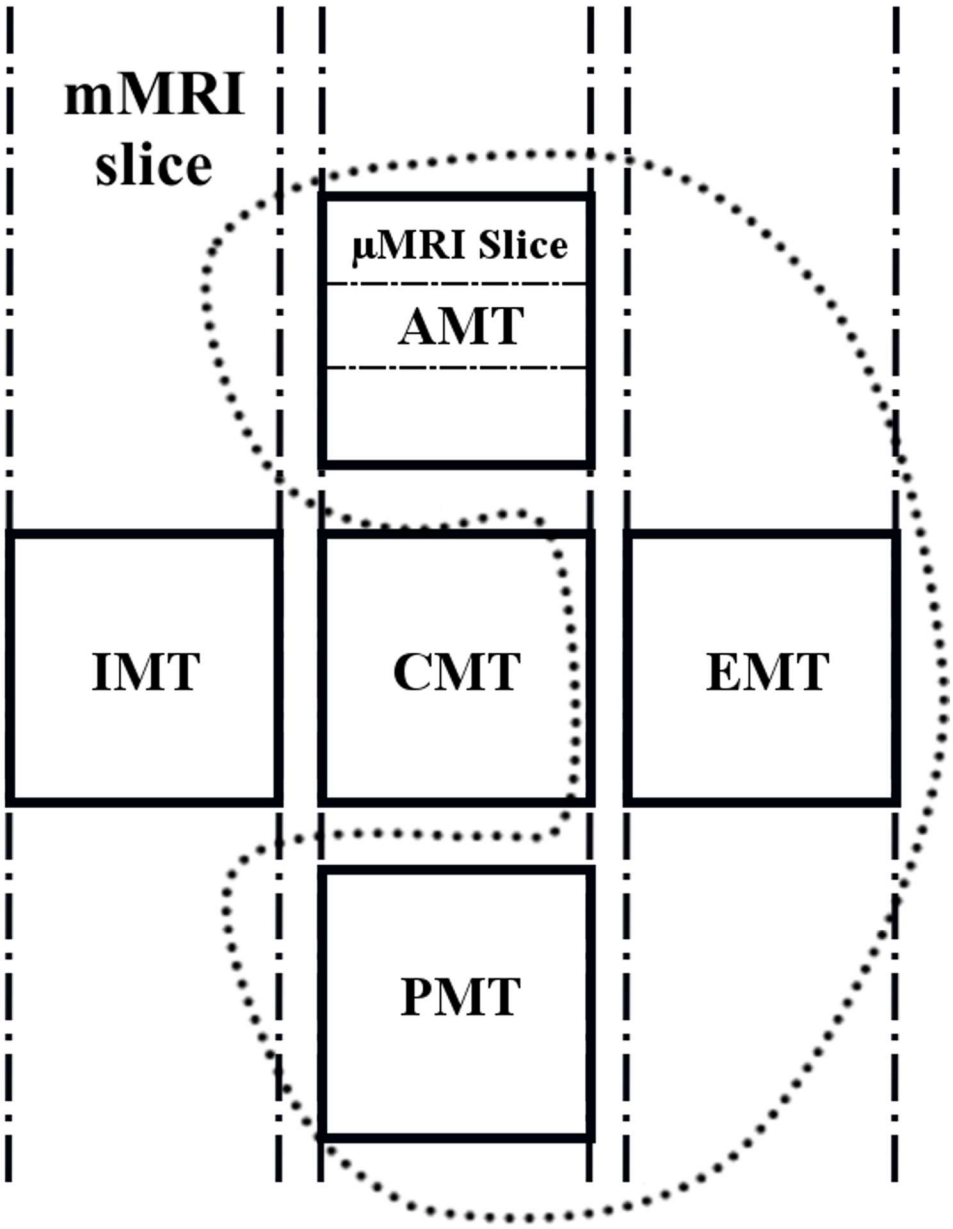

Figure 3.1 An illustrative topographic map of medial tibia joint divided into five locations (thick solid rectangular) representing each of the five cartilage bone plugs selected for µMRI studies. The five locations are labelled as Anterior (AMT), Exterior (EMT), Posterior (PMT), Central (CMT) and Interior (IMT) respectively. The dotted curved line represents the meniscus covered area in the medial tibial surface. Three mMRI slices are marked by the dot-dash lines that cover the five locations.

3.2.1 Low-Resolution MRI Protocols

All unopened knee capsules were imaged in quantitative MRI T2 experiments on a Varian MRI system with a 7T/20cm horizontal-bore magnet (Santa Clara, CA) and used the multi-slice multi-echo (MSME) pulse sequence. The FOV was 5cm with a matrix size of 256x256, which yielded a 200μm pixel size. These images were then interpolated in post-processing into 100μm per pixel size, which are labeled as macro-MRI (mMRI) in the remainder of this report. The repetition time was 3 sec; 10 echo times were used, with the minimum echo time of 10ms and each increment at 10ms with a total scan time of about 52 minutes. At each echo time, 10 slices were acquired, each with a slice thickness of 1mm (approx. 2.5mm apart from each other, running at interleaving sequences). Each joint thus had 100 T2*-weighted images, whose time-domain data were reconstructed (including zero padding) from a matrix size of 256x256 to 512x512, yielding the final pixel size of 100μm (Badar & Xia, 2017). Ten quantitative T2* images at 10 different slice locations were calculated based on these weighted images. The locations of three mMRI slices and the subsequent five μMRI cartilage-bone plug locations are shown in Figure 3.1.

3.2.3 High-Resolution MRI Protocol

All small specimens were immersed in physiological saline solution, which also contained 1mM Gd-DTPA^{2-} contrast agent and 1% protease inhibitor cocktail (Sigma, MO). The specimens were maintained at 4ºC (never frozen) and imaged quantitatively in a different 7T micro-MRI (Bruker AVANCE II 300 micro-imager). The acquisition matrix was 256x128, which was reconstructed into 256x256 matrix, resulting in a pixel size of 17.6 μm (labeled as μMRI). The field of view was 4.5 mm with a slice thickness

of 0.8 mm. The repetition time (TR) was set at 500 as all samples were soaked in Gd-DTPA^{2-} (for T_1 experiments). The T2-weighted images were acquired using a CPMG magnetization-prepared imaging sequence with five echo times (2, 8, 20, 50, and 100 ms) and total scan time of approximately 1 hour and 30 minutes (Xia, 1998; Zheng & Xia, 2009b).

Two sets of μMRI images were acquired for each specimen with the normal axis to the cartilage surface being oriented at 0º and 55º to the external magnetic B0 field, which were used to calculate two orientation-dependent T2 images. These two orientations in the quantitative T2 imaging were necessary since T2 characteristic in articular cartilage is known to have strong magic angle effect (Xia, 1998, 2000b), which has its origin in the dipolar interaction in spin dynamics. The angles of 0º and 55º to the external magnetic field are the two orientations that give the maximum and minimum influence of the dipolar interaction to the depth-dependent T2 characteristics.

3.2.4 Image and Statistical Analysis

The high-resolution T2 profiles in μMRI were divided into four zones using a well-established method of zonal division (Lee & Xia, 2013; Xia et al., 2001), where the bell-shaped curve of a depth-dependent T2 profile (0º) is divided into four individual zones. The division for the low-resolution profile in mMRI considered the fact that the average thickness of SZ and TZ was each 80-120μm for this type of canine tissue (Lee et al., 2014; Xia, Wang, Lee, & Badar, 2011), hence assigning the first and second pixels as SZ and TZ for mMRI respectively, with the rest of the profiles as the two equal parts of RZ (RZI and RZII). Both mMRI and μMRI quantitative T2 maps were calculated using a single exponential decay on pixel-by-pixel basis with the aid of a MATLAB code. The

exponential decay equation used in the code allows for a more rigorous calculation of T2. Further explanation of the single exponential model using MATLAB (and other software) is presented in Appendix B of the dissertation.

One-way ANOVA with Bonferroni correction test using KaleidaGraph was performed on all specimens from each of the five topographical locations (AMT, EMT, PMT, CMT and IMT) of the medial tibia, comparing T2 relaxation times among healthy (N), contralateral (8C and 12C) and osteoarthritic (8OA and 12OA) cartilage in each of four unequal-thickness zones (SZ, TZ, RZI and RZII) by mMRI and μMRI (0º and 55º). Pairwise statistical tests were also carried out between healthy (N) and both contralateral joints (8C and 12C), and between healthy (N) and both osteoarthritic joints (8OA and 12OA). Pairwise statistical comparisons were also carried out between comparable disease groups. A resultant p-value of less than 0.05 was considered significant.

3.3 The Interface Region Between Articular Cartilage and Bone by μMRI and PLM at Microscopic Resolution

3.3.1 Sample Preparation

Five cartilage-bone rectangular plugs (~3x3x5 mm^3) were extracted from the central region of a healthy canine humeral head. The animal was sacrificed for an unrelated biomedical study, which was approved by the relevant Institutional Review Committee. The intact joint was frozen immediately at -80°C after euthanizing and thawed at 4°C before the specimen harvesting. Nearly identical canine humeral cartilage-bone specimens, which were from the same tissue source over the last 25 years, have been studied in our lab for numerous micro-imaging projects across multiple imaging

modalities (Badar et al., 2021; Lee & Xia, 2013; Xia, 2008; Xia, Farquhar, Burton-Wurster, & Lust, 1997; Zheng, Xia, & Badar, 2011).

3.3.2 μMRI Experimental Setup

The μMRI system (Oakland University, MI) used in this work was a Bruker AVANCE IIIHD console and a 7 Tesla/89 mm vertical-bore superconducting magnet, together with the micro-imaging accessory and a 3mm solenoid coil (Bruker, Billerica, MA). Three 2D imaging sequences were used, a gradient echo (GE) sequence, a magnetized-prepared spin-echo (Mprep.SE) sequence and a UTE sequence, to collect T2 data of the cartilage-bone specimens at both 0º and 55º (magic-angle) orientations with respect to the external magnetic field B_0. (Note that GE and UTE sequences generate T2* data instead of T2 data. To simplify the labeling, we use T2 in the dissertation.) Two orientations in the quantitative T2 imaging were necessary since T2 characteristics in articular cartilage are known to have the magic angle effect (Xia, 1998), which has its origin in the dipolar Hamiltonian in spin dynamics. The angles of 0º and 55º to the B_0 are the two orientations that give the maximum and minimum influences on the depth dependent T2 characteristics, yielding the T2 anisotropy in articular cartilage. All three sequences used the same geometry settings, with a FOV of 3 mm and a matrix size of 256x128 (post-reconstruct to 256x256; for GE and Mprep.SE) and 256x256 for UTE, yielding a 11.7 μm/pixel resolution for all three imaging sequences. All μMRI sequences used a slice thickness of 1mm. The GE sequence used a TR of 2000 ms and had five echo times (TE) of 7, 14, 21, 28 and 35 ms. The Mprep.SE sequence used a CPMG T2 contrast header segment (Zheng & Xia, 2009a) that used a TR of 2000 ms and had five TEc of 2, 8, 20, 40 and 60 ms. The UTE sequence used a TR of 100ms and had five echo times at

0.235, 0.3, 0.5, 0.6 and 1 ms. To avoid intensity saturation between individual UTE proton maps due to changing receiver gain and parameters, the identical receiver gain, and parameters were set for each of the individual UTE experiments. To quantify T2 in SE and T2* for GE and UTE in non-calcified and calcified cartilage, a single exponential fit to the image intensities was carried out for all ROIs, with a variable baseline ($S = S_0 + \alpha * e^{(-TEc/T2)}$, where S_0 is the average noise (baseline) selected from a region outside the tube and α is the maximum intensity measured minus the baseline (S_0) at the earliest TEc). Further explanation of the single exponential model using MATLAB (and other software) is presented in Appendix B of the dissertation.

3.3.3 Histological and Optical Imaging Setup

To correlate between μMRI and PLM, the cartilage-bone specimens imaged first by μMRI were fixated in 10% neutral buffered formalin overnight at 4°C. The fixated cartilage-bone specimens were sent to a histology service (Yale Pathology Tissue Services, New Haven, CT) to section into 6 μm slices using the paraffin method. Multiple slices from the five individual specimens were processed through histology; adjacent slices were alternatively either unstained (for quantitative PLM) or processed with the Hematoxylin and Eosin (H&E) staining protocol (for qualitative visualization of ZCC). All unstained slices were imaged in our lab by a quantitative PLM system, which consists of a digital setup (Cambridge Research & Instrumentation, Woburn, MA) that is mounted on a polarized light microscope (Leica, Buffalo Grove, IL). The output of the CCD camera was processed to generate two quantitative images: the optical retardation (in units of nm) that describes the voxel averaged collagen organization and the azimuth (in units of degº) that quantifies the voxel average collagen orientation (Oldenbourg & Mei,

1995). A selected number of slices were imaged multiple times at different magnifications. With the use of a 5x, 10x, 20x, or 40x objective, our PLM system has pixel resolutions of 2 μm, 1 μm, 0.5 μm, or 0.25 μm, respectively. The H&E-stained sections were imaged by the same optical microscopy and captured by a Canon Rebel T4i digital camera. The H&E images were taken using white light in the Leica microscope and the camera in manual mode using fixed settings to avoid any intensity variation from one image capture to another. The color images of the H&E-stained sections were adjusted by correcting the hue and saturation levels with the help of the ImageJ software, to differentiate the ZCC better visually from the NCC and SBP. The pixel sizes in the Canon images were calibrated with the use of a resolution scale to match the pixel sizes of the quantitative PLM images.

3.3.4 Data and Statistical Analysis

For the exponential fitting, a region of interest (ROI) was selected in each zone (SZ, TZ, RZ1, RZ2 and ZCC) of the specimen from which the average signal at each TEc was collected. The single exponential fit was used to calculate the T2 or T2* (with the error E and goodness of fit (R2)). From the average of five cartilage-bone plugs, a profile plot was calculated using a ten-pixel ROI selected from the center of each μMRI T2 map (both 0º and 55º sample orientations) which covered the entire thickness of cartilage and extended into SBP. A one-dimensional (1D) profile from the selected 2D ROI was generated by row-wise averaging (together with the standard error) along the cartilage depth. For each quantitative PLM image, an ROI containing 60 parallel neighboring columns, which would have approximately the same width as the ROI thickness in μMRI, were averaged to produce one 1D profile. Since the averaging was row-wise, the

spatial resolutions of the 1D profiles along the tissue depth are 11.7 μm for μMRI and 2 μm for PLM. All 2D images and 1D profiles, where each came from one independent imaging experiment, used the identical scaling and settings without any additional manual adjustment. The post-acquisition image and statistical analyses used the public-domain software ImageJ and the commercial software KaleidaGraph. A one-way ANOVA with Bonferroni correction was used to compare the 0º and 55º mean UTE-T2* values in the ZCC ($p < 0.05$ was considered significant).

CHAPTER FOUR

IMAGE INTERPOLATION IMPROVES THE ZONAL ANALYSIS OF CARTILAGE T2 RELAXATION IN MRI

4.1 Introduction

Morphological changes of articular cartilage due to osteoarthritis can be detected by several clinical MRI sequences such as T2 and T2 anisotropy, T1ρ, T1 (with the use of contrast agent), and diffusion (Alhadlaq et al., 2004; Matzat et al., 2014; Newbould, Miller, Toms, et al., 2012; Regatte et al., 2006; Smith et al., 2001; Welsch et al., 2008). Early OA detection using MRI, however, remains unsatisfactory in the clinic. A major reason for this inadequate clinical diagnosis is the relatively large voxel size in comparison with the thin thickness of articular cartilage over which the molecular concentration and orientation changes are significant (Xia, 2007). Consequently, several changes can occur in the tissue simultaneously, for example, due to topographical distributions of the collagen orientation and proteoglycan concentration, natural wear and tear, or degradation due to non-physiological activities (i.e., impacts during sport, work, or battlefield). At the current standard of clinical whole-body scanners, detection of these changes is inadequate for the best and earliest diagnosis of OA.

This chapter describes a multi-resolution imaging study of canine tibial cartilage that had surgically induced OA. First, the T2 images of intact knees were acquired at 200 μm pixel resolution, which mimicked the resolution obtainable in clinical MRI of human joints. The joints were subsequently opened and the cartilage-bone specimens at the locations that were imaged previously were harvested and imaged again at 17.6 μm pixel

resolution. 2D T2 maps were calculated from both MRI experiments. We applied an image interpolation algorithm to investigate whether the reconstruction of the 200 μm images to 100 μm images could improve the detection sensitivity in MRI. Since the most important feature of cartilage degradation is its depth-dependent zonal divisions, we aimed to investigate if different interpolating and zonal division methods could improve the detection of early OA.

4.2 Results

4.2.1 Multi-Resolution T2 Maps

A T2 map of a healthy medial tibia using the 7T macro-MRI imaged at the resolution of 200 μm/pixel (Figure 4.1a) showed the pixilation of a low-resolution whole joint image that is commonly seen in clinical MRI. The white region of interest (ROI) box depicted the region on the tibia from which a cartilage-bone specimen was later imaged at 17.6 μm/pixel in μMRI. Just like the original image (Figure 4.1b), similar ROIs were selected from the reconstructed images (100 μm/pixel) by two different types of interpolation methods: the ImageJ reconstruction (Figure 4.1c) and the FID reconstruction (Figure 4.1d). Both reconstruction methods clearly produced smoother images (Figures 4.1c and 1d) that are lesser pixelated than the original image (Figure 4.1b) with minor differences in the different regions of the joint. The smaller ROI within Figures 4.1b-1d depict ROIs from which depth-dependent T2 profile analyses were performed and a similar location from which μMRI data were analyzed.

4.2.2 Multi-Resolution T2 Profiles

From the two-dimensional T2 maps, the depth-dependent T2 profiles for both healthy and OA cartilage (Figure 4.2a) were extracted from the ROI, with and without the

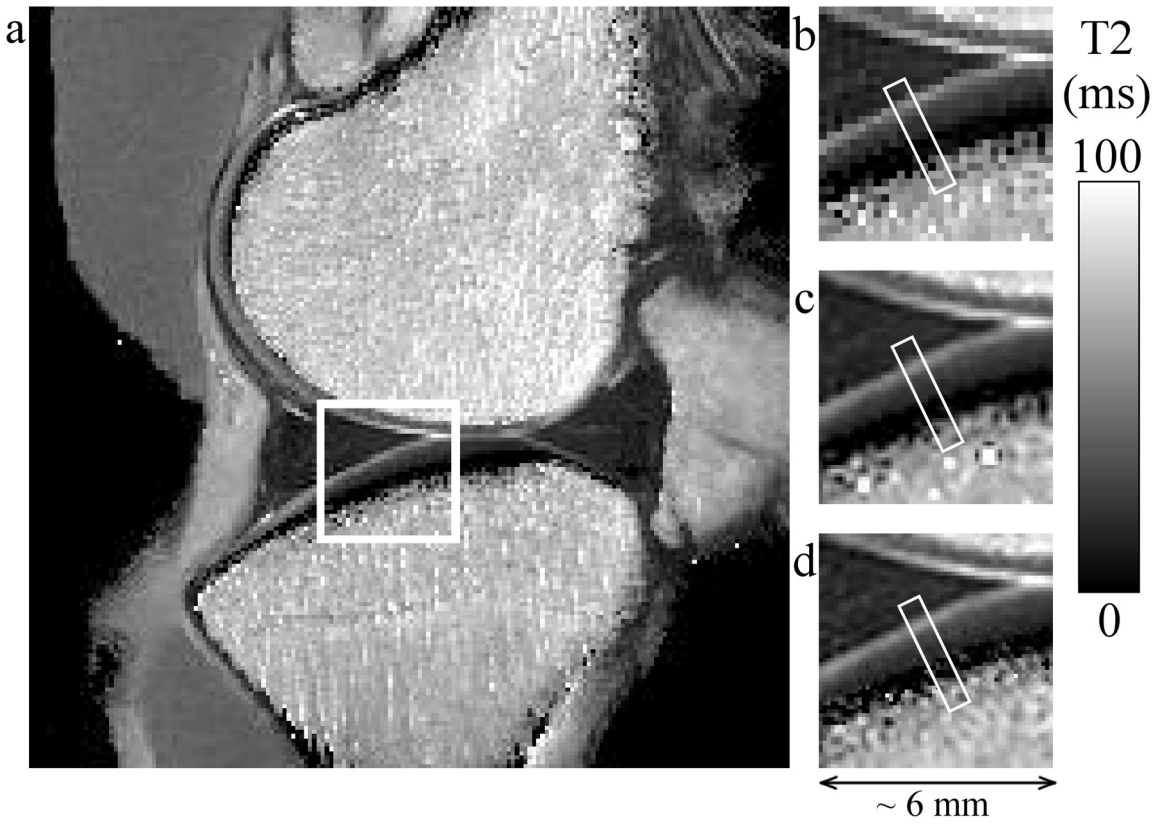

Figure 4.1 Macro-MRI T2 map of a healthy canine medial tibia. (a) Quantitative T2 images of a canine medial tibia from macro-MRI in a sagittal slice. The white square shows the selected ROI, which is enlarged on the right: (b) the ROI with the original resolution (~ 200μm/pixel), (c) the ROI with the bicubic interpolated resolution (100μm/pixel) in ImageJ software, and (d) the ROI with the FID-based reconstructed resolution (100μm/pixel) in the Varian NMR spectrometer. The white rectangle on b, c and d represent the ROI selected for depth-dependent profiles. The 0 to 100ms gray scale is used for all images.

image interpolation. Even though the images in Figures 4.1c and 1d had slight overall differences, the profiles showed near identicalness of the two interpolation methods as well the resolution difference between the original image and the interpolated images. The horizontal error bars in the original (256) T2 profile showed the pixel location at 200 μm and the site reference to the pixel locations at 100μm. Since a 200 μm pixel is substantial in size when compared with the cartilage thickness (about 600-1000 μm), the T2 value at 200 μm/pixel was placed in the middle of each large voxel in the horizontal scale (i.e., at the 100 μm location), as a representation of an average T2 value of the finite-sized voxel. For the 100 μm pixels, the T2 values were placed at the beginning, mid-point, and end of each 256-pixel location. The most significant difference in T2 between healthy and OA cartilage is shown to occur near the top 20% of the tissue (Figure 4.2a). A careful inspection of the error bars and the comparison of the interpolated images using both methods showed that the time-domain (FID) reconstruction resulted in a slightly less noisy profile, and as such, was used for the rest of the analysis.

Comparison between the macro-MRI T2 profile of healthy cartilage (N), which were harvested from the ROI shown in Figure 4.1a, and their equivalent μMRI T2 profiles (Figure 4.2b) showed significant similarity. The high-resolution μMRI data showed significantly more information in terms of the depth-dependency of cartilage T2 when compared to the macro-MRI data. The zonal markings on the μMRI profiles clearly indicated the resolution differences between the macro-MRI (~200 and 100 μm) and μMRI (~20 μm). This comparison demonstrated that the missing information in the low-resolution MRI is mainly in the top 20% of the cartilage in a typical clinical MRI setting.

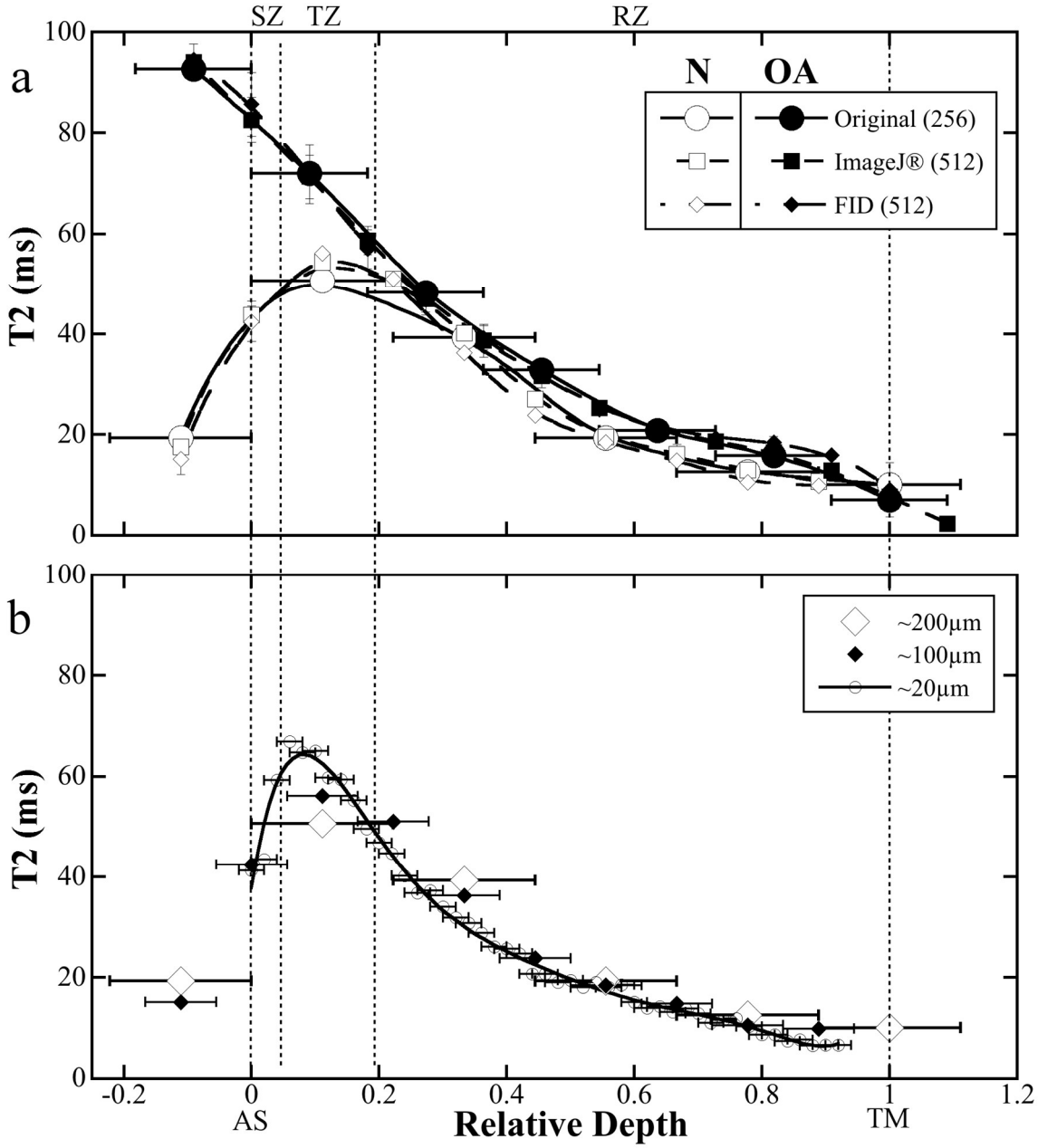

Figure 4.2 T2 comparison of healthy and OA cartilage using different interpolation and resolution methods. (a) The depth-dependent T2 profiles of healthy (N) cartilage (a) and OA cartilage (b) depicting the influence of different image interpolation, shown in Fig 1(b)-(d). The articular surface (AS) is marked with 0 and the cartilage-bone interface (TM) with 1. (b) The depth-dependent T2 profiles of healthy cartilage between µMRI (~20µm/pixel) and macro-MRI (both original and interpolated pixel sizes) with tissue divided into the three distinct zones: Superficial (SZ), Transitional (TZ) and Radial (RZ) zones.

This missing information would depend on the ROI selection and the partial volume effect, which are critical for the early OA detection. The subtle yet critical difference between the 200 μm and 100 μm T2 profiles (N, healthy) where the 100 μm profile showed the lamina effect that is evident also in the 20 μm T2 profile (Xia, 2005; Xia et al., 1997). This difference is also documented in Table 4.1 in the unequal division of zone column (in bold) where the T2 pattern for 200 μm is SZ > TZ > RZ whereas the 100 μm follows a pattern of TZ > SZ > RZ, similar to the findings of healthy tissue T2 profiles in μMRI. This is a key finding in the importance of the reconstruction and minimum resolution needed for zonal division.

4.2.3 Statistical Comparison of Low- and High-Resolution T2 MRI Data

T2 profiles of the images at 200 μm/pixel resolution (Figure 4.3) and the "time-domain" interpolated images at 100 μm/pixel resolution (Figure 4.4) showed statistical findings among three different division methods (the two equal-thickness division, the three equal-thickness division, and the three unequal-thickness zones), and among three types of cartilage (healthy, contralateral, OA).

Table 4.1 summarizes the statistical findings (shown in Figure 4.3 and Figure 4.4) as mean and standard error of the mean (SEM) with their respective statistical p-values. Several conclusions can be drawn from the comparisons of the three division methods based on the strong statistical results.

1. The subtle differences between the 200 μm/pixel data (Figure 4.3) and the 100 μm/pixel data (Figure 4.4) show that the image interpolation can improve the OA detection by MRI T2, even when the imaging resolution is still insufficient to resolve the structural zones in cartilage. This is best illustrated in the three equal-

thickness division (Figure 4.4.b), where the middle 1/3 gains T2 sensitivities to OA after image interpolation.

2. Comparing the two and three equal-thickness division methods (Figure 4.3a/4.4a vs. Figure 4.3b/4.4b), it is clear that the three equal-division method is more sensitive than the two equal-division – it is capable of picking up the differences between healthy and contralateral cartilage, as well as between contralateral and OA cartilage when the image interpolation is used. This shows the improvement of image resolution, in both acquisition and analysis, should be the top priority in clinical MRI development.
3. The more revealing division method is the unequal-thickness zonal division, which requires the knowledge of the true zonal structure in cartilage, obtainable only by histology or μMRI. This unequal zonal division is capable of detecting the T2 changes not only between healthy and OA cartilage, but also between healthy to contralateral cartilage (Figure 4.3c and Figure 4.4c), in both 200 μm/pixel and 100 μm/pixel images. The latter difference between healthy and contralateral cartilage in SZ cannot be seen in any of the equally divided regional analysis (Figure 4.3a-b and 4.4a-b) at both resolutions (200 μm and 100 μm). This is a significant finding.

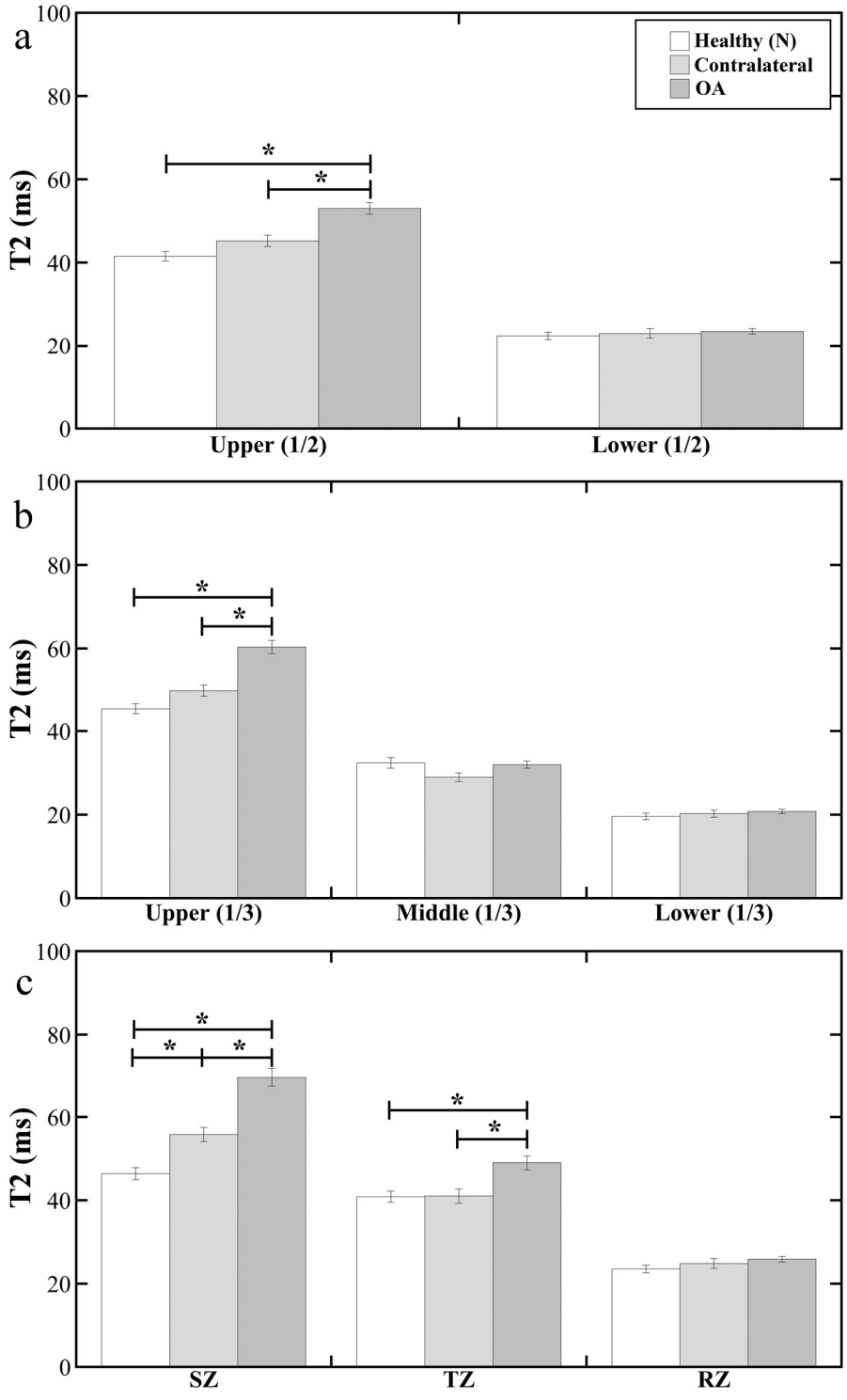

Figure 4.3 Statistical comparison between healthy (N), contralateral and OA groups based on the two equal (a), three equal (b) and three unequal (c) division of the T2 profiles at 200μm resolution. The statistical significances are donated as * (<0.01).

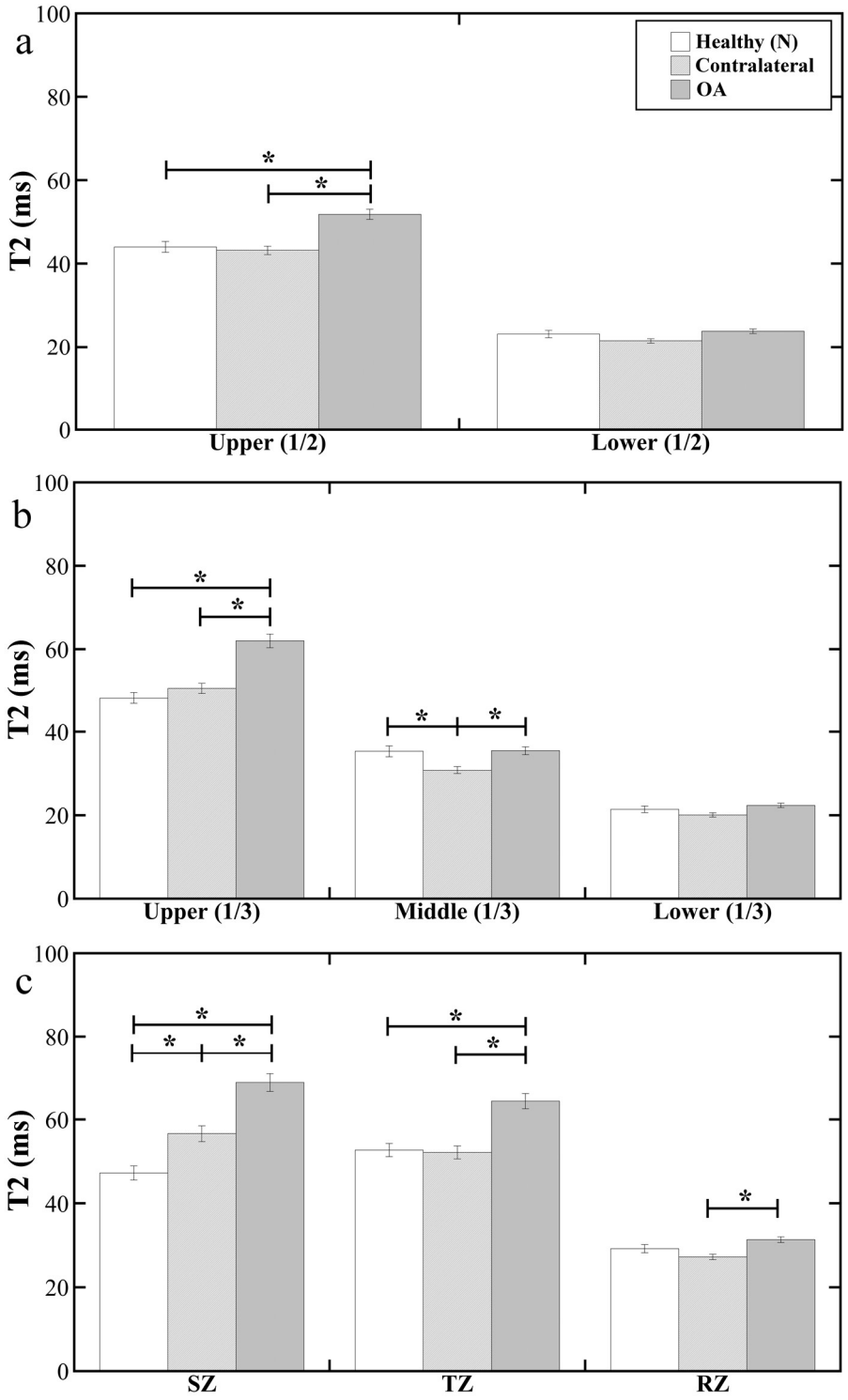

Figure 4.4 Statistical comparison between healthy (N), contralateral and OA groups based on the two equal (a), three equal (b) and three unequal (c) division of the T2 profiles at 100μm resolution. The statistical significances are donated as * (<0.01)

Table 4.1 T2 values comparing healthy (N), contralateral (C) and OA cartilage (mean ± SEM) at two resolutions using the three methods of tissue division; namely two-equal, three-equal, and three-unequal divisions (using "FID 512" method).

			mean ± SEM (ms)			p-value			
Resolution	**Method**	**Zone**	**N**	**C**	**OA**	**ANOVA**	**N v. C**	**N v. OA**	**C v. OA**
200 µm	Two Equal Division	Upper (1/2)	41.66 ± 1.19	45.23 ± 1.35	53.06 ± 1.41	**< .0001**	0.1257	**< .0001**	**0.0001**
		Lower (1/2)	22.39 ± 0.87	23.01 ± 1.12	23.49 ± 0.66	0.6902	0.8834	0.6659	0.9212
	Three Equal Division	Upper (1/3)	45.33 ± 1.21	49.91 ± 1.34	60.37 ± 1.57	**< .0001**	0.0524	**< .0001**	**< .0001**
		Middle (1/3)	32.37 ± 1.26	28.98 ± 1.03	31.99 ± 0.87	0.3074	0.3241	0.9696	0.4545
		Lower (1/3)	19.62 ± 0.78	20.28 ± 0.89	20.79 ± 0.55	0.3172	0.3161	0.4943	0.9436
	Three Unequal Division	SZ	**46.38 ± 1.46**	55.82 ± 1.69	69.54 ± 2.14	**< .0001**	**0.0008**	**< .0001**	**< .0001**
		TZ	**40.86 ± 1.35**	41.08 ± 1.69	49.03 ± 1.70	**0.0003**	0.995	**0.0011**	**0.0015**
		RZ	**23.52 ± 0.93**	24.84 ± 1.19	25.85 ± 0.71	0.2408	0.6047	0.2113	0.7357
100 µm	Two Equal Division	Upper (1/2)	44.02 ± 1.28	43.21 ± 1.01	51.86 ± 1.22	**< .0001**	0.8773	**< .0001**	**< .0001**
		Lower (1/2)	23.14 ± 0.87	21.52 ± 0.51	23.82 ± 0.53	0.0422	0.1915	0.7494	0.0383
	Three Equal Division	Upper (1/3)	48.25 ± 1.40	50.62 ± 1.22	62.03 ± 1.63	**< .0001**	0.4704	**< .0001**	**< .0001**
		Middle (1/3)	35.31 ± 1.29	30.81 ± 0.84	35.47 ± 0.95	**0.0020**	**0.0074**	0.9934	**0.0053**
		Lower (1/3)	21.42 ± 0.79	20.07 ± 0.51	22.36 ± 0.49	0.0325	0.2697	0.5286	0.0251
	Three Unequal Division	SZ	**47.26 ± 1.69**	56.62 ± 1.87	68.85 ± 2.11	**< .0001**	**0.0018**	**< .0001**	**< .0001**
		TZ	**52.74 ± 1.56**	52.16 ± 1.53	64.39 ± 1.78	**< .0001**	0.9657	**< .0001**	**< .0001**
		RZ	**29.21 ± 0.98**	27.23 ± 0.67	31.37 ± 0.71	**0.0016**	0.1923	0.1389	**0.0010**

* p-value < 0.01 was considered statistically significant (Sample size of 60 for each N, C and OA samples).

4.3 Discussion

It is rare that one has the opportunity to study approximately the same cartilage specimens using both macro-MRI at 200 μm resolution and μMRI at 17.6 μm resolution, quantitatively, with the same MRI parameter (T2 relaxation), at the same field strength (7T), and with both healthy and well-characterized osteoarthritis. Given our extensive experience with similar canine cartilage at microscopic resolutions (Alhadlaq et al., 2004; Lee et al., 2016; Mittelstaedt, Kahn, & Xia, 2016; Xia et al., 2001), the multidisciplinary properties of this type of cartilage are well understood. Our study of canine tibial cartilage at 200 μm per pixel by macro-MRI has approximately the same length scale in comparison to the clinical MRI of a thicker human tibial cartilage at a fraction of millimeters per pixel using a whole-body MRI scanner, both resolving about 3 pixels across the thickness of cartilage based on the clinical settings implemented. Consequently, this animal MRI study and the common human MRI scans share a similar structural averaging in cartilage within each depth-dependent pixel, as well as the averaging between cartilage and its surrounding tissues (Xia, 2007). Since T2 is an important indicator in MRI study of cartilage damage due to OA (Lee et al., 2016; Wei et al., 2015; Wyatt et al., 2015), this project could help better illustrate the issues of MRI resolution at early stages of osteoarthritic cartilage.

4.3.1 The Zonal Thickness Approximation

Some of the early lesions in human OA can be localized near/around the surface of the tissue (Hwang et al., 1992). The averaging of the surface tissue in diagnostic imaging could therefore hide vital information that is essential to the detection of early OA. Many clinical MRI analyses often compare just one bulk T2 value between the healthy and OA

cartilage (Chang et al., 2013; Ross et al., 2012). With the improvement of clinical MRI technology, resolving cartilage thickness in 2-4 or more pixels becomes possible for quantitative human MRI (Bangerter, Taylor, Tarbox, Palmer, & Park, 2016). Consequently, these pixels of equal size could be used to represent different depths of cartilage (Shao et al., 2016; Welsch et al., 2009). This type of depth-dependent regional analysis is superior to the bulk analysis since a regional analysis separates the different characteristics between surface and deep cartilage. Since the combined thickness of both SZ and TZ is likely less than 1/3 of the total thickness, an equal thickness division essentially groups the complex surface structures of cartilage into one pixel, which could mask subtle changes of T2 in early OA (Figure 4.2). This project clearly demonstrates the additional detection sensitivity gained from the image interpolation, even when the original data is inadequate to resolve the zonal structure of cartilage. The approach in this animal cartilage study could be equally applied to clinical MRI of human cartilage, based on the scaling of imaging resolution in MRI (Xia, 2007).

This study has benefited from the knowledge from μMRI T2 profiles of the same cartilage (Lee et al., 2014; Lee et al., 2015; Lee et al., 2016), which clearly indicate the strong and distinct zonal profiles of cartilage T2 over its thickness, especially near the surface. Proper zonal division permits the best separation of Superficial and Transitional zones, which increases the sensitivity of the MRI protocol. This study therefore calls for the determination of the minimum resolution required for MRI of osteoarthritic cartilage. This determination, however, can be complicated in practice by the heterogeneity of the zonal structures in cartilage over a joint surface such as tibia or femur (Appleyard et al., 2003), as well as the dimension and orientation of the imaging voxel, which is commonly

non-isotropic (Xia et al., 2001). By averaging only within each zone, a much better detection of the morphological changes occurring in early OA cartilage can be obtained.

4.3.2 Minimal Resolution Requirements for Articular Cartilage

In the post-acquisition image interpolation from the original 256 matrix to a 512 matrix, two different reconstruction methods showed minimal difference. This result is beneficial to most users since few could have repeated access to the original MRI system after the data acquisition. Since the scaling factor of two was used in both interpolation methods, the quantitative information from the interpolation is sufficiently within the limitations reported by other image interpolation studies where interpolation showed a statistical improvement in structural changes and reduction of partial volume effect (Bernstein, Fain, & Riederer, 2001; Du, Parker, Davis, & Cao, 1994; Mayerhoefer et al., 2009). For canine tibial cartilage, a minimum resolution of 100μm/pixel is both necessary and sufficient, since μMRI results at a much higher resolution showed the thinnest zones were about 80-100μm in thickness (Zhuang, Lee, Badar, Xu, & Xia, 2016).

4.3.3 Experimental and Analytical Limitations

One methodological consideration in this data analysis is the location of the T2 values on the depth scale of cartilage. We placed the T2 values at the center of the pixels in the depth scale (at 100 μm, 300 μm, and so on). Arguments could be formulated to place the T2 value at the upper edge of the pixels (at 0μm, 200 μm, and so on). Since the voxel size is large in comparison with the collagen structure in cartilage, the partial volume effect is an important factor when deciding the depth location of the first pixel of the tissue (Liu, Chaudhary, Block, Samsonov, & Kijowski, 2015). We recommend that if the depth-dependent analysis approach is consistent, which merely represent a relative

shift of the relaxation profile, the analysis should result in a similar conclusion. However, it does leave an ambiguity in the profile matching, as the selection is user dependent. Since the shape of a MRI voxel is commonly elongated (Xia, 2007), the averaging of the surface reflects the contribution not only from different cartilage but also some surrounding tissues. This is represented by the surface portion of the T2 profiles in Figure 4.2a, which include two possible scenarios, that is, whether the T2 values in the adjacent non-cartilage regions is lower or higher than the T2 values of the first cartilage pixel.

4.3.4 Conclusion

We demonstrate that the interpolation of T2 images can better detect OA in cartilage, in the situation when the MRI resolution is insufficient to resolve the depth-dependent T2 characteristics in articular cartilage. Several zonal divisions of articular cartilage were compared using quantitative macro-MRI data. An unequal zonal division is shown to be much more statistically informative than the typical equal thickness division used in low-resolution MRI and hence able to detect earlier signs of T2 changes due to OA. Since the relative length scale of canine cartilage and macro-MRI is nearly identical to those of human cartilage and whole-body MRI, this image analysis approach can benefit the clinical detection of early OA in humans.

CHAPTER 5

TOPOGRAPHICAL AND ZONAL PATTERNS OF T2 RELAXATION IN OSTEOARTHRITIC TIBIAL CARTILAGE BY LOW- AND HIGH-RESOLUTION

5.1 Introduction

The degradation of cartilage is the hallmark of osteoarthritis (OA), which is the most common musculoskeletal disease that affects millions of people in our society (Buckland-Wright, Macfarlane, Lynch, et al., 1995; Huang & Schweitzer, 2014; Matyas et al., 1999; Vignon et al., 2003; Watson et al., 1996). Given the zonal and topographical natures of cartilage properties, cartilage degradation must have zonal and topographical signatures at different stages of OA during its slow progression (Kahn et al., 2016). The fact that articular cartilage is a thin layer of curved tissue with both topographical and zonal variabilities make the detection of early OA progression challenging. Among the non-invasive imaging tools in clinics, magnetic resonance imaging (MRI) is the only technique that has the sensitivity to the motion of molecules in soft tissue (Wang & Xia, 2013). Several MRI parameters, in particular T2 relaxation time, have been widely used for the diagnostic assessment of OA cartilage (Alhadlaq & Xia, 2004; Kurkijarvi et al., 2004; Lee et al., 2015). In biological tissues, T2 relaxation has complex mechanisms that reflect the mobility of water molecules in their local environments, which can be used to monitor the anisotropic properties in cartilage and other collagen-rich tissues (Xia, 1998; Xia et al., 2012). For the simplest notion in relation to osteoarthritis cartilage, a high T2 value implies a tissue having less proteoglycans, less organized collagen matrix, more extracellular water, and looser interactions between water and macromolecules

(Blumenkrantz et al., 2008; Hannila et al., 2009; Hanninen et al., 2017; Li et al., 2007; Millington et al., 2007; Stahl et al., 2007).

In this project that used a canine model of OA, the degradation of cartilage was triggered by anterior cruciate ligament (ACL) transection surgery (Matyas, Atley, Ionescu, Eyre, & Poole, 2004; McDevitt et al., 1977) and studied at 8-weeks and 12-weeks after the surgery. There were five types of tissue: healthy cartilage, OA cartilage 8-weeks and 12-weeks after surgery, and contralateral cartilage 8-weeks and 12-weeks after surgery. Cartilage from five topographical locations on the medial tibial plateau was studied by MRI T2 protocols, each with two zonal resolutions (100μm/pixel and 17.6μm/pixel). We aimed to investigate the interactions on the MRI T2 OA detection by different disease progression, at different topographical locations, in different sub-tissue zones, and using different imaging protocols.

5.2 Results

5.2.1 The mMRI and μMRI Images and Profiles

Figure 5.1 shows the locations of the mMRI and μMRI slices, from which the T2 of cartilage was measured quantitatively. The central mMRI slice (#2) captured three locations from anterior to posterior (AMT, CMT and PMT), where each topographical location was studied individually in μMRI. Figures 5.1a/d/g show three identically located mMRI slices from three specimen groups (N, 8OA, 12OA); all had the colored T2 images of cartilage overlaid on the grey-scale intensity images of knee joint, together with the corresponding μMRI T2 maps at 0º and 55º orientations. With the progression of the tissue lesion from healthy (N) to two OA stages (8OA, 12OA), an incremental increase in both T2 and tissue thickness can be seen clearly, with the 12OA tissue

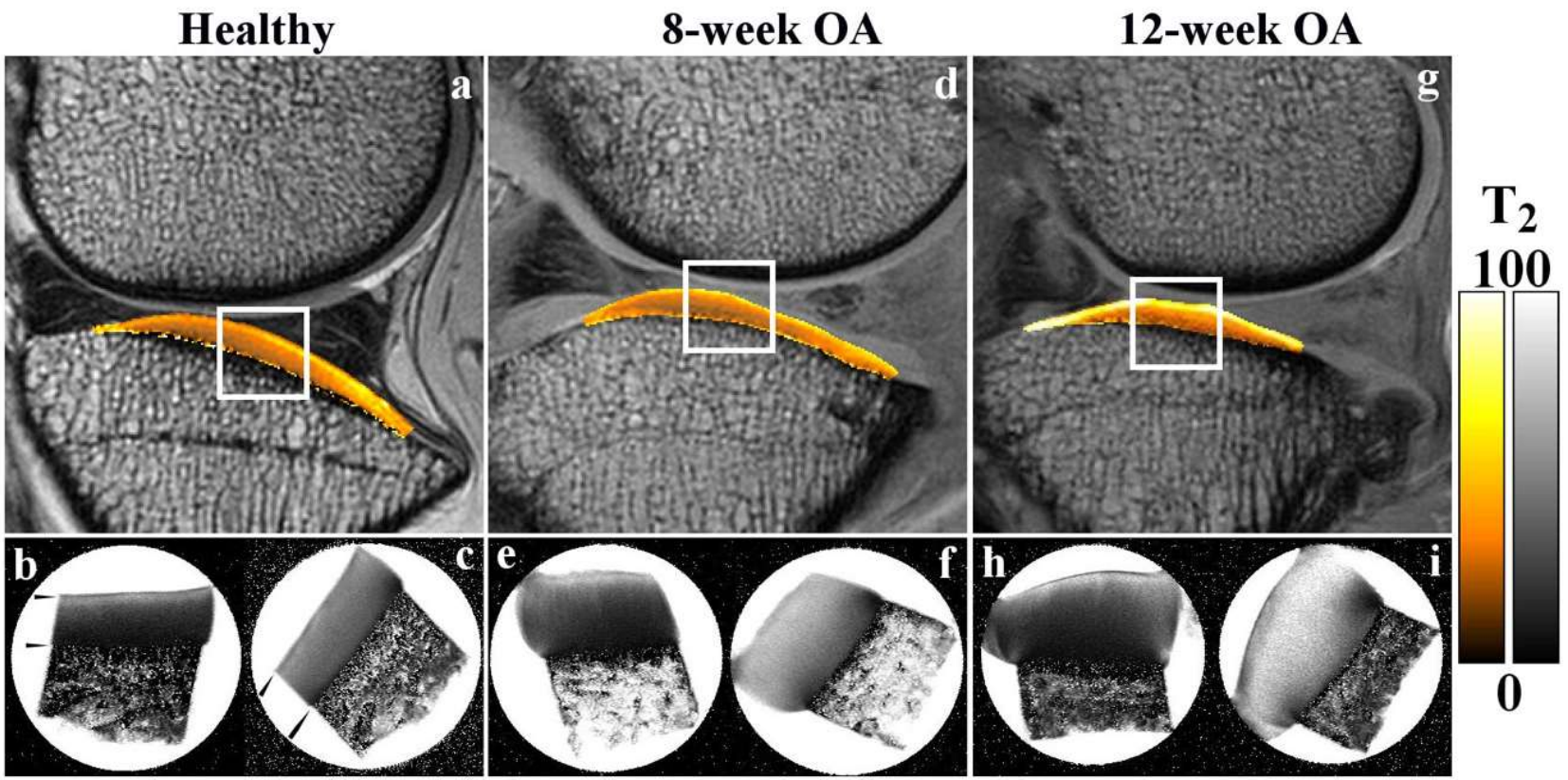

Figure 5.1 The mMRI images (a, d, g) of three intact knee joints representing the Normal, 8OA and 12OA animals, overlaid by their quantitative T2 maps (colored, 0-100ms). The mMRI ROI (the white box) shows the approximate region where the cartilage-bone plugs were harvested for the μMRI 0º and 55º imaging, which were shown under each knee image. The arrow heads in (b) and (c) mark the thickness of articular cartilage. The direction of the magnetic field B0 is pointing vertically up in the figure; the angles of 0º and 55º are between the normal axis of the articular surface and the magnetic field direction.

showing the biggest T2 increases (Figure 5.1g) and the clearest swelling in cartilage across the entire tibial sagittal slice (Figures 5.1h and 1i). The phenomenon of tissue swelling in μMRI clearly indicates that at these degradation stages, (a) there are disintegrations of the collagen network in 8OA and 12OA tissues, and (b) cartilage still contains measurable PG even at 12OA. These mMRI changes vary topographically from one surface location to another, illustrating the fact that not all cartilage degrades simultaneously. Hence, a topographical view with zonal resolution is crucial for accurate diagnostic study of early OA by any imaging tool.

Figure 5.2 shows the depth-dependent T2 profiles at one tibial site (CMT), comparing healthy cartilage with the OA cartilage. The comparative plots used a relative thickness to accommodate varying tissue thickness due to tissue swelling. The region of interest (ROI) on both mMRI and μMRI T2 maps had a consistent width (~200μm). In the low-resolution mMRI profiles (Figure 5.2a), three features can be observed. First, a significant elevation of T2 can be seen in the surface tissue between the normal and the OA cartilage (0 – 0.15 depth). Second, there was no difference in T2 between the 8-weeks and 12-weeks after the surgery. Finally, for most of the deep cartilage (0.15 – 1.0 relative depth), there is little change in T2 values, regardless of whether the tissue is healthy, 8-weeks or 12-weeks after the surgery.

In the high-resolution μMRI profiles (Figure 5.2b), two specimen orientations in the magnetic field modulated the T2, where the dipolar interaction has the strongest effect on T2 at 0˚ orientation and the least effect on T2 at the 55˚ (the magic angle). At 0˚, the μMRI T2 profiles appear nearly identical to the mMRI profiles (Figure 5.2a), where the only sensitivity to the tissue degradation was on the surface of the tissue. When the

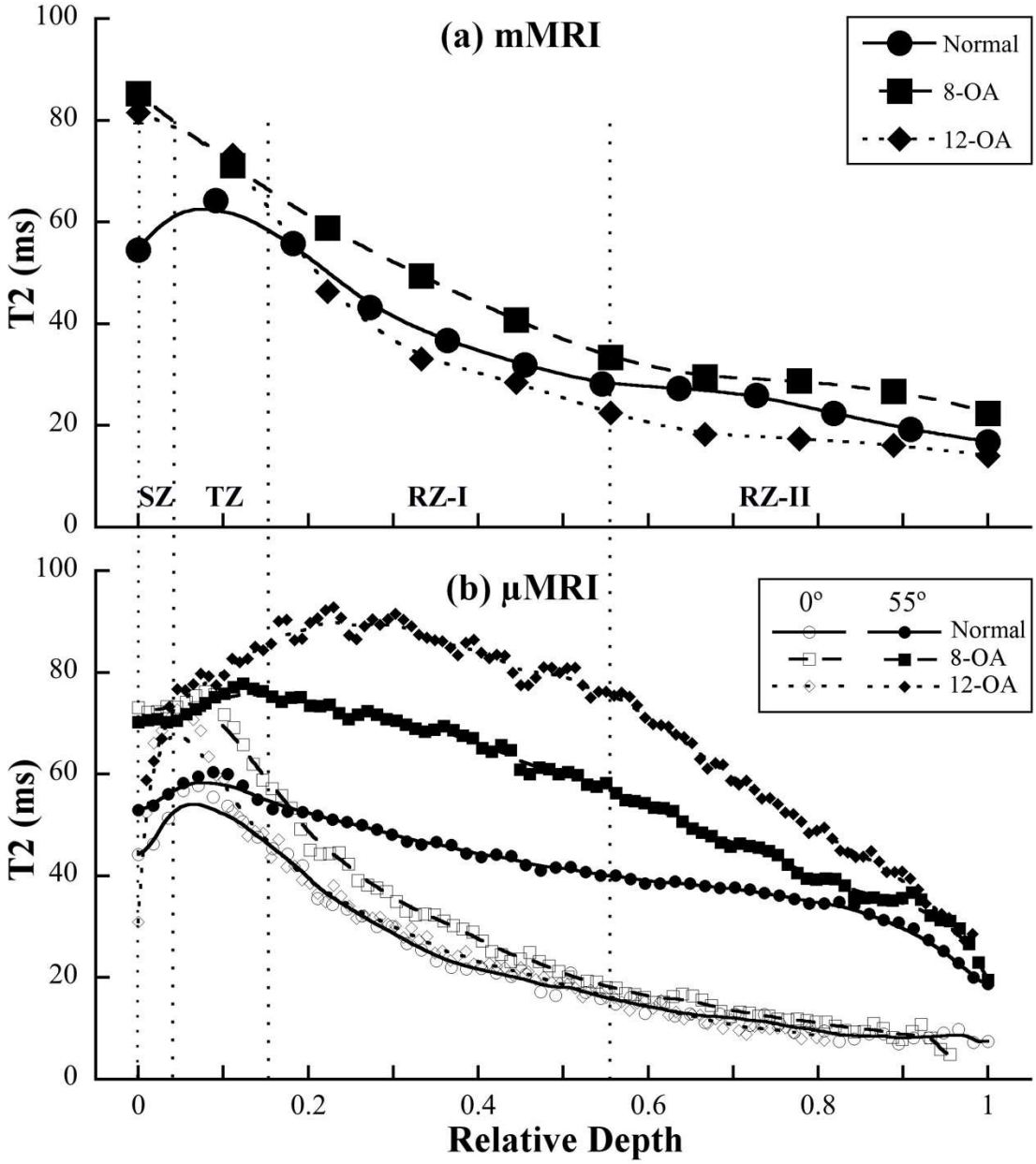

Figure 5.2 Quantitative T2 profiles of the entire cartilage from the images shown in Figure 5.1, (a) mMRI profiles at 100 µm per pixel, (b) µMRI profiles at 17.6 µm per pixel. The vertical dotted lines mark the sub-tissue zones.

specimen was oriented at 55˚ (Figure 5.2b), the progression of cartilage lesion was clearly different from the corresponding 0˚ profiles. Two additional features of these μMRI T2 55˚ profiles should be noted. First, there was a lack of major differences in the surface tissue (0 - 0.1 relative depth) between the 8OA and 12OA groups, which signals the lack of further degradation in the surface tissue from 8 weeks to 12 weeks after the ACL transection. Second, despite the lack of progression in the surface tissues between 8OA and 12OA, there were significant T2 elevations for the deep tissue (0.2 – 1.0 relative depth) between 8OA and 12OA, which indicates that the degradation in the deep cartilage happened later than the degradation in the surface cartilage.

5.2.2 Topographical and Zonal T2 Patterns among Different Lesion Groups

Quantitative T2 maps for three imaging protocols (mMRI, μMRI 0˚, μMRI 55˚) were constructed individually in all five topographical locations on the medial tibial surface (Figure 3.1). At each location, a depth-dependent profile (Figure 5.2) was obtained by averaging all the T2 profiles among the animals. These profiles were sub-divided into the four zones and the quantitative T2 values within each zone were averaged (Xia et al., 2001; Xia et al., 2012). The progressions of tissue degradation were analyzed among the five topographical sites (AMT, EMT, PMT, CMT and IMT), among the four sub-tissue zones (SZ, TZ, RZI, RZII), among the five disease groups (N, 8C, 12C, 8OA, 12OA), and among the three imaging protocols (mMRI, μMRI 0˚, μMRI 55˚).

Figure 5.3 shows the topographical T2 patterns in the superficial zone of cartilage measured by three imaging protocols at one specific topographical site. Since T2 values of healthy cartilage at different sites of the knees are known to be different (Lee et al., 2014), simply comparing an averaged T2 value would not reflect the true trend due to the

degradation. For this reason, we also calculated the topographical and zonal percentage differences of T2 between various osteoarthritic cartilage and the healthy counterpart, and used the percentages to color these topographical patterns, where darker red/blue signifies increased/decreased percentage difference with the normal (uncolored). This use of color 'hot/cold' maps highlights any trend of changes that is significant to the disease progression.

Several trends can be noted for the superficial cartilage. First, a large cluster of blue colors were noted in the anterior and exterior sites of the contralateral cartilage (AMT and EMT at 8C and 12C), where both are covered by the meniscus; and a higher cluster of red and more dark-red colors could be seen in OA cartilage (8OA and 12OA). This illustrates that T2 generally increased as the disease progressed from healthy to severe lesions. Second, although three imaging protocols (mMRI, μMRI 0˚, μMRI 55˚) measured approximately the same tissue, they showed different sensitivities towards the T2 changes. For example, both μMRI 0˚ and μMRI 55˚ at the AMT location showed lower T2 in contralateral cartilage and modest high T2 in 12OA cartilage; in contrast, mMRI showed significantly higher T2 (darker red) for both contralateral and OA cartilage at the same location (consistent with the information in Figure 5.2). Finally, each topographical location showed different trends of T2. For example, at the CMT location, the biggest increases in T2 were in the 8C cartilage (μMRI 0˚), which reduced towards later degradation. At the same time, AMT and PMT locations (which are the most anterior and posterior locations) have the opposite trends in 8C cartilage.

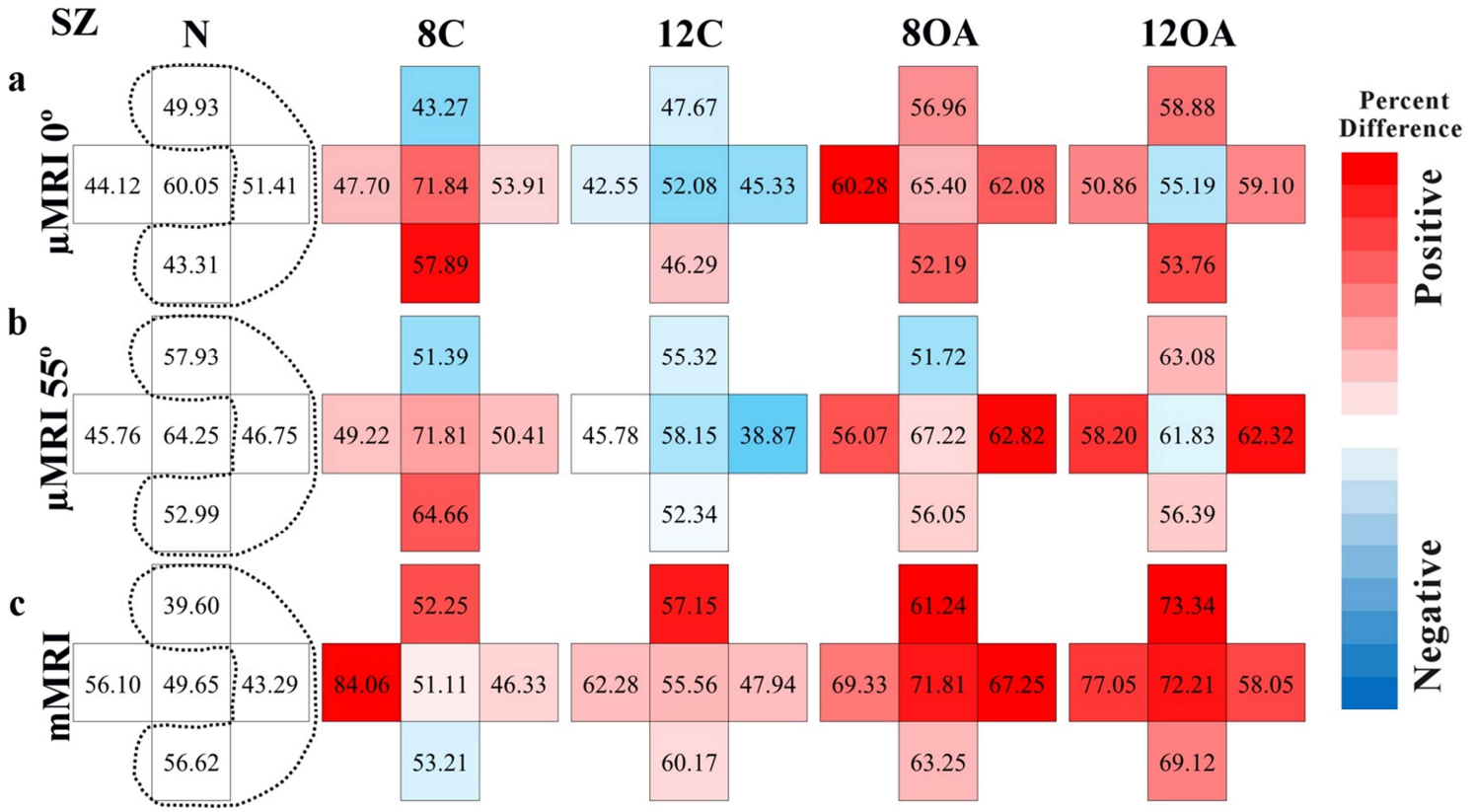

Figure 5.3 Topographical T2 maps of the superficial zone cartilage in the medial tibias from three imaging protocols: (a) μMRI at 0º, (b) μMRI at 55º, and (c) mMRI. Each T2 value is averaged among the T2 of all specimens at the same zone and same topographical location. The three blocks inside the dotted line represent the meniscus covered region, while the other two blocks represent the exposed region. The darkness of blue and red colors is based on the calculated percentage difference between each disease stage to the healthy counterpart, where darker red/blue means higher/lower percentage change than the normal, which is uncolored. The max and min % changes were ±30 % in μMRI 0º (a) and 55º (b), and ±40% in mMRI (c).

All other sub-tissue zones were studied similarly as in the SZ maps in Figure 5.3. We found that cartilage in each topographical zone degrades independently. One essential finding was that T2 changes in μMRI 0º is more evident in SZ and TZ than the deep zones, as 0º orientation showed the weakened sensitivity of T2 for the deep cartilage due to the increased influence of the dipolar interaction on water mobility. Since the intact joint in mMRI is limited to rotation (identical to the situation for a human in a whole-body MRI), T2 from the selected cartilage in mMRI is highly dependent on the orientation with respect to the magnetic field as well as the partial volume effect due to the limited resolution, which yields mMRI T2 data to have more similarity to μMRI 0˚ T2 data.

5.2.3 Zonal T2 Patterns at All Topographical Locations

Topographically distributed zonal T2 data in all five locations and by three imaging protocols were summarized as values with statistically significant differences from the healthy (N) counterparts emphasized by bold and underline, and the color hot/cold maps were scaled based on percentage differences shown in Figure 5.4. The relevant percentage differences of T2 between various osteoarthritic degradation and the healthy counterpart were presented in Table 5.1, together with statistical analysis where any significant differences were made in bold and underlined in Fig 5.4 and marked with an asterisk in Table 5.1. The averaged data was also presented as the correlated linear regression plots in Figure 5.5, which presents consistent overall conclusions, shows the effects of orientational and resolution dependency. Some of the major observations are:

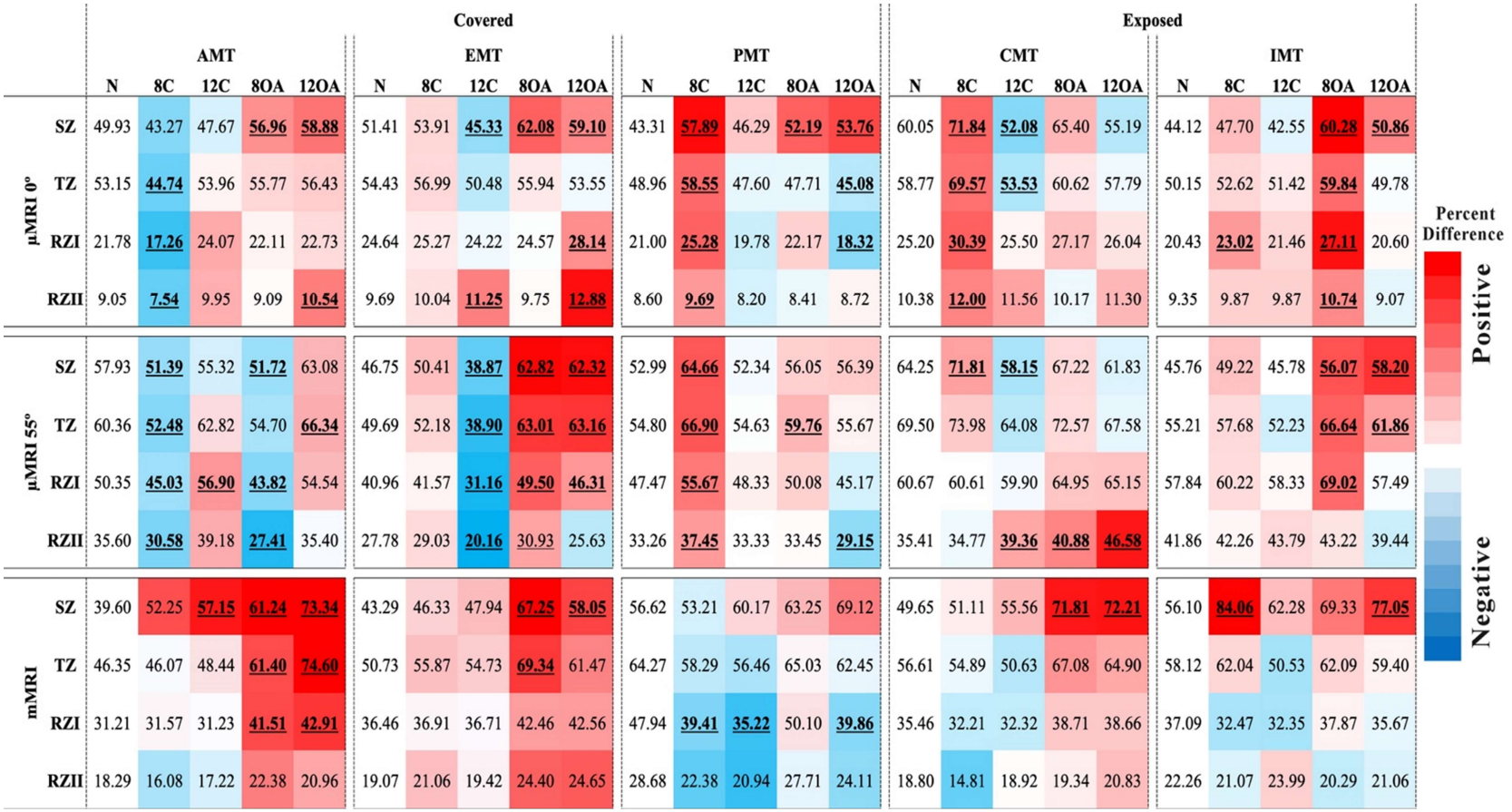

Figure 5.4 Mean T2 values of all imaging protocols, all topographical locations, starting with the normal to each of the disease stages through all histological zones (SZ, TZ, RZI and RZII). *Covered* marks the meniscus-covered region on tibial surface, (AMT, EMT, PMT); *Exposed* marks the tibial region that is not covered by the meniscus, (CMT and IMT). The mean T2 values with underlined bold font imply statistical significance in pair-wise comparison. Color coding (blue, white, red) is based on the calculated percentage difference between each disease stage to the healthy counterpart: μMRI 0º and μMRI 55˚ are -30% to +30%, mMRI is -40% to +40%. The actual percentage differences are in Table 5.

- When comparing 8C to N, the most striking observation was that in μMRI 0˚ data, T2 in AMT and PMT (which are positioned as the most anterior and posterior locations of the tibial surfaces – both are covered by the meniscus) had the opposite trends. While T2 changes in AMT statistically decreased in all zones, T2 changes in PMT statistically increased in all zones. More interestingly, despite the opposite changes between AMT and PMT, the T2 in SZ at both locations ended with statistically significant increases at the late stage of the degradation (8OA and 12OA). In addition, the T2 in CMT, which is between AMT and PMT, share the same significance as in PMT. Most mMRI T2 data in the surface tissue also showed significant increases at advanced OA.
- When comparing 12C to N, μMRI data showed more significant T2 decreases in EMT and CMT than mMRI data, especially for EMT where μMRI 55˚ T2 in all zones statistically decreased, which was followed by significant increases in 8OA and 12OA. Between (8C – N) and (12C – N), there were more decreases (more blues) in the (12C – N) comparisons.
- When comparing 8OA or 12OA to N, more significant increases in T2 could be found in all three protocols – more larger increases in the superficial tissue (SZ, TZ) and more changes in several locations (EMT, IMT), with the exception of 8OA μMRI 55˚ data in AMT, where significant T2 reductions were measured.

Summarizing Figure 5.4, the T2 in SZ had the highest increases among all zones (comparing all rows) when the disease progressed, which was evident also from the profiles in Figure 5.2. Among different imaging protocols, μMRI 55˚ had the most consistent sensitivities, reflected also by the nearly consistent slopes of the linear

regression lines in Figure 5.5. We found that T2 changes measured for each topographical site were independent of the disease progression but dependent on the zonal depth as well as the resolution and orientation of articular cartilage.

The data shown in the colored 'heat' maps as in Fig 5.4 were also analyzed using linear regression analysis, by comparing the T2 values between healthy and disease tissues, in all zones and at all topographical locations. Figure 5.5 shows the summary of this analysis effort. In these regression plots, the solid diagonal lines indicate that the T2 of the disease tissues (vertical axis) is the same as the healthy tissues (horizontal axis). Each data point represents the average T2 value, which are shape-coded, as well as color-coded. When the data points are above/below the diagonal lines, the disease tissues have a higher/lower T2 than the healthy tissue respectively. The trends of T2s for each category were fitted linearly and shown as the colored dotted lines. The major findings from this analysis support the observations from the color maps in Fig 5.4.

5.2.4 Zonal T2 OA Progression Between the Covered and Exposed Regions

To correlate with some previously published regional analysis (Alhadlaq et al., 2004; Lee et al., 2016) , we grouped all T2 data at five locations (as in Figure 5.4) into two regions, the meniscus-covered and exposed regions, and showed them in Figure 5.6. In essence, Figure 5.4 was condensed into Figure 5.6 with the same use of colormaps based on the percentage significance on the regional analysis (Table 5.2). This average from 5 locations to 2 regions strengthened the statistical power of the data analysis, at the price of losing the ability to identify the trends in individual topographical locations. The major observations in this regional analysis (Figure 5.6) agree with the topographical location analysis (Figure 5.4). Some of the highlights are:

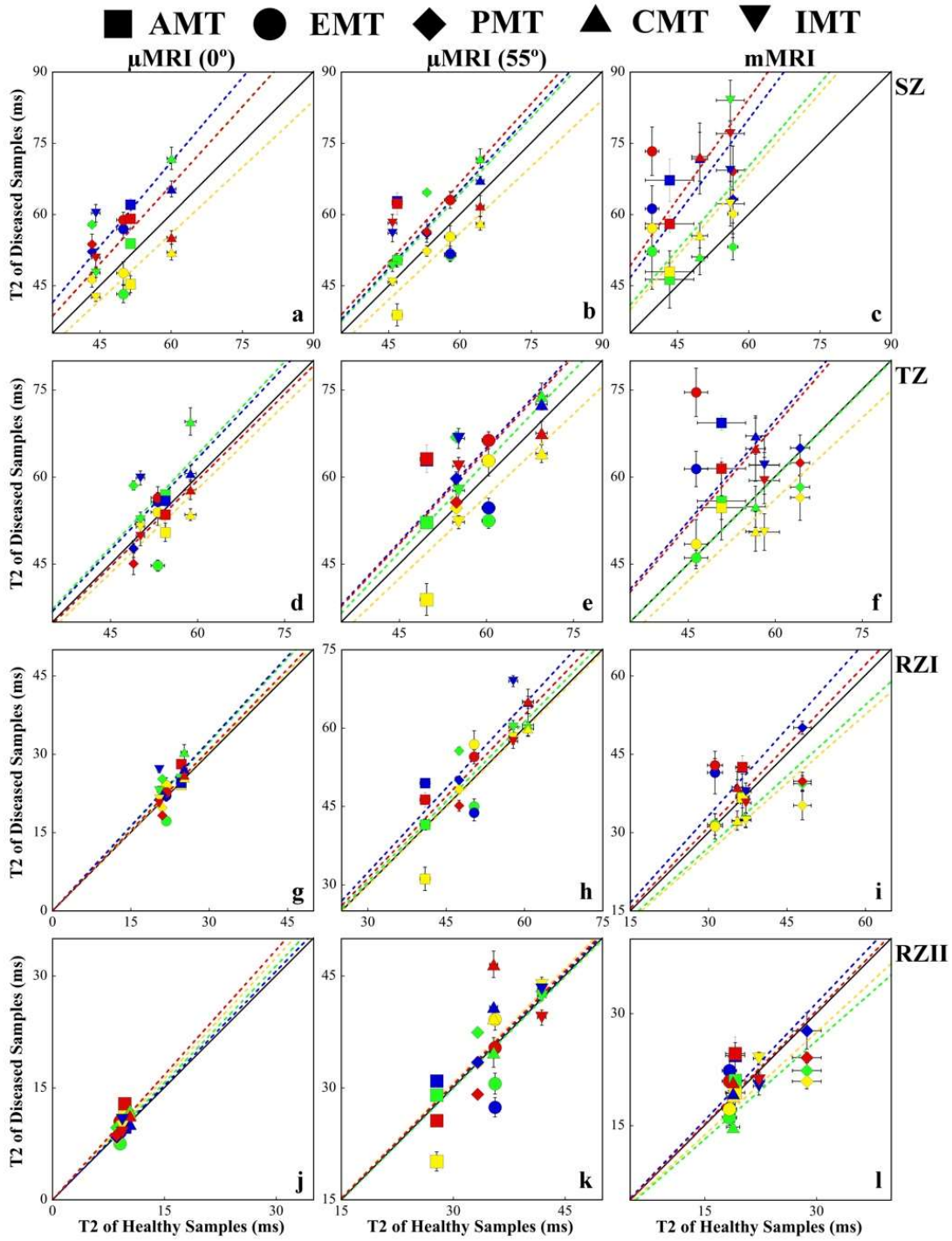

Figure 5.5 Linear regression plots of zonal averaged T2 values, comparing healthy (N, horizontal axis) and disease (vertical axis). (Green 8C, blue 8OA, yellow 12C, and red 12OA; solid square AMT, solid circle EMT, diamond PMT, up triangle CMT, down triangle IMT). For each row of data, the differences between the min T2 and max T2 are kept the same.

- The effect of location average can be seen clearly when comparing the μMRI 0˚ 8C regional data (the top two 2nd columns in Figure 5.6) with the same 8C location data (the top five 2nd columns in Figure 5.4). The opposite trends in two 8C locations (AMT and PMT) in Figure 5.4 were averaged to result in a mostly non-significant 8C covered data in Figure 5.6. At the same time, the consistent trend in both 8C CMT and IMT data in Figure 5.4 were averaged to result in more significant data across all four sub-tissue zones in the exposed region. Similar observations can be found in other disease progression and other imaging protocols, for example, the μMRI 0˚ 8OA data between the location analysis (Figure 5.4) and the regional analysis (Figure 5.6).
- When comparing two contralateral cartilages (8C and 12C in Figure 5.6), the most striking feature is mostly T2 increases (red) in 8C and mostly T2 decreases (blue) in 12C, in both μMRI 0˚ and μMRI 55˚. Interestingly, the mMRI sensitivity was very different from μMRI (due to the lack of resolution in mMRI), which had consistent results between 8C and 12C.
- When comparing two OA cartilages (8OA and 12OA in Figure 5.6), 8OA had more damage (higher T2) than 12OA, especially in the exposed regions, which solidified the observation of different trends in the zonal changes in the T2 profiles in Figure 5.1 and 5.2b.

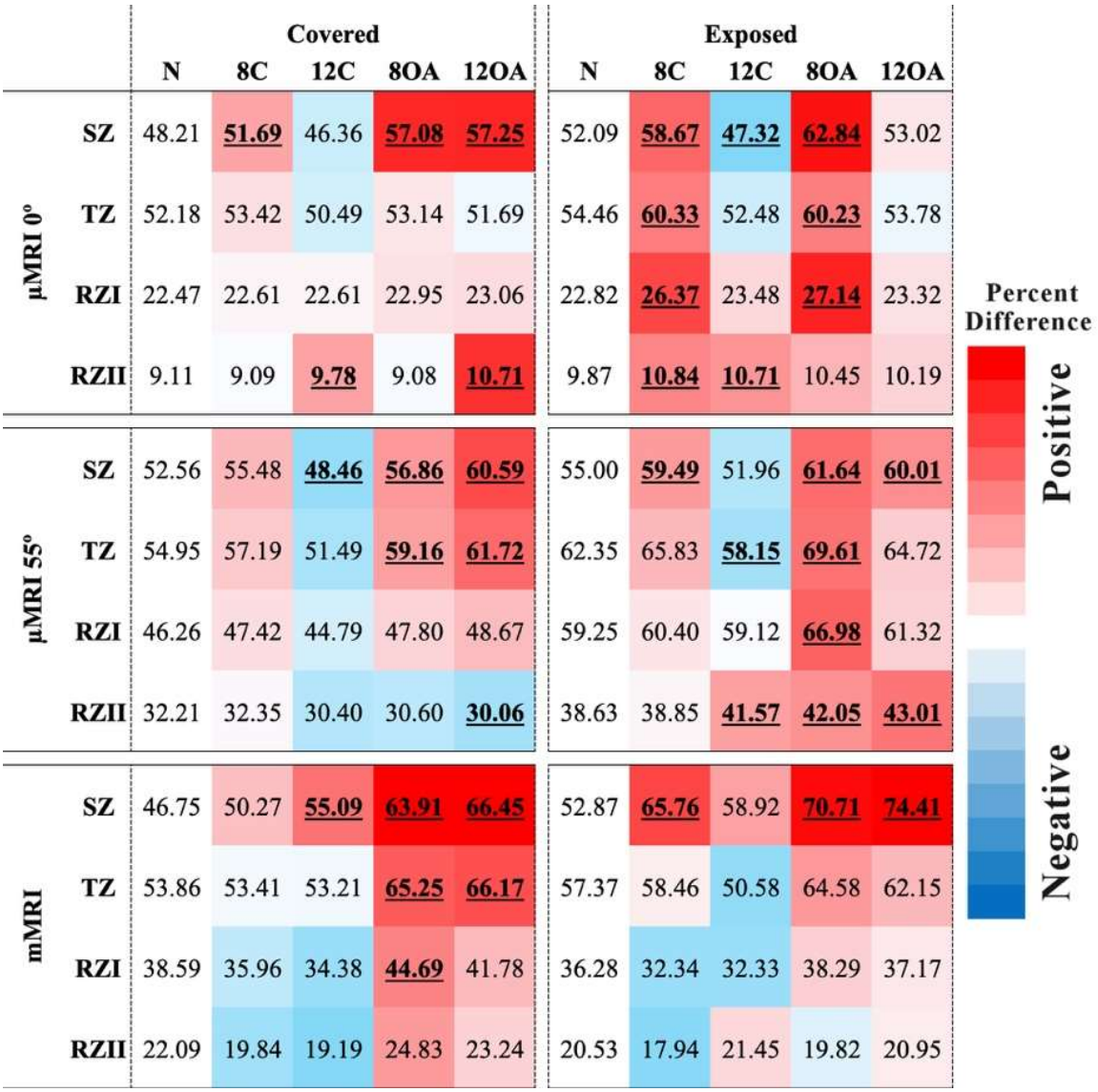

Figure 5.6 Regional average T2 values of cartilage in all imaging protocols and two grouped topographical regions, starting with the normal to each of the disease stages through all the histological zones (SZ, TZ, RZI and RZII). The mean T2 values with underlined bold font imply statistical significance in pair-wise comparison. Color coding (blue, white, red) is based on the calculated percentage difference between each disease stage to the healthy counterpart: µMRI 0º and µMRI 55˚ are -20% to +20%, mMRI is -30% to +30%. The actual percentage differences are in Table 5.2.

5.3 Discussion

To the best of our knowledge, this was the first and highest multi-resolution MRI study of five topographical patterns of T2 relaxation in tibial surface during OA progression in a well-established animal model, which is a major step above the previous studies where only two regional differences were analyzed (Xia et al., 2001; Xia et al., 2011). The use of multi-resolution enabled the correlation between the zonal characteristics at high μMRI resolution and the intact joint features at clinical MRI resolution. The degradation was initiated by the transection surgery of ACL in one knee with two waiting periods, which precisely defined the degradation period. A number of significant results were observed in the imaging study, including the overall positive correlation between the T2 values and tissue degradation, the topographical nature of tissue degradation over the tibial surface, and the depth dependent nature of morphological degradation where the surface tissue had the most changes. These findings were complex due to the multiple parameters that interplay with the data and their interpretation, including the disease detection based on imaging protocols, the disease progression as a factor of time, the disease progression per location or region, and the disease progression in depth over the zones. This study enlightened the importance and drawbacks to the study of OA progression comparing factors of overall tissue versus topographical and depth dependent.

5.3.1 Influences on Disease Detection Due to Imaging Protocols

As shown clearly in Figure 5.2, tissue degradation can be detected by the MRI T2 protocols. There are two subtle influences on the sensitivity of T2 detection to cartilage degradation. First, articular cartilage is known to have a T2 anisotropy in MRI, due to the

influences of the collagen orientation in the external magnetic field (Xia, 1998; Xia et al., 1997). When the surface normal of cartilage is parallel to B0, the dipolar interaction has the strongest attenuation effect on T2, making T2 have the shortest value and reducing its sensitivity to tissue degradation. In contrast, when the surface normal of cartilage is at 55˚ with B0 (the magic angle), the dipolar interaction is minimized, making T2 have the highest sensitivity to tissue degradation. This orientational influence on T2 sensitivity was the reason to measure T2 at two different orientations (0˚ and 55˚) in this study. In human MRI (and similarly in our mMRI), the orientation of an intact joint in the magnet is about 0˚ and the topographical ROIs selected from mMRI were predominately at 0º orientation to the magnetic field, which explains the similarity between the mMRI profiles (Figure 5.2a) and the μMRI 0˚ profiles (Figure 5.2b).

Second, for a thin layer of cartilage with a strong depth dependence across its thin thickness, the imaging resolution significantly impacts the outcome of OA detection by any imaging method. At low resolution, a large voxel contains more tissue, not only different structured cartilage but also neighboring tissues (synovial fluid, meniscus, membranes, etc.) – all having very different MRI properties than cartilage. For these canine tissues, the zonal thicknesses have been determined in several previous studies using optical imaging, as approximately SZ 80μm, TZ 120μm, and RZ 600μm (Lee & Xia, 2013; Xia et al., 2001). At the mMRI resolution of 100μm/pixel, both surface zones (SZ, TZ) were just one pixel each. At the resolution of 17.6μm/pixel in μMRI, there were about 5 pixels in SZ and 7 pixels in TZ, which were adequate to resolve these thin zones. This was the reason to quantify cartilage at two different MRI resolutions in this study, since clinical MRI typically resolves the whole thickness of human cartilage (which is

much thicker) in 3-5 pixels. Consequently, our mMRI of canine cartilage mimics almost exactly the tissue averaging scenario in clinical MRI of human cartilage with an improved unequally divided zonal division of cartilage (Badar & Xia, 2017; Xia, 2007); at the same time, our μMRI has the ability to examine cartilage degradation in a more controlled manner than what is available for clinical study. Hence, the results from our multi-resolution MRI methodology can provide an invaluable translational pathway, from bench to bedside.

5.3.2 Variations in Disease Progression

OA in humans can take multiple years to progress, which begins with increased synovial inflammation and an upregulation of degradative enzymes. The avascular and aneural natures of cartilage structure keeps the early degradation silent to the patients, who only feel the degradation at its later stages when the pain and stiffness occur. The use of animal models offers a unique advantage for the study of OA, since the degradation initiation event can be precisely defined (Pond & Nuki, 1973). The data in this project showed that cartilage at different post-surgical times had different signatures of the degradation, which had inconsistent topographical T2 patterns between contralateral and OA knees. The swelling seen in the images of Figure 5.1 clearly showed the disruption of the collagen network in both stages of OA cartilage in the presence of sufficient PG in the tissue. Between the 8-weeks and 12-weeks post-surgery, it seemed the 8-wk OA had fairly incremental changes when compared with the later timepoint (12 weeks). This observation was consistent with an earlier anatomic/morphologic report (Kahn et al., 2016) that was part of this study with similar time points, where the 8-week OA knees were found to have worse OA changes than the 12-week or even 24-week knees post-surgery. These findings

could be caused by the overcompensating damages (e.g., swelling) in the 8wk OA joint as well as the 8wk C joint, which recovered partially at the later time points.

Coming back to the biology of cartilage degradation, the onset of OA causes the tissue to have more water and less PG. However, any change to a complex tissue would have consequences. More water and less PG also change the local orientation and concentration of the collagen fibers, both of which strongly influence the quantitative measurement of T2. As shown clearly in the magic angle effect of cartilage in MRI, the fibril orientation can reduce or increase the T2 values in cartilage tissue, depending upon the precise modification to the local fibril matrix (Lee & Xia, 2013; Xia et al., 2001). There are therefore multiple factors that can vary the quantitative measurement, towards opposite directions, in a site-specific, resolution-dependent and orientation dependent manner. Further studies are needed to verify the biological and biochemical origins of this observation.

5.3.3 Variations in Zonal Disease Progression

T2 in the surface cartilage has showed high sensitivity towards the disease progression. As evident from Figure 5.2 and other parts of the results in this report, the top ¾ of cartilage had a rapid degradation progression during the first 8 weeks post-surgery (Figure 5.2b), consistent with the finding in previous studies (Lee et al., 2014). Between 8-weeks and 12-weeks post-surgery, most of additional degradation occurs in the middle tissue (0.15 – 0.8 relative depth). Given the fact that the early lesions in human OA are known to localize near/around the surface of the tissue (Hwang et al., 1992; Pritzker et al., 2006; Squires et al., 2003), the use of high resolution in imaging will increase the detection sensitivity and differentiation of different tissue degradation. With

the improvement of clinical MRI technology, resolving cartilage thickness in more pixels could become possible for human MRI. It should be noted that since the imaging pixel size in MRI has a consistent size while the sub-tissue zones in cartilage have variable thickness, it is the thinnest zone in cartilage that places the requirement for the minimum resolution that is adequate to resolve the zones in MRI.

5.3.4 Variations in Topographical Disease Progression

This study demonstrates clearly that the tissue degradation is not uniform across the joint surface; instead, different trends of degradation occur at different locations over a joint surface. This location variability is compounded with the zonal variability, making the patterns of OA degradation in the tibial cartilage a time-dependent three-dimensional matrix. As evident from Figure 5.4 and Table 5.1 in this report, the degradation between AMT and PMT had opposite trends by both μMRI 0˚ and 55˚ protocols. While T2 showed significant decreases in AMT, the trends in PMT (and CMT) were the opposite – both locations had consistent and statistically significant increases over all zones. This is likely caused by the differences in the local loading pattern on the tibial surface.

Two different topographical analyses were used in this project, the location analysis where each of the five independent sites on the medial tibial surface were studied individually, and the regional analysis where the medial tibial surface was divided into two regions, covered by the meniscus, and not covered by the meniscus. The regional analysis certainly benefits from a stronger statistical power in data analysis, which was used in several of the previous publications (Alhadlaq et al., 2004; Lee et al., 2015; Lee et al., 2016). The price to pay for a regional analysis is that T2 trends are averaged over a much larger area on the tibial surface, where different locations within one area are

known to progress differently during the tissue degradation. Previous studies have also shown that, after OA progression, the meniscus-covered area changes from the defined healthy meniscal and exposed regions on the tibia (Appleyard et al., 2003; Kahn et al., 2016), causing the grouping of sites to move from covered to exposed regions, affecting the interpretation of disease progression in covered and exposed regions. This project kept the same group from healthy to each disease stage for consistency whereas the effect due to OA may change the assignment of the site from one group to another. This project clearly demonstrates the beneficial value from a more detailed location analysis, and perhaps a dynamic grouping from locations to regions. The results from this project provide a background knowledge required for future study of localized knee OA.

5.3.5 Conclusion

The influences of several experimental parameters and methods to the detection of early OA in cartilage by the ACL transection have been studied in this project. We observed the positive correlation between the T2 values and tissue degradation, the depth dependence of tissue degradation where the surface tissue had the most changes, and the location-dependence of tissue degradation over the tibial surface. To the best of our knowledge, the μMRI results are the first quantitative and multi-resolution characterization of cartilage at five independent locations over the medial tibial surface in an animal model of OA. We showed that in the early degradation of OA, the changes in cartilage properties are influenced strongly by the ability to image small regions topographically and small tissue depths zonally. A topographical view with fine zonal resolution is crucial for diagnostic detection of early OA by any imaging tool. In addition, the contralateral cartilage can have different degradation patterns than seen in OA

cartilage. The use of MRI imaging protocols can also influence the data interpretation. The use of dual resolutions in MRI in this project provides a scalable translational pathway between bench and bedside.

Table 5.1 Quantitative T2 percent differences of µMRI 0º (a), µMRI 55º (b) and mMRI (c) of the individual topographical locations, which were used to color Fig 5.4. The table starts with the differences of each disease stage (8C, 12C, 8OA and 12OA) from the normal (N) followed by the disease group comparison, through all of the histological zones (SZ, TZ, RZI and RZII). AMT, EMT, PMT mark the three meniscus-covered locations on tibial surface, while CMT and IMT mark the two tibial locations that is not covered by the meniscus. Any number marked with * signifies the statistical significance ($p<0.05$) within the pairwise comparison.

(a)

a	site	Zone	N v. 8C	N v. 12C	N v. 8OA	N v. 12OA	8C v. 8OA	12C v.12OA	8C v. 12C	8OA v.12OA
µMRI 0º	AMT	SZ	-14.28	-4.63	13.17*	16.46*	27.32*	21.05*	9.67	3.31
		TZ	-17.18*	1.52	4.81	5.99	21.95*	4.48	18.69*	1.18
		RZI	-23.15*	10.01	1.51	4.27	24.64*	-5.75	32.97*	2.76
		RZII	-18.12*	9.47	0.52	15.28*	18.63*	5.83	27.47*	14.76
	EMT	SZ	4.76	-12.55*	18.82*	13.93*	14.09*	26.37*	-17.28*	-4.92
		TZ	4.59	-7.53	2.73	-1.64	-1.85	5.89	-12.11*	-4.38
		RZI	2.55	-1.70	-0.25	13.28*	-2.80	14.97*	-4.25	13.53*
		RZII	3.53	14.95*	0.61	28.30*	-2.93	13.49*	11.43*	27.71*
	PMT	SZ	28.82*	6.67	18.60*	21.53*	-10.36*	14.92*	-22.27*	2.96
		TZ	17.83*	-2.82	-2.59	-8.25*	-20.40*	-5.44	-20.63*	-5.67
		RZI	18.51*	-5.99	5.42	-13.62*	-13.12*	-7.64	-24.43*	-19.01*
		RZII	11.94*	-4.79	-2.26	1.34	-14.20*	6.12	-16.71*	3.60
	CMT	SZ	17.88*	-14.21*	8.52	-8.43	-9.39	5.79	-31.89*	-16.93*
		TZ	16.83*	-9.33*	3.11	-1.68	-13.74*	7.66	-26.06*	-4.79
		RZI	18.68*	1.19	7.52	3.29	-11.20	2.10	-17.50*	-4.24
		RZII	14.44*	10.71	-2.05	8.49	-16.48*	-2.23	-3.74	10.53
	IMT	SZ	7.79	-3.63	30.95*	14.18*	23.30*	17.79*	-11.41	-16.95*
		TZ	4.82	2.51	17.62*	-0.74	12.83*	-3.26	-2.30	-18.36*
		RZI	11.93*	4.93	28.11*	0.81	16.31*	-4.12	-7.02	-27.32*
		RZII	5.43	5.35	14.80*	-3.00	8.36	-8.35	-0.08	-16.76*

(b)

b	site	Zone	N v. 8C	N v. 12C	N v. 8OA	N v. 12OA	8C v. 8OA	12C v.12OA	8C v. 12C	8OA v.12OA
µMRI 55º	AMT	SZ	-11.96*	-4.62	-11.33*	8.50	0.64	13.11*	7.36	19.78*
		TZ	-13.97*	3.99	-9.84	9.43*	4.14	5.45	17.93*	19.23*
		RZI	-11.17*	12.21*	-13.88*	7.99	-2.71	-4.23	23.30*	21.80*
		RZII	-15.17*	9.58	-25.98*	-0.57	-10.92	-10.14	24.66*	25.42*
	EMT	SZ	7.53	-18.41*	29.34*	28.55*	21.93*	46.35*	-25.85*	-0.81
		TZ	4.89	-24.36*	23.63*	23.87*	18.80*	47.54*	-29.16*	0.24
		RZI	1.48	-27.19*	18.87*	12.25*	17.41*	39.11*	-28.63*	-6.66
		RZII	4.40	-31.78*	10.73*	-8.03	6.34	23.90*	-36.05*	-18.72*
	PMT	SZ	19.83*	-1.25	5.60	6.21	-14.27*	7.46	-21.06*	0.62
		TZ	19.88*	-0.32	8.65*	1.57	-11.28*	1.89	-20.20*	-7.09
		RZI	15.90*	1.79	5.35	-4.96	-10.58*	-6.75	-14.12*	-10.30*
		RZII	11.85*	0.21	0.55	-13.17*	-11.30*	-13.38*	-11.65*	-13.72*
	CMT	SZ	11.12*	-9.97*	4.52	-3.84	-6.61	6.14	-21.03*	-8.35
		TZ	6.25	-8.12	4.33	-2.79	-1.92	5.33	-14.35*	-7.12
		RZI	-0.10	-1.28	6.81	7.12	6.91	8.40	-1.18	0.32
		RZII	-1.82	10.56*	14.36*	27.25*	16.17*	16.80*	12.38	13.02*
	IMT	SZ	7.27	0.04	20.24*	23.92*	13.02*	23.89*	-7.23	3.73
		TZ	4.38	-5.55	18.77*	11.37*	14.42*	16.89*	-9.92	-7.43
		RZI	4.04	0.85	17.63*	-0.60	13.62*	-1.45	-3.18	-18.23*
		RZII	0.94	4.50	3.25	-5.96	2.25	-10.45*	3.56	-9.15*

(c)

c	site	Zone	N v. 8C	N v. 12C	N v. 8OA	N v. 12OA	8C v. 8OA	12C v.12OA	8C v. 12C	8OA v.12OA
mMRI	AMT	SZ	27.54	36.29*	42.93*	59.76*	15.86	24.81	8.97	17.98
		TZ	-0.60	4.41	27.94*	46.72*	28.52*	42.53*	5.01	19.42
		RZI	1.12	0.04	28.31*	31.56*	27.21	31.52*	-1.08	3.33
		RZII	-12.88	-6.01	20.10	13.57	32.77*	19.54	6.88	-6.58
	EMT	SZ	6.78	10.20	43.35*	29.13*	36.84*	19.07	3.42	-14.68
		TZ	9.64	7.60	31.00*	19.15	21.51	11.60	-2.05	-12.02
		RZI	1.22	0.66	15.20	15.42	13.98	14.76	-0.56	0.22
		RZII	9.90	1.81	24.49	25.49	14.68	23.71	-8.09	1.02
	PMT	SZ	-6.21	6.09	11.07	19.89	17.25	13.84	12.29	8.87
		TZ	-9.77	-12.93	1.17	-2.88	10.94	10.06	-3.18	-4.05
		RZI	-19.55*	-30.60*	4.39	-18.41*	23.89*	12.36	-11.22	-22.76*
		RZII	-24.68	-31.22	-3.45	-17.34	21.28	14.07	-6.66	-13.91
	CMT	SZ	2.91	11.24	36.49*	37.03*	33.67*	26.06*	8.34	0.56
		TZ	-3.10	-11.15	16.92	13.64	19.99	24.70	-8.06	-3.30
		RZI	-9.61	-9.27	8.77	8.64	18.33	17.87	0.34	-0.13
		RZII	-23.78	0.62	2.81	10.24	26.55	9.62	24.39	7.44
	IMT	SZ	39.90*	10.44	21.10	31.47*	-19.20	21.20	-29.76*	10.54
		TZ	6.52	-13.97	6.60	2.18	0.08	16.14	-20.45	-4.43
		RZI	-13.27	-13.66	2.08	-3.89	15.34	9.78	-0.39	-5.97
		RZII	-5.52	7.46	-8.85	-5.54	-3.75	-12.98	12.96	3.72

Table 5.2 Quantitative T2 percent differences of all imaging protocols of two topographical regions (Covered and Exposed), which were pooled from the five location-data in Table 5.1. The values in this table were used to color Fig 5.5. Any number marked with * signifies the statistical significance ($p<0.05$) within the pairwise comparison.

	site	Zone	N v. 8C	N v. 12C	N v. 8OA	N v. 12OA	8C v. 8OA	12C v.12OA	8C v. 12C	8OA v.12OA
µMRI 0°	**Covered**	**SZ**	6.96*	-3.92	16.84*	17.13*	9.91*	21.02*	-10.88*	0.30
		TZ	2.36	-3.30	1.82	-0.95	-0.53	2.35	-5.65	-2.77
		RZI	0.59	0.61	2.11	2.60	1.52	1.99	0.02	0.49
		RZII	-0.23	7.09*	-0.33	16.16*	-0.10	9.10*	7.31*	16.49*
	Exposed	**SZ**	11.89*	-9.60*	18.71*	1.78	6.85	11.38*	-21.43*	-16.94*
		TZ	10.22*	-3.71	10.07*	-1.25	-0.16	2.46	-13.92*	-11.31*
		RZI	14.47*	2.88	17.32*	2.18	2.87	-0.70	-11.60*	-15.15*
		RZII	9.39*	8.22*	5.77	3.21	-3.63	-5.01	-1.18	-2.57
µMRI 55°	**Covered**	**SZ**	5.42	-8.12*	7.87*	14.21*	2.45	22.26*	-13.52*	6.35
		TZ	3.99	-6.51	7.37*	11.60*	3.38	18.08*	-10.49*	4.25
		RZI	2.48	-3.24	3.27	5.08	0.79	8.31*	-5.71	1.81
		RZII	0.43	-5.78	-5.15	-6.91*	-5.58	-1.13	-6.21	-1.76
	Exposed	**SZ**	7.83*	-5.69	11.38*	8.71*	3.56	14.38*	-13.50*	-2.68
		TZ	5.43	-6.97*	11.00*	3.73	5.58	10.70*	-12.39*	-7.27
		RZI	1.91	-0.23	12.25*	3.43	10.34*	3.66	-2.14	-8.83*
		RZII	0.56	7.33*	8.47*	10.72*	7.91*	3.40	6.76	2.25
mMRI	**Covered**	**SZ**	7.24	16.37*	31.01*	34.80*	23.91*	18.70*	9.16	3.90
		TZ	-0.84	-1.20	19.14*	20.52*	19.97*	21.71*	-0.37	1.40
		RZI	-7.06	-11.53	14.64*	7.92	21.64*	19.41*	-4.48	-6.74
		RZII	-10.72	-14.02	11.68	5.07	22.34	19.05	-3.30	-6.63
	Exposed	**SZ**	21.72*	10.82	28.87*	33.84*	7.26	23.23*	-10.96	5.10
		TZ	1.89	-12.57	11.83	8.01	9.95	20.52*	-14.46	-3.84
		RZI	-11.46	-11.49	5.40	2.43	16.84*	13.91	-0.03	-2.98
		RZII	-13.50	4.39	-3.55	2.00	9.95	-2.39	17.86	5.55

CHAPTER SIX

THE INTERFACE REGION BETWEEN ARTICULAR CARTILAGE AND BONE BY μMRI AND PLM AT MICROSCOPIC RESOLUTIONS

6.1 Introduction

Quantitative T2 in magnetic resonance imaging (MRI) has been used extensively to measure the dynamic motion of water molecules which can be influenced by the structural properties of the collagen matrix in articular cartilage (Xia, Moody, & Alhadlaq, 2002). When imaged using standard spin-echo (SE) or gradient-echo (GE) based MRI sequences, T2 in articular cartilage has strong depth and orientational dependencies (the magic angle effect), which makes the accurate measurement of tissue thickness difficult (Shao et al., 2017; Wang & Xia, 2012). In addition, the finite echo time (from several to 10s of milliseconds) in SE- and GE-based imaging sequences leads to a very weak signal for the deep portion of articular cartilage, making the quantification of T2 in the deep RZ and ZCC impossible (Wang et al., 2018). Having a much shorter echo time (as short as a fraction of a millisecond), ultra-short echo time (UTE) imaging sequences have the potential to visualize ZCC (Bae et al., 2010; Du et al., 2013; Nykänen et al., 2020; Shao et al., 2016). In clinical MRI, study of the ZCC is mainly limited to qualitative comparisons between long and short echo-time images due to the resolution limitation and orientational limitation (Bae et al., 2014). In μMRI, both SE and UTE sequences have been used to study the deep cartilage and ZCC but without complementary correlation at optical resolution (Mahar et al., 2018).

In this study, we aimed to quantify T2 in both non-calcified and calcified cartilage, from the articular surface to the beginning of the subchondral bone plate, using both SE/GE and UTE MRI sequences, and correlate the quantitative T2 anisotropy results from microscopic MRI (μMRI) with the quantitative optical birefringence calibration from polarized light microscopy (PLM). We paid attention to the interface region between the non-calcified cartilage and the subchondral bone plate, which can be damaged in post-traumatic injuries, for better understanding of future studies of OA progressing in the calcified cartilage.

6.2 Results

6.2.1 Intensity Maps of Cartilage-Bone Plug by Three Different Imaging Sequences

Figure 6.1 shows six proton intensity maps of a cartilage-bone specimen by three different imaging sequences, at both 0º (Figure 6.1.a-.c) and 55˚ orientations (Figure 6.1. d-. f). At the 0˚ orientation where the dipolar interaction is the strongest, the images by GE (Figure 6.1.a) and Mprep.SE (Figure 6.1.b) clearly show the depth-dependent intensity variations of cartilage, which agree with the well-recognized fibril orientational structure in the non-calcified cartilage. In contrast, the intensity image by UTE (Figure 6.1.c) shows a uniform appearance for nearly the entire depth of cartilage, well into the deep cartilage and calcified cartilage. At the 55˚ orientation to B_0 (the magic angle), cartilage by all three imaging sequences shows a uniform appearance, similar to the UTE image at 0˚. The large (white) and small (colors) ROIs represent the overall and individual zones selected for quantitative analysis, respectively.

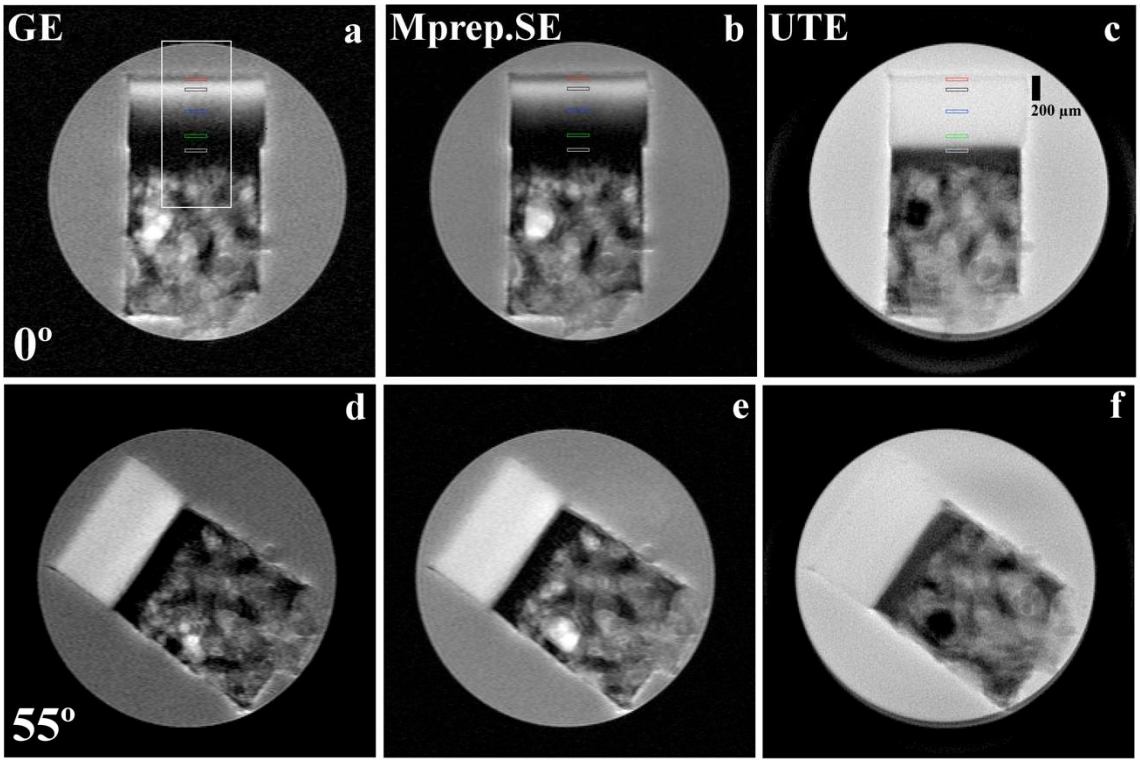

Figure 6.1 T2-weighted intensity maps using a Gradient Echo (GE), magnetized prepared Spin Echo (Mprep.SE), and Ultra-short Echo (UTE) sequence of cartilage bone plugs at 0º (a, b, and c) and 55º (d, e, and f) respectively (the direction of the B0 is vertically up in the figure). The white ROI box represents the region of interest for analysis. The smaller ROIs within represent the zonal locations where red, black, blue, green, and white ROIs represent SZ, TZ, RZ1, RZ2, and ZCC respectively. All images are displayed using the same max and min intensity limits.

6.2.2 Single Exponential Fits of ROIs In Individual Zones of Cartilage-Bone Plugs

At the 0º orientation when the normal axis of the surface of the tissue block is parallel with B_0, GE and Mprep.SE images (Figures 6.2.a and 2.b), T2 can be quantified in SZ, TZ, and RZ1, where the signal decays can be fit by an exponential function. However, GE and Mprep.SE images (Figures 6.2.a and 2.b) cannot quantify T2 in the deepest portion of non-calcified cartilage (RZ2) and cartilage-bone interface (ZCC), due

to the long TEs and the strong influence of the dipolar interaction on T2. In contrast, the UTE sequence (Figure 6.2.c) cannot quantify T2 in SZ, TZ and RZ1 due to insufficient signal attenuation at these ultra-short TEs and, hence, lead to large errors, but can reliably quantify T2 in the RZ2 and ZCC due to the adequate decay, because of the strong influence of the dipolar interaction.

At the magic angle (~54.7º to B_0), GE and Mprep.SE (Figures 6.3.a and 3.b) sequences can quantify higher T2 values due to the minimization of the dipolar interaction in all the non-calcified cartilage zones (SZ, TZ, RZ1 and RZ2), which give the tissue its homogenous appearance. Table 6.1 and Table 6.2 summarize the calculated T2 relaxation times and the fitting errors based on the single exponential fit of each zone's individual ROI as shown in the images and profiles of Figures 6.2 and 6.3 respectively. The error and goodness of fit (R^2) in the tables describe the type of fitting and are determined by KaleidaGraph software (Reading, PA). Single exponential fittings of T2 in all four non-calcified zones are significantly accurate (Table 6.2). In contrast, the UTE sequence (Figure 6.3.c), with its very short echo times, cannot measure a reliable T2 as the fit lies at the shortest part of the exponential fit whereas T2 of the non-calcified cartilage at the magic angle has long values. T2 quantification by UTE was reliable only in the calcified region of cartilage due to its short values (Table 6.1).

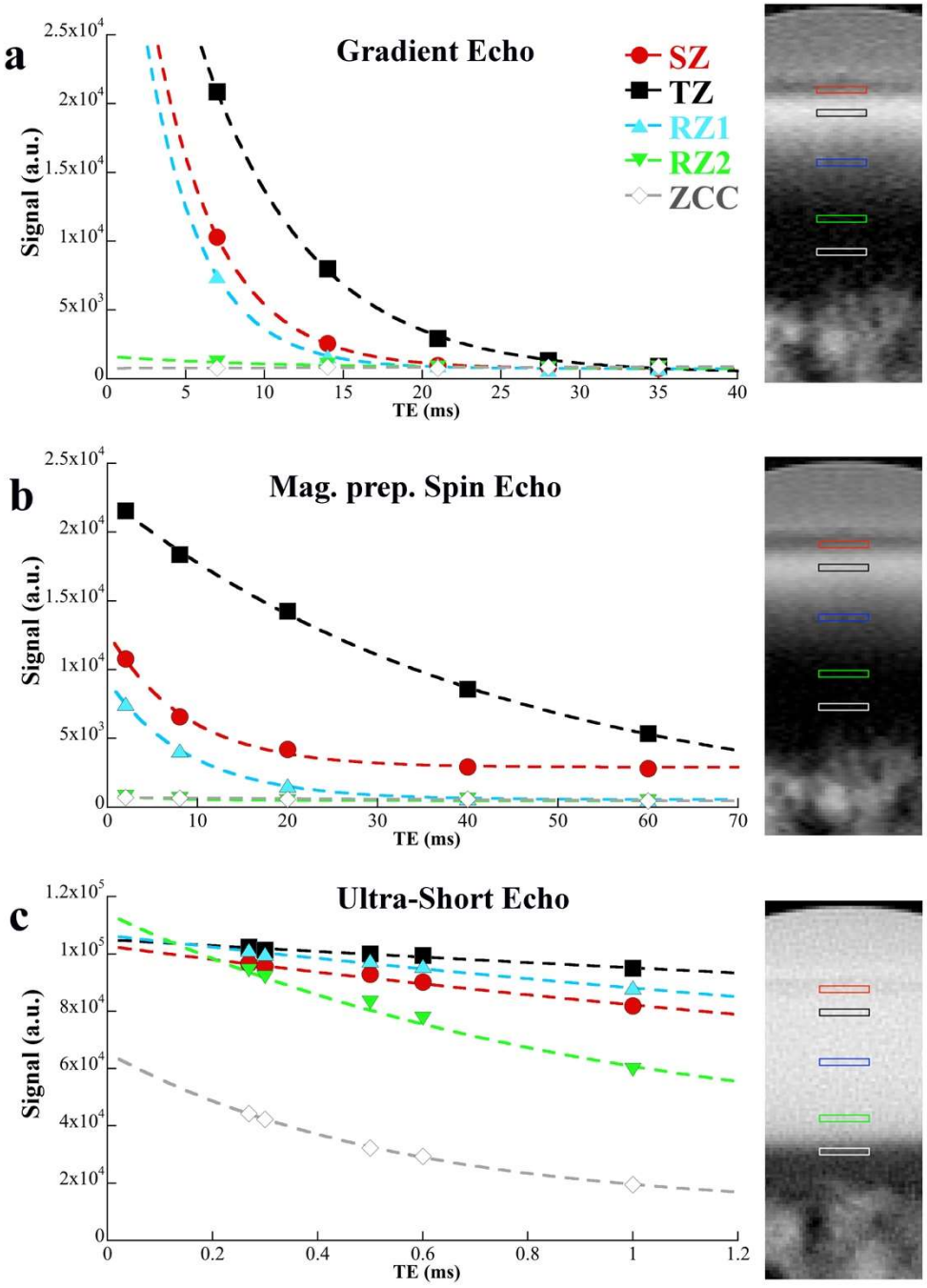

Figure 6.2 The signal attenuations in the five individual zonal locations (SZ, TZ, RZ1, RZ2 and ZCC) of a cartilage-bone specimen at 0º orientation with the magnetic field were fitted with a single exponential. The specimen by the GE and Mprep.SE sequences showed the distinct anisotropic properties of the tissue where the RZ and ZCC had the overall low signal intensities. The same specimen by the UTE sequence showed little change in attenuation within the SZ, TZ and RZ1 ROIs, but measurable decays in RZ2 and ZCC.

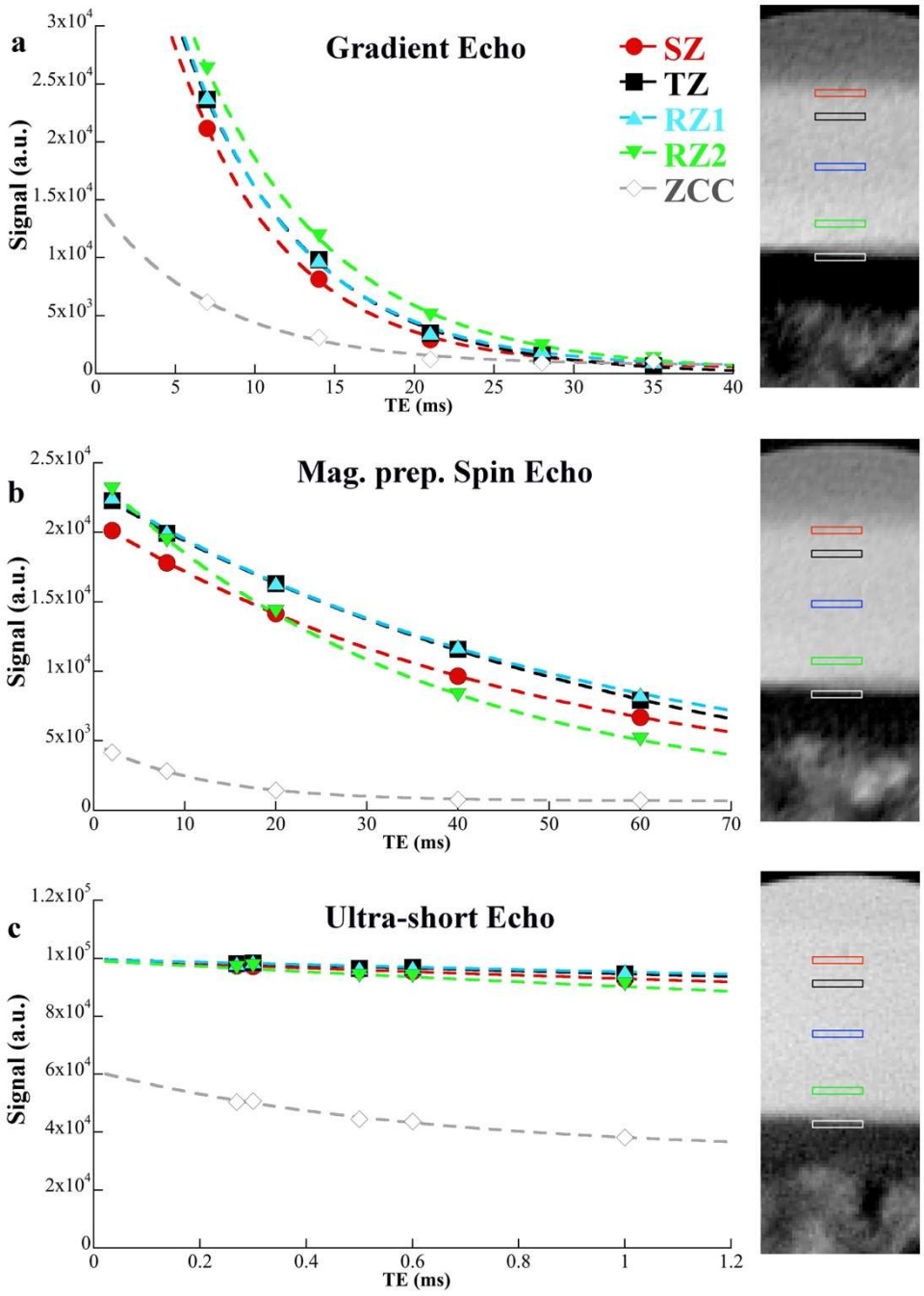

Figure 6.3 The signal attenuations in the five individual zonal locations (SZ, TZ, RZ1, RZ2 and ZCC) of a cartilage-bone specimen at 55º orientation with the magnetic field were fitted with a single exponential. The specimen by the GE and Mprep.SE sequences showed the uniform isotropic properties of the tissue. The same specimen by the UTE sequence showed little change in attenuation within the SZ, TZ, RZ1 and RZ2 ROIs, but measurable decays in ZCC.

Table 6.1 T2 and T2* values using an exponential fit of one cartilage-bone specimen at 0º orientation with respect to B0. *** represents errors greater than mean ZCC of GE and SE T2* values. Data that is underlined represents T2 values that have large errors.

0º	Gradient Echo			Mprep.SE			UTE		
Zone	**T2***	**Err**	**R^2**	**T2**	**Err**	**R^2**	**T2***	**Err**	**R^2**
SZ	4.184	0.138	1.000	8.696	1.059	0.996	2.849	6.867	0.983
TZ	6.944	0.238	1.000	43.860	5.386	0.999	6.494	39.594	0.978
RZ1	3.546	0.249	1.000	9.174	0.213	1.000	3.425	11.599	0.975
RZ2	9.709	4.430	0.981	6.536	5.425	0.837	0.917	0.707	0.984
ZCC	442.478	***	0.564	961.538	***	0.907	0.543	0.050	0.999

Table 6.2 T2 and T2* values using an exponential fit of one cartilage-bone specimen at 55º (magic angle) orientation with respect to B0. Data that is underlined represents T2 values that have large errors.

55º	Gradient Echo			Mprep.SE			UTE		
Zone	**T2***	**Err**	**R^2**	**T2**	**Err**	**R^2**	**T2***	**Err**	**R^2**
SZ	6.944	0.277	1.000	48.309	1.221	1.000	9.174	18.433	0.999
TZ	7.752	0.389	0.999	64.103	6.246	1.000	11.198	185.592	0.949
RZ1	7.407	0.469	0.999	53.476	5.090	1.000	12.920	417.309	0.868
RZ2	8.547	0.272	1.000	35.461	1.911	1.000	5.236	51.260	0.912
ZCC	7.463	1.754	0.988	11.933	0.483	1.000	0.606	0.281	0.987

6.2.3 Qualitative and Quantitative Maps of Non-Calcified and Calcified Cartilage-Bone Specimen

Four optical images from two adjacent, six-micron thin cartilage-bone slices from the same tissue specimen are shown in Figures 6.4.a to 4.d. Figure 6.4.a is a slice stained with H&E, which differentiates the non-calcified cartilage, calcified cartilage, and SBP based on the dye binding properties (Deng et al., 2016; Li et al., 2013). Figure 6.4.b is a regular optical image of the unstained tissue slice. Figures 6.4.c and 4.d are a pair of the quantitative PLM images using the same unstained slice as in Figure 6.4.b, the retardation image in grayscale (where black is minimum and white is maximum in the unit of nanometers) and the angle image in color (where 0˚ to 90˚ is represented by blue, white, and red colors). In the quantitative retardation image (Figure 6.4.c), the SZ and RZ have high retardation values, while a minimum retardation occurs as dark grey at the central location of TZ. In the quantitative angle image (Figure 6.4.d), the blue in SZ and red in RZ represent the SZ and RZ, respectively, which are 90˚ to each other. It should be noted that the dense red color, representing the 90º orientation (in parallel with the normal axis to the articular surface), extends further into the calcified cartilage, which is critical in the understanding of the anisotropy measured in the calcified cartilage by μMRI.

Figures 6.4.e-h compares the μMRI proton intensity maps and the quantitative T2 maps of the same cartilage-bone specimen where the tissue sections were optically imaged in Figures 6.4.a-d. Each μMRI image has a red arrow that marks the same cartilage-bone interface as identified by the optical images at a much higher optical resolution (Figure 6.4.a). The Mprep.SE intensity map (Figure 6.4.e) shows the heterogeneity in the cartilage appearance at the 0º orientation (the strongest dipolar

interaction), while the darkest region is at about the tidemark (red arrow). In the UTE intensity image, at the shortest TE of 235 μs (Figure 6.4.f), cartilage has a homogenous appearance with measurable intensity, well below the tide mark (red arrow). The quantitative T2 map, using Mprep.SE sequence (Figure 6.4.g), has the calculation noises in much of the deep RZ (RZ2) and in the ZCC, due to the strong dipolar interaction in these regions. The quantitative T2 map, using UTE sequence (Figure 6.4.h), is scaled from 0 to 5ms, where the white (bright) regions in the upper cartilage have inaccurately calculated T2 values due to the lack of sufficient signal attenuation, whereas the dark region around the tidemark (red arrow) has consistent T2 values (under 5ms).

The region of the deep non-calcified cartilage and ZCC in the optical images shown in Figure 6.4 were enlarged at a higher magnification (×20) and shown in Figure 6.5. From the H&E-stained optical image (Figure 6.5.a), the thin layer of the calcified cartilage can be measured at about 100-200 μm in thickness (between the white arrows). The H&E-stained image shows clearly the two interfaces, the tide mark that separates the non-calcified cartilage and the ZCC, and the second interface between ZCC and the underlying SBP. The line of the tide mark is approximately straight but the interface between ZCC and SBP has significant waving. Figures 6.5.b-d shows the same tissue regions in qualitative intensity image, quantitative retardation map and quantitative azimuth map, respectively. Even though the H&E image shows a segmented discontinuity among the non-calcified cartilage, ZCC, and SBP, quantitative PLM images shows the structural and orientational continuity of the collagen fibers from the non-calcified RZ cartilage to the mineralized and calcified cartilage, and further into the subchondral bone.

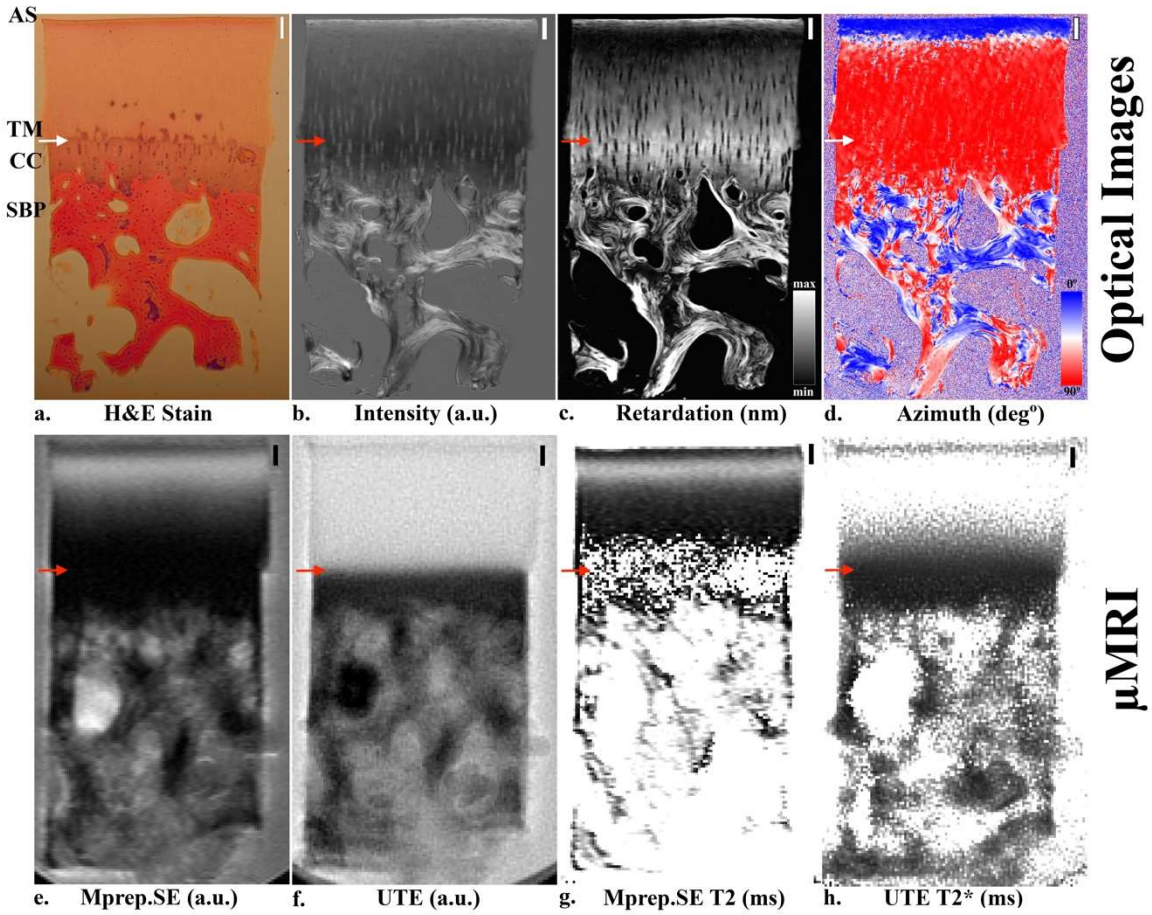

Figure 6.4 A specimen imaged using multiple modalities. Four optical images (0.26 µm/pixel for H&E (a); 2 µm/pixel for PLM (b, c, and d)): (a) a color optical image of H&E-stained slice, (b) an intensity image of an unstained slice, (c) the quantitative retardation map, and (d) the quantitative angle map of the same unstained slice as in (b). Four µMRI images: (e) Mprep.SE intensity image, (f) UTE intensity image, and quantitative T2 maps from Mprep.SE (g) and UTE (h) methods. The vertical scale bars (top-right) in all images are 100 µm. The red and white arrows mark the identical location of the tidemark (TM).

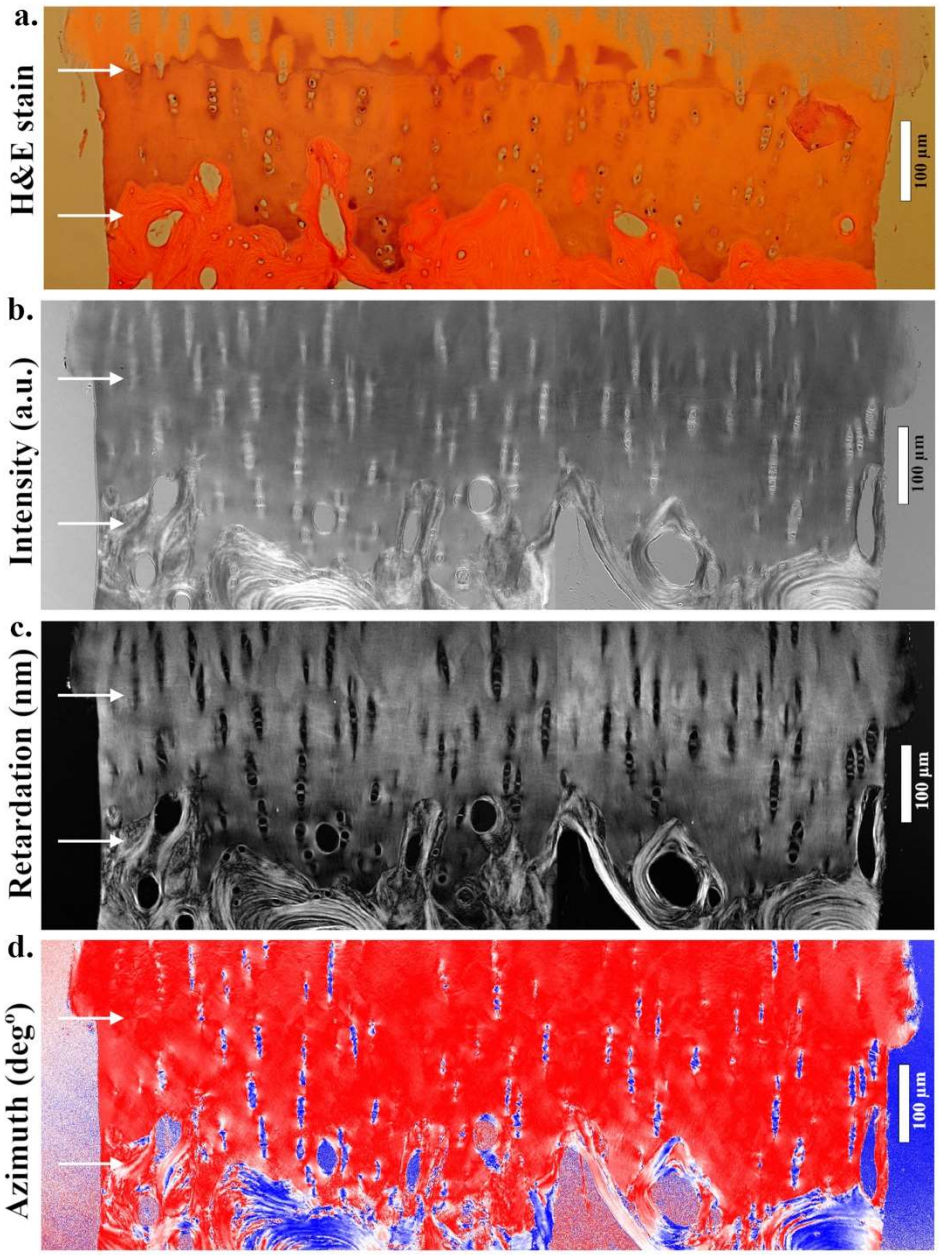

Figure 6.5 Optical images at higher resolution (0.13 µm/pixel for H&E (a); 0.5 µm/pixel for PLM (b, c, and d)) of the cartilage-bone interface region. The region between two arrows in each image marks the ZCC. The white color scalebars are 100 µm.

6.2.4 Quantitative μMRI and PLM Profiles of Non-Calcified and Calcified Cartilage-Bone Plug

Figure 6.6.a shows the quantitative depth-dependent T2 and T2* profiles (0º vs 55º), where the SE sequence can accurately measure much of the non-calcified region of articular cartilage (SZ, TZ and RZ1). Due to the stronger dipolar influence on T2 relaxation, the 0˚ SE-based μMRI can only quantify T2 to RZ1, beyond which the quantitative calculations become too noisy to be reliable. The minimization of the dipolar interaction at 55˚ enables the T2 55˚ profile to reach the tidemark. With a TE as short as a fraction of one ms, UTE-based sequences can quantify T2* in both RZ2 and ZCC. Figure 6.6.b shows the quantitative PLM profiles, where the profile features correlate well with the zonal features of μMRI T2 and T2* profiles. As evident in the PLM profiles, the collagen properties continue the trends in RZ beyond the deepest region of the non-calcified cartilage, across the tidemark and into ZCC, which supports the quantitative T2* data from UTE sequence in Figure 6.6.a, as well as the observations from the images shown in Figure 6.5.

Figure 6.7 enlarges the quantitative profiles in Figure 6.6 between the deep cartilage and SBP. Since the collagen fibers in ZCC retain their orientation from RZ to ZCC, the anisotropy profiles (i.e., the orientational dependent values at 0˚ vs 55˚) by the UTE sequence at the tidemark and ZCC tissues (Figure 6.7.a) reflect reliably the magic angle effect in this segment of calcified cartilage and bony structure. The UTE-based measurement complements the SE/GE-based measurement in μMRI. Beyond ~650μm in tissue depth, the angle profile deviates from the 90˚ orientation, and the retardation

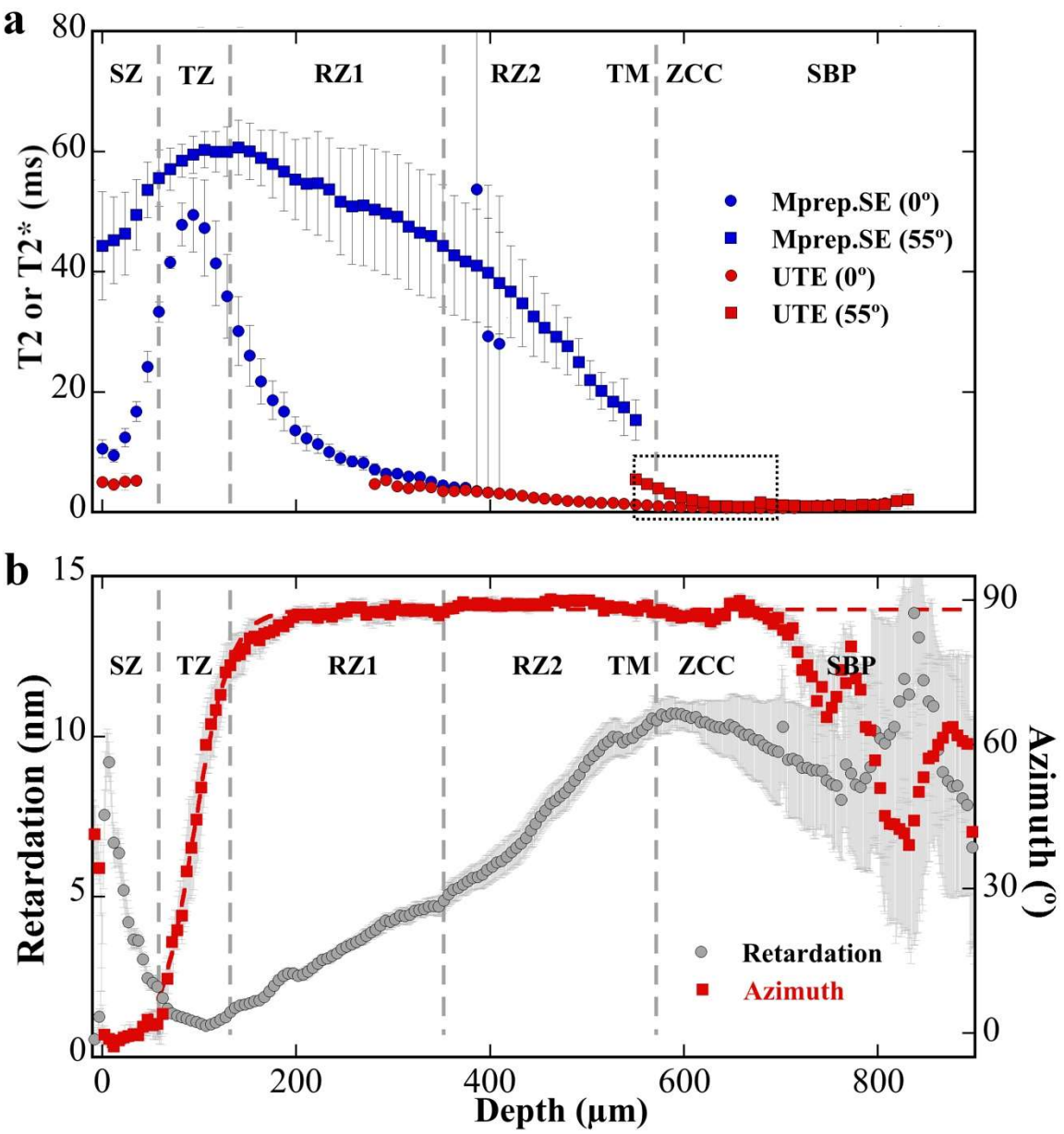

Figure 6.6 Quantitative and ROI-averaged depth-dependent profiles (a) μMRI and (b) PLM. The dashed box in (a) marks the region in both μMRI and PLM that is enlarged in Figure 6.7.

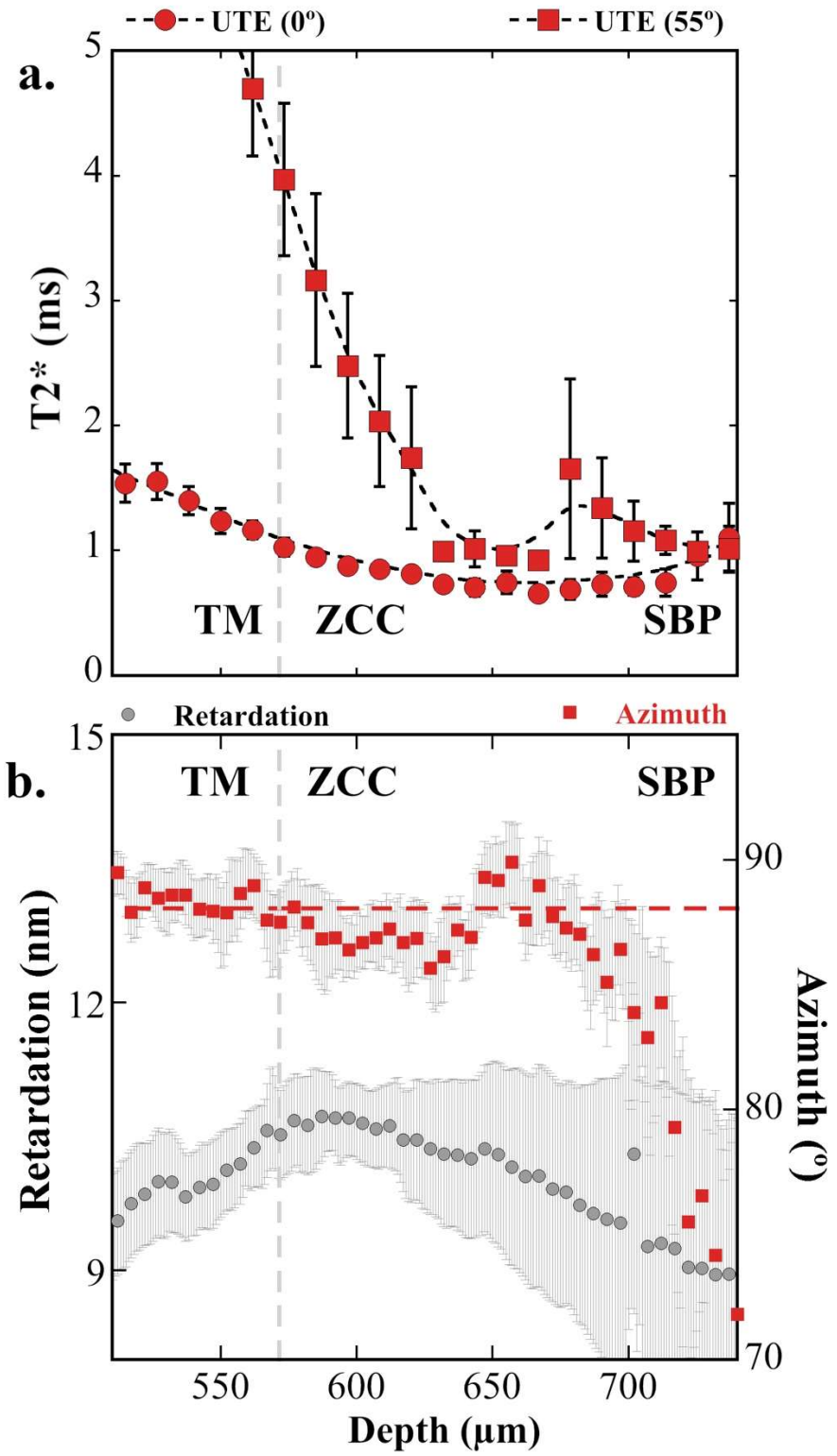

Figure 6.7 An enlargement of the μMRI UTE data and the PLM data of the calcified cartilage and SBP interface region.

profile starts to have large deviations (Figure 6.7.b), which corresponds to the vanishing of the magic angle effect in that region as observed in μMRI (Figure 6.7.a).

It should be noted that the individual images and fitting profiles from Fig 6.1 to Fig 6.5, as well as the fitting values in Table 6.1 and Table 6.2 were from the same single specimen. The profiles in Fig 6.6 and Fig 6.7 were the averaged profiles from all five specimens. The averaged T2* profiles in the calcified cartilage region in Figure 7a shows the UTE T2 at 55º on average was 3.19±0.40 ms, which was greater than UTE T2 at 0º (0.99±0.13 ms) with a high statistical significance ($p<0.0001$). This μMRI data correlates well with the PLM data in Figure 6.7.b where the Azimuth holds at around 90º and the Retardation is the highest among this region with a considerable low standard error.

6.3 Discussion

The structural integrity of the calcified cartilage and subchondral bone region is crucially important to the health of synovial joints. Any weakening or damage to this interface region could trigger the onset of osteoarthritis and other joint diseases (Brandt et al., 1991; Brandt et al., 2006; Dedrick et al., 1993; Findlay & Kuliwaba, 2016). Since MRI is a non-invasive imaging method without the use of any toxic agents or any radiation, the ability to monitor this interface region by MRI could be central to the treatment and management of OA. Due to the resolution limitation, however, most clinical MRI studies of musculoskeletal diseases examine the end stage cartilage degradation. With a transverse resolution as fine as sub-10μm in μMRI (Batool, Mahar, Badar, Tetmeyer, & Xia, 2020), μMRI is capable of measuring the heterogeneity of non-calcified cartilage in the lab and correlating the μMRI results with the higher resolution optical imaging of animal OA models (Alhadlaq et al., 2004; Lee et al., 2014; Lee et al.,

2016; Mittelstaedt, Kahn, & Xia, 2018; N. Wang, Badar, & Xia, 2015). In addition, standard MRI sequences (SE and GE based) are unable to accurately measure the short T2 components in deep cartilage and ZCC because of the mineralized collagen fibers (Biswas et al., 2012; Nakasa, Adachi, Kato, & Ochi, 2014). The use of μMRI with UTE capability is essential in the quantitative studies of calcified cartilage and the cartilage-bone interface at a high resolution.

In this study, the quantitative UTE imaging in μMRI was used for the first time together with the quantitative imaging by the higher resolution optical microscopy. Cartilage-bone specimens from a well-studied and well-documented canine model were used (Xia, 2008). The non-calcified region of the cartilage-bone specimens correlates well with the previously published results, where the μMRI T2 at 0º and 55˚ confirms the magic angle effect due to the fibril architectures across the non-calcified tissue depth (Xia, 2008). These features of μMRI also correlate well with the measurement from clinical MRI at a lower resolution (Novakofski et al., 2015). By coalescing the UTE and Spin Echo T2 data, we extend the measurement of T2 to ZCC, with the aid of correlative quantitative optical imaging.

6.3.1 Quantitative Properties of Non-Calcified and Calcified Cartilage

Polarized light microscopy is a gold standard measure of anisotropic properties in any biological as well as non-biological material (Oldenbourg & Mei, 1995). Using PLM, quantitative high-resolution retardation and angle images have been used to provide further insights into tissue structures measured by μMRI (Xia, Moody, Alhadlaq, et al., 2002). This study showed that the H&E staining can visually reveal the boundaries among non-calcified cartilage, calcified cartilage, and subchondral bone (Deng et al.,

2016). Although the existence of these interfaces is reflected indirectly in the quantitative μMRI profiles using UTE, they are not directly distinguishable in μMRI SE or GE sequences due to the strong dipolar interaction. Interestingly, although the three types of tissues emphasized in Figure 6.5 seem to be quite different from the H&E image (Figure 6.5.a), the quantitative data show that the orientation of the collagen fibers and the packing density (hence the optical retardation) do not vary significantly over this interface region. The fibers keep their orientation and organization from RZ, beyond the tidemark and ZCC and extend into SBP. The degradation of the optical properties beyond the 650μm depth in the quantitative profiles is due to the practical way these profiles are row-averaged within a multiple column (ROI). When the bony voids start to appear in SBP, the averaged organization of the collagen fibers are disrupted, hence, leading to larger standard deviations.

A sophisticated study of the deep cartilage and interface regions by optical imaging helps to better understand the tissues by non-invasive and non-destructive μMRI with the use of UTE sequences to determine the T2 characteristic of biological tissue (Du et al., 2013; Fabich et al., 2016). In the cartilage-bone specimens, the deep portion of the non-calcified cartilage, ZCC and SBP have intermediate to short T2 due to the amount of the minerals and strong dipolar interaction (Shao et al., 2016). When the cartilage-bone specimens are oriented at 54.7º (magic angle) to the magnetic field, the tissue appears thicker and brighter in the GE/SE-based imaging sequences, which allows the accurate measurement of tissue thickness (N. Wang et al., 2018). To visualize and quantify the deep RZ and ZCC, one needs the UTE sequences, which has TE as short as tens to hundreds of μs. We show in this study that the existence of the magic angle effect in the

deep portion of the non-calcified cartilage, ZCC, is verifiable when correlating the quantitative UTE data (μMRI) with the optical data (PLM) (Figure 6.7).

6.3.2 Experimental Notes

Due to the thinness of this interface region, high resolution is a necessity in imaging to quantify the structural anisotropy in these tissues by MRI and PLM. Due to the destructive nature of optical imaging, our approach is limited to the animal tissue study and ex-vivo human tissue study. As evident in this study, having a higher resolution certainly enhances the knowledge gained from these types of quantitative projects. In addition, being able to correlate the non-invasive μMRI results and the complementary PLM results further enhances the appreciation for the roles of tissue morphology on these quantitative measurements. Finally, this study uses several MRI sequences, from the GE sequence which are common in clinical MRI, to the SE sequence where quantitative measurement is much less sensitive to the experimental parameters and conditions, and finally, to the UTE sequence which has the potential to see the invisible regions in GE/SE imaging. In clinical settings where the resolution is limited, a subtraction of different images would allow for a qualitative quantification of SBP (Bae et al., 2014). By the concept of a "scaling law" in MRI (Xia, 2007), the knowledge gained from microscopic imaging should facilitate fast advancement of MRI applications in calcified cartilage (Kuo, Panchal, Tanenbaum, & Crues, 2007; Pakin et al., 2006; Regatte & Schweitzer, 2007).

6.3.3 Conclusion

In this study, T2 anisotropy in the interface region (calcified cartilage) between the deep non-calcified cartilage and subchondral bone plate was quantified at the highest

MRI resolution. In addition, the same region of tissue was studied by quantitative optical microscopy. The ultra-short T2 properties and the optical characteristics in this interface region of tissues were compared accurately. To the best of our knowledge, this is the first quantitative measure of structural anisotropy in the deep non-calcified cartilage and subchondral bone plate by high-resolution MRI supported by high magnification gold standard of optical microscopy. Enhanced understanding by complementary correlation provides a more inclusive understanding of the tissue properties in this important interface region, whose changes can be instrumental to the initiation and development of OA.

CHAPTER SEVEN

SUMMARY AND FUTURE DIRECTIONS

It is rare to have the opportunity to access two different MRI systems that are at the two ends of imaging resolution for animal model studies: one system when an animal joint is imaged has a resolution similar to that on a clinical whole-body scanner for humans, while the other system has the highest MRI resolution in the field for quantitative micro-imaging. In addition, we were able to image the same/similar tissue samples at these two different resolutions, which helps in the understanding of necessary requirements for diagnostic measurements of early osteoarthritis in humans.

Studies of animal models of OA from early to late stages are essential to track the progression of cartilage degradation which helps in the clarification of the poorly defined structural and biochemical modifications of extracellular matrix within the articular cartilage. The normal function of articular cartilage (i.e., when the joint is healthy) that is crucial can be observed by sensitive techniques such as MRI T2 relaxation anisotropy, which can monitor the molecular motion of water in the structure and architecture of the extracellular matrix in articular cartilage. μMRI results provide a reachable goal for clinical radiologists and researchers as well as medical imaging manufacturers to improve the clinical resolution based on the resolution limits that are needed to resolve the subtle changes in articular cartilage morphology and function.

Multi-resolution MRI at the same field strength (7 Tesla magnet) was used throughout this work to examine the Pond-Nuki model of OA on canine articular cartilage. A bridge between experimental high-resolution MRI and pre-clinical MRI

setting were put together to explore the importance of topographical and zonal variations when there are changes in articular cartilage due to osteoarthritis. These studies explored the important roles of zonal division in MRI with respect to the histological thickness of the sub-tissue zones in articular cartilage. The ability to detect changes in articular cartilage due to early and late stages of OA between low-resolution and high-resolution MRI is an important task for building a bridge to further improve the clinical diagnostic capabilities and further expand our knowledge in the complicated initiation of early signs of tissue degradation.

The first study (Chapter 4) explored the interpolation of T2 images, which can better detect the degradation in articular cartilage due to OA. When the MRI resolution is insufficient to resolve the depth-dependent T2 characteristics in articular cartilage, an unequal zonal division is shown to be much more statistically informative than the typical equal zone division and hence able to detect earlier signs of T2 changes due to tissue degradation. Since the relative length scale of depth-dependent canine articular cartilage and the low-resolution macro-MRI is nearly identical to that of human cartilage and whole-body MRI, the unequal zonal analysis method of image analysis approach is beneficial in a clinical diagnosis of early OA in humans.

In the second study (Chapter 5), an overall positive correlation between the T2 values and tissue degradation can be reached regardless of the resolution of MRI with better findings in the high-resolution μMRI T2, the depth dependence of tissue degradation where the surface tissue had the most changes, and the location-dependence of tissue degradation over the tibial surface. To the best of our knowledge, the MRI T2 results are the first quantitative and multi-resolution characterization of cartilage at five

independent locations over the medial tibial surface in an animal model of OA. We showed that in the early degradation of OA, the changes in cartilage properties are influenced strongly by the ability to image small locations topographically and small tissue depths zonally. A topographical view with fine zonal resolution is crucial for diagnostic detection of early OA by any imaging tool. In addition, the contralateral cartilage can have different degradation patterns than seen in OA cartilage. The use of MRI imaging protocols can also influence the data interpretation. The use of dual resolutions in MRI in this project provides a scalable translational pathway between bench and bedside.

In the third study (Chapter 6), the properties in the interface region (calcified cartilage) between the deep region of the non-calcified cartilage and subchondral bone plate were quantified at the highest MRI resolution via T2 anisotropy. In correlation for confirmation, the same region of the same tissues was studied by quantitative optical microscopy. The ultra-short T2 properties and the optical characteristics in this interface region of tissues were compared accurately. To the best of our knowledge, this is the first quantitative measure of structural anisotropy by high-resolution MRI supported by high magnification gold standard of optical microscopy. Enhanced understanding by complementary correlation provides a more inclusive understanding of the tissue properties in this important interface region, whose changes can be instrumental to the initiation and development of OA.

From these studies, it is evident that higher resolution MRI is a requirement in diagnostic capabilities of osteoarthritis in synovial joints. With improvements and advances in clinical MRI instrumentation to increase the resolution and better sequences

and image acquisition, the probability of qualitative and quantitative measure of early signs of tissue degradation in synovial joints is high. Artificial intelligence and neural network computing, better and faster quantitative imaging of disease progression is conceivable with emphasis on segmentation of whole joint to measure the progression of the disease topographically and depth-dependently. With faster sequences, like UTE, Zero Echo (ZE) and UTE-3D, measurement of calcified tissue with very short T2 due to the low mobility of water is showing improvement in the detection of disease progression from the bone and calcified cartilage.

Here are some future improvements feasible in the analysis of the osteoarthritic cartilage data presented in this dissertation that can be done by other methods of analysis or some additional experiments. Firstly, the method of segmentation on the whole joint using the low-resolution MRI T2 data to create a contour map to help in visualizing a quantitative measure of cartilage degradation at different stages of OA. Second, further improve the application of quantitative measure of UTE T2* to measure the changes in the calcified cartilage due to impact driven OA or ACL OA. Third, the application of compressed sensing to shorten the time to acquire high-resolution quantitative T2, using magnetized prepared spin-echo sequence and measure changes in experimental osteoarthritic articular cartilage. Finally, using quantitative polarized light microscopy for the measure of chondrocyte shapes in relation to the neighboring local collagen fiber orientation in OA cartilage can help in the understanding of cell and fiber relationships in healthy and disease articular cartilage.

APPENDIX A

COPYRIGHT LETTERS OF PERMISSION TO REPRODUCE

Letter #1: CCC right granting permission to reproduce Chapter 4 in its entirety.

CCC Marketplace™

This is a License Agreement between Farid Badar ("User") and Copyright Clearance Center, Inc. ("CCC") on behalf of the Rightsholder identified in the order details below. The license consists of the order details, the CCC Terms and Conditions below, and any Rightsholder Terms and Conditions which are included below.

All payments must be made in full to CCC in accordance with the CCC Terms and Conditions below.

Order Date	29-Jan-2022	Type of Use	Republish in a thesis/dissertation
Order License ID	1183699-1		
ISSN	2223-4306	Publisher	AME Publishing Company
		Portion	Chapter/article

LICENSED CONTENT

Publication Title	Quantitative imaging in medicine and surgery	Publication Type	Journal
		Start Page	227
Article Title	Image interpolation improves the zonal analysis of cartilage T2 relaxation in MRI.	End Page	237
		Issue	2
		Volume	7
Date	01/01/2011	URL	http://www.amepc.org/qims
Language	English		
Country	China		
Rightsholder	Nancy International Ltd Subsidiary AME Publishing Company		

REQUEST DETAILS

Portion Type	Chapter/article	Rights Requested	Main product
Page range(s)	227-237	Distribution	United States
Total number of pages	10	Translation	Original language of publication
Format (select all that apply)	Print, Electronic	Copies for the disabled?	No
Who will republish the content?	Academic institution	Minor editing privileges?	No
Duration of Use	Life of current edition	Incidental promotional use?	No
Lifetime Unit Quantity	Up to 499	Currency	USD

NEW WORK DETAILS

Title	Image interpolation improves the zonal analysis of cartilage T2 relaxation in MRI	Institution name	Oakland University
		Expected presentation date	2022-03-15
Instructor name	Yang Xia		

ADDITIONAL DETAILS

Order reference number	1	**The requesting person / organization to appear on the license**	Farid Badar

REUSE CONTENT DETAILS

Title, description or numeric reference of the portion(s)	Image interpolation improves the zonal analysis of cartilage T2 relaxation in MRI	**Title of the article/chapter the portion is from**	Image interpolation improves the zonal analysis of cartilage T2 relaxation in MRI.
Editor of portion(s)	Badar, Farid; Xia, Yang	**Author of portion(s)**	Badar, Farid; Xia, Yang
Volume of serial or monograph	7	**Issue, if republishing an article from a serial**	2
Page or page range of portion	227-237	**Publication date of portion**	2017-04-01

RIGHTSHOLDER TERMS AND CONDITIONS

It is the responsibility of the users' to identify the copyright holder of any materials. If the user has any doubts, please contact the publisher at permissions@amegrouops.com. For illustrations owned by Ms. Croce, please contact beth@bioperspective.com.

CCC Terms and Conditions

1. Description of Service; Defined Terms. This Republication License enables the User to obtain licenses for republication of one or more copyrighted works as described in detail on the relevant Order Confirmation (the "Work(s)"). Copyright Clearance Center, Inc. ("CCC") grants licenses through the Service on behalf of the rightsholder identified on the Order Confirmation (the "Rightsholder"). "Republication", as used herein, generally means the inclusion of a Work, in whole or in part, in a new work or works, also as described on the Order Confirmation. "User", as used herein, means the person or entity making such republication.

2. The terms set forth in the relevant Order Confirmation, and any terms set by the Rightsholder with respect to a particular Work, govern the terms of use of Works in connection with the Service. By using the Service, the person transacting for a republication license on behalf of the User represents and warrants that he/she/it (a) has been duly authorized by the User to accept, and hereby does accept, all such terms and conditions on behalf of User, and (b) shall inform User of all such terms and conditions. In the event such person is a "freelancer" or other third party independent of User and CCC, such party shall be deemed jointly a "User" for purposes of these terms and conditions. In any event, User shall be deemed to have accepted and agreed to all such terms and conditions if User republishes the Work in any fashion.

3. Scope of License; Limitations and Obligations.

    3.1. All Works and all rights therein, including copyright rights, remain the sole and exclusive property of the Rightsholder. The license created by the exchange of an Order Confirmation (and/or any invoice) and payment by User of the full amount set forth on that document includes only those rights expressly set forth in the Order Confirmation and in these terms and conditions, and conveys no other rights in the Work(s) to User. All rights not expressly granted are hereby reserved.

    3.2. General Payment Terms: You may pay by credit card or through an account with us payable at the end of the month. If you and we agree that you may establish a standing account with CCC, then the following terms apply: Remit Payment to: Copyright Clearance Center, 29118 Network Place, Chicago, IL 60673-1291. Payments Due: Invoices are payable upon their delivery to you (or upon our notice to you that they are available to you for downloading). After 30 days, outstanding amounts will be subject to a service charge of 1-1/2% per month or, if less, the maximum rate allowed by applicable law. Unless otherwise specifically set forth in the Order Confirmation or in a separate written agreement signed by CCC, invoices are due and

payable on "net 30" terms. While User may exercise the rights licensed immediately upon issuance of the Order Confirmation, the license is automatically revoked and is null and void, as if it had never been issued, if complete payment for the license is not received on a timely basis either from User directly or through a payment agent, such as a credit card company.

3.3. Unless otherwise provided in the Order Confirmation, any grant of rights to User (i) is "one-time" (including the editions and product family specified in the license), (ii) is non-exclusive and non-transferable and (iii) is subject to any and all limitations and restrictions (such as, but not limited to, limitations on duration of use or circulation) included in the Order Confirmation or invoice and/or in these terms and conditions. Upon completion of the licensed use, User shall either secure a new permission for further use of the Work(s) or immediately cease any new use of the Work(s) and shall render inaccessible (such as by deleting or by removing or severing links or other locators) any further copies of the Work (except for copies printed on paper in accordance with this license and still in User's stock at the end of such period).

3.4. In the event that the material for which a republication license is sought includes third party materials (such as photographs, illustrations, graphs, inserts and similar materials) which are identified in such material as having been used by permission, User is responsible for identifying, and seeking separate licenses (under this Service or otherwise) for, any of such third party materials; without a separate license, such third party materials may not be used.

3.5. Use of proper copyright notice for a Work is required as a condition of any license granted under the Service. Unless otherwise provided in the Order Confirmation, a proper copyright notice will read substantially as follows: "Republished with permission of [Rightsholder's name], from [Work's title, author, volume, edition number and year of copyright]; permission conveyed through Copyright Clearance Center, Inc. " Such notice must be provided in a reasonably legible font size and must be placed either immediately adjacent to the Work as used (for example, as part of a by-line or footnote but not as a separate electronic link) or in the place where substantially all other credits or notices for the new work containing the republished Work are located. Failure to include the required notice results in loss to the Rightsholder and CCC, and the User shall be liable to pay liquidated damages for each such failure equal to twice the use fee specified in the Order Confirmation, in addition to the use fee itself and any other fees and charges specified.

3.6. User may only make alterations to the Work if and as expressly set forth in the Order Confirmation. No Work may be used in any way that is defamatory, violates the rights of third parties (including such third parties' rights of copyright, privacy, publicity, or other tangible or intangible property), or is otherwise illegal, sexually explicit or obscene. In addition, User may not conjoin a Work with any other material that may result in damage to the reputation of the Rightsholder. User agrees to inform CCC if it becomes aware of any infringement of any rights in a Work and to cooperate with any reasonable request of CCC or the Rightsholder in connection therewith.

4. Indemnity. User hereby indemnifies and agrees to defend the Rightsholder and CCC, and their respective employees and directors, against all claims, liability, damages, costs and expenses, including legal fees and expenses, arising out of any use of a Work beyond the scope of the rights granted herein, or any use of a Work which has been altered in any unauthorized way by User, including claims of defamation or infringement of rights of copyright, publicity, privacy or other tangible or intangible property.

5. Limitation of Liability. UNDER NO CIRCUMSTANCES WILL CCC OR THE RIGHTSHOLDER BE LIABLE FOR ANY DIRECT, INDIRECT, CONSEQUENTIAL OR INCIDENTAL DAMAGES (INCLUDING WITHOUT LIMITATION DAMAGES FOR LOSS OF BUSINESS PROFITS OR INFORMATION, OR FOR BUSINESS INTERRUPTION) ARISING OUT OF THE USE OR INABILITY TO USE A WORK, EVEN IF ONE OF THEM HAS BEEN ADVISED OF THE POSSIBILITY OF SUCH DAMAGES. In any event, the total liability of the Rightsholder and CCC (including their respective employees and directors) shall not exceed the total amount actually paid by User for this license. User assumes full liability for the actions and omissions of its principals, employees, agents, affiliates, successors and assigns.

6. Limited Warranties. THE WORK(S) AND RIGHT(S) ARE PROVIDED "AS IS". CCC HAS THE RIGHT TO GRANT TO USER

THE RIGHTS GRANTED IN THE ORDER CONFIRMATION DOCUMENT. CCC AND THE RIGHTSHOLDER DISCLAIM ALL OTHER WARRANTIES RELATING TO THE WORK(S) AND RIGHT(S), EITHER EXPRESS OR IMPLIED, INCLUDING WITHOUT LIMITATION IMPLIED WARRANTIES OF MERCHANTABILITY OR FITNESS FOR A PARTICULAR PURPOSE. ADDITIONAL RIGHTS MAY BE REQUIRED TO USE ILLUSTRATIONS, GRAPHS, PHOTOGRAPHS, ABSTRACTS, INSERTS OR OTHER PORTIONS OF THE WORK (AS OPPOSED TO THE ENTIRE WORK) IN A MANNER CONTEMPLATED BY USER; USER UNDERSTANDS AND AGREES THAT NEITHER CCC NOR THE RIGHTSHOLDER MAY HAVE SUCH ADDITIONAL RIGHTS TO GRANT.

7. Effect of Breach. Any failure by User to pay any amount when due, or any use by User of a Work beyond the scope of the license set forth in the Order Confirmation and/or these terms and conditions, shall be a material breach of the license created by the Order Confirmation and these terms and conditions. Any breach not cured within 30 days of written notice thereof shall result in immediate termination of such license without further notice. Any unauthorized (but licensable) use of a Work that is terminated immediately upon notice thereof may be liquidated by payment of the Rightsholder's ordinary license price therefor; any unauthorized (and unlicensable) use that is not terminated immediately for any reason (including, for example, because materials containing the Work cannot reasonably be recalled) will be subject to all remedies available at law or in equity, but in no event to a payment of less than three times the Rightsholder's ordinary license price for the most closely analogous licensable use plus Rightsholder's and/or CCC's costs and expenses incurred in collecting such payment.

8. Miscellaneous.

    8.1. User acknowledges that CCC may, from time to time, make changes or additions to the Service or to these terms and conditions, and CCC reserves the right to send notice to the User by electronic mail or otherwise for the purposes of notifying User of such changes or additions; provided that any such changes or additions shall not apply to permissions already secured and paid for.

    8.2. Use of User-related information collected through the Service is governed by CCC's privacy policy, available online here:https://marketplace.copyright.com/rs-ui-web/mp/privacy-policy

    8.3. The licensing transaction described in the Order Confirmation is personal to User. Therefore, User may not assign or transfer to any other person (whether a natural person or an organization of any kind) the license created by the Order Confirmation and these terms and conditions or any rights granted hereunder; provided, however, that User may assign such license in its entirety on written notice to CCC in the event of a transfer of all or substantially all of User's rights in the new material which includes the Work(s) licensed under this Service.

    8.4. No amendment or waiver of any terms is binding unless set forth in writing and signed by the parties. The Rightsholder and CCC hereby object to any terms contained in any writing prepared by the User or its principals, employees, agents or affiliates and purporting to govern or otherwise relate to the licensing transaction described in the Order Confirmation, which terms are in any way inconsistent with any terms set forth in the Order Confirmation and/or in these terms and conditions or CCC's standard operating procedures, whether such writing is prepared prior to, simultaneously with or subsequent to the Order Confirmation, and whether such writing appears on a copy of the Order Confirmation or in a separate instrument.

    8.5. The licensing transaction described in the Order Confirmation document shall be governed by and construed under the law of the State of New York, USA, without regard to the principles thereof of conflicts of law. Any case, controversy, suit, action, or proceeding arising out of, in connection with, or related to such licensing transaction shall be brought, at CCC's sole discretion, in any federal or state court located in the County of New York, State of New York, USA, or in any federal or state court whose geographical jurisdiction covers the location of the Rightsholder set forth in the Order Confirmation. The parties expressly submit to the personal jurisdiction and venue of each such federal or state court.If you have any comments or questions about the Service or Copyright Clearance Center, please contact us at 978-750-8400 or send an e-mail to support@copyright.com.

v 1.1

Letter #2: CCC right granting permission to reproduce Chapter 5 in its entirety.

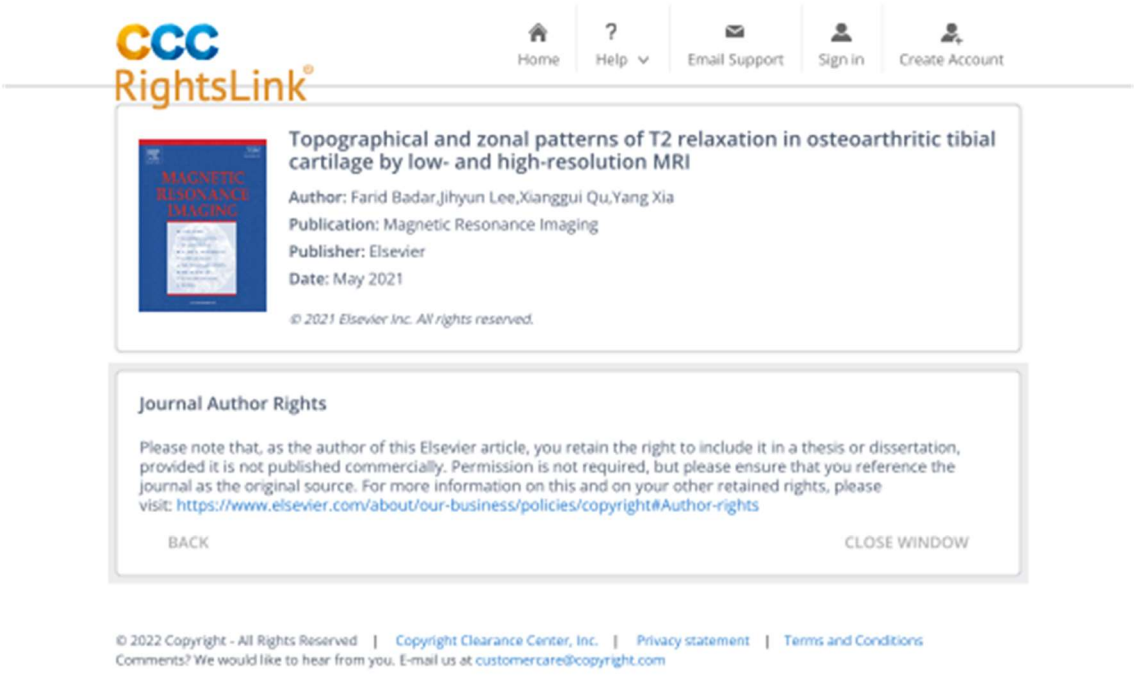

Letter #3: CCC right granting permission to reproduce Chapter 6 in its entirety.

JOHN WILEY AND SONS LICENSE
TERMS AND CONDITIONS

Feb 06, 2022

This Agreement between Farid Badar ("You") and John Wiley and Sons ("John Wiley and Sons") consists of your license details and the terms and conditions provided by John Wiley and Sons and Copyright Clearance Center.

License Number	5238421025841
License date	Jan 29, 2022
Licensed Content Publisher	John Wiley and Sons
Licensed Content Publication	Microscopy Research and Technique
Licensed Content Title	The interface region between articular cartilage and bone by μMRI and PLM at microscopic resolutions
Licensed Content Author	Yang Xia, Farid Badar
Licensed Content Date	Dec 3, 2021
Licensed Content Volume	0
Licensed Content Issue	0
Licensed Content Pages	11

Type of use	Dissertation/Thesis
Requestor type	Author of this Wiley article
Format	Print and electronic
Portion	Full article
Will you be translating?	No
Title	Multi-resolution study of topographical and zonal properties of articular cartilage using MRI T2 and polarized light microscopy
Institution name	Oakland University
Expected presentation date	Mar 2022
Order reference number	1
Requestor Location	Farid Badar 264 Hannah Hall 244 Meadow Brook Road Physics Department ROCHESTER, MI 48309 United States Attn: Farid Badar
Publisher Tax ID	EU826007151
Total	0.00 USD

Terms and Conditions

TERMS AND CONDITIONS

This copyrighted material is owned by or exclusively licensed to John Wiley & Sons, Inc. or one of its group companies (each a"Wiley Company") or handled on behalf of a society with

which a Wiley Company has exclusive publishing rights in relation to a particular work (collectively "WILEY"). By clicking "accept" in connection with completing this licensing transaction, you agree that the following terms and conditions apply to this transaction (along with the billing and payment terms and conditions established by the Copyright Clearance Center Inc., ("CCC's Billing and Payment terms and conditions"), at the time that you opened your RightsLink account (these are available at any time at http://myaccount.copyright.com).

Terms and Conditions

- The materials you have requested permission to reproduce or reuse (the "Wiley Materials") are protected by copyright.

- You are hereby granted a personal, non-exclusive, non-sub licensable (on a stand-alone basis), non-transferable, worldwide, limited license to reproduce the Wiley Materials for the purpose specified in the licensing process. This license, **and any CONTENT (PDF or image file) purchased as part of your order,** is for a one-time use only and limited to any maximum distribution number specified in the license. The first instance of republication or reuse granted by this license must be completed within two years of the date of the grant of this license (although copies prepared before the end date may be distributed thereafter). The Wiley Materials shall not be used in any other manner or for any other purpose, beyond what is granted in the license. Permission is granted subject to an appropriate acknowledgement given to the author, title of the material/book/journal and the publisher. You shall also duplicate the copyright notice that appears in the Wiley publication in your use of the Wiley Material. Permission is also granted on the understanding that nowhere in the text is a previously published source acknowledged for all or part of this Wiley Material. Any third party content is expressly excluded from this permission.

- With respect to the Wiley Materials, all rights are reserved. Except as expressly granted by the terms of the license, no part of the Wiley Materials may be copied, modified, adapted (except for minor reformatting required by the new Publication), translated, reproduced, transferred or distributed, in any form or by any means, and no derivative works may be made based on the Wiley Materials without the prior permission of the respective copyright owner.**For STM Signatory Publishers clearing permission under the terms of the STM Permissions Guidelines only, the terms of the license are extended to include subsequent editions and for editions in other languages, provided such editions are for the work as a whole in situ and does not involve the separate exploitation of the permitted figures or extracts,** You may not alter, remove or suppress in any manner any copyright, trademark or other notices displayed by the Wiley Materials. You may not license, rent, sell, loan, lease, pledge, offer as security, transfer or assign the Wiley Materials on a stand-alone basis, or any of the rights granted to you hereunder to any other person.

- The Wiley Materials and all of the intellectual property rights therein shall at all times remain the exclusive property of John Wiley & Sons Inc, the Wiley Companies, or their respective licensors, and your interest therein is only that of having possession of and the right to reproduce the Wiley Materials pursuant to Section 2 herein during the continuance of this Agreement. You agree that you own no right, title or interest in or to the Wiley Materials or any of the intellectual property rights therein. You shall have no rights hereunder other than the license as provided for above in Section 2. No right, license or interest to any trademark, trade name, service mark or other branding ("Marks") of WILEY or its licensors is granted hereunder, and you agree that you

shall not assert any such right, license or interest with respect thereto

- NEITHER WILEY NOR ITS LICENSORS MAKES ANY WARRANTY OR REPRESENTATION OF ANY KIND TO YOU OR ANY THIRD PARTY, EXPRESS, IMPLIED OR STATUTORY, WITH RESPECT TO THE MATERIALS OR THE ACCURACY OF ANY INFORMATION CONTAINED IN THE MATERIALS, INCLUDING, WITHOUT LIMITATION, ANY IMPLIED WARRANTY OF MERCHANTABILITY, ACCURACY, SATISFACTORY QUALITY, FITNESS FOR A PARTICULAR PURPOSE, USABILITY, INTEGRATION OR NON-INFRINGEMENT AND ALL SUCH WARRANTIES ARE HEREBY EXCLUDED BY WILEY AND ITS LICENSORS AND WAIVED BY YOU.

- WILEY shall have the right to terminate this Agreement immediately upon breach of this Agreement by you.

- You shall indemnify, defend and hold harmless WILEY, its Licensors and their respective directors, officers, agents and employees, from and against any actual or threatened claims, demands, causes of action or proceedings arising from any breach of this Agreement by you.

- IN NO EVENT SHALL WILEY OR ITS LICENSORS BE LIABLE TO YOU OR ANY OTHER PARTY OR ANY OTHER PERSON OR ENTITY FOR ANY SPECIAL, CONSEQUENTIAL, INCIDENTAL, INDIRECT, EXEMPLARY OR PUNITIVE DAMAGES, HOWEVER CAUSED, ARISING OUT OF OR IN CONNECTION WITH THE DOWNLOADING, PROVISIONING, VIEWING OR USE OF THE MATERIALS REGARDLESS OF THE FORM OF ACTION, WHETHER FOR BREACH OF CONTRACT, BREACH OF WARRANTY, TORT, NEGLIGENCE, INFRINGEMENT OR OTHERWISE (INCLUDING, WITHOUT LIMITATION, DAMAGES BASED ON LOSS OF PROFITS, DATA, FILES, USE, BUSINESS OPPORTUNITY OR CLAIMS OF THIRD PARTIES), AND WHETHER OR NOT THE PARTY HAS BEEN ADVISED OF THE POSSIBILITY OF SUCH DAMAGES. THIS LIMITATION SHALL APPLY NOTWITHSTANDING ANY FAILURE OF ESSENTIAL PURPOSE OF ANY LIMITED REMEDY PROVIDED HEREIN.

- Should any provision of this Agreement be held by a court of competent jurisdiction to be illegal, invalid, or unenforceable, that provision shall be deemed amended to achieve as nearly as possible the same economic effect as the original provision, and the legality, validity and enforceability of the remaining provisions of this Agreement shall not be affected or impaired thereby.

- The failure of either party to enforce any term or condition of this Agreement shall not constitute a waiver of either party's right to enforce each and every term and condition of this Agreement. No breach under this agreement shall be deemed waived or excused by either party unless such waiver or consent is in writing signed by the party granting such waiver or consent. The waiver by or consent of a party to a breach of any provision of this Agreement shall not operate or be construed as a waiver of or consent to any other or subsequent breach by such other party.

- This Agreement may not be assigned (including by operation of law or otherwise) by you without WILEY's prior written consent.

- Any fee required for this permission shall be non-refundable after thirty (30) days from receipt by the CCC.

- These terms and conditions together with CCC's Billing and Payment terms and conditions (which are incorporated herein) form the entire agreement between you and WILEY concerning this licensing transaction and (in the absence of fraud) supersedes all prior agreements and representations of the parties, oral or written. This Agreement may not be amended except in writing signed by both parties. This Agreement shall be binding upon and inure to the benefit of the parties' successors, legal representatives, and authorized assigns.

- In the event of any conflict between your obligations established by these terms and conditions and those established by CCC's Billing and Payment terms and conditions, these terms and conditions shall prevail.

- WILEY expressly reserves all rights not specifically granted in the combination of (i) the license details provided by you and accepted in the course of this licensing transaction, (ii) these terms and conditions and (iii) CCC's Billing and Payment terms and conditions.

- This Agreement will be void if the Type of Use, Format, Circulation, or Requestor Type was misrepresented during the licensing process.

- This Agreement shall be governed by and construed in accordance with the laws of the State of New York, USA, without regards to such state's conflict of law rules. Any legal action, suit or proceeding arising out of or relating to these Terms and Conditions or the breach thereof shall be instituted in a court of competent jurisdiction in New York County in the State of New York in the United States of America and each party hereby consents and submits to the personal jurisdiction of such court, waives any objection to venue in such court and consents to service of process by registered or certified mail, return receipt requested, at the last known address of such party.

WILEY OPEN ACCESS TERMS AND CONDITIONS

Wiley Publishes Open Access Articles in fully Open Access Journals and in Subscription journals offering Online Open. Although most of the fully Open Access journals publish open access articles under the terms of the Creative Commons Attribution (CC BY) License only, the subscription journals and a few of the Open Access Journals offer a choice of Creative Commons Licenses. The license type is clearly identified on the article.

The Creative Commons Attribution License

The Creative Commons Attribution License (CC-BY) allows users to copy, distribute and transmit an article, adapt the article and make commercial use of the article. The CC-BY license permits commercial and non-

Creative Commons Attribution Non-Commercial License

The Creative Commons Attribution Non-Commercial (CC-BY-NC)License permits use, distribution and reproduction in any medium, provided the original work is properly cited and is not used for commercial purposes.(see below)

Creative Commons Attribution-Non-Commercial-NoDerivs License

APPENDIX B

T2 MAP CALCULATIONS USING MULTIPLE SOFTWARE AND PROGRAMS

Quantitative T2 experiments have been used in most, if not all, of the publications in which depth-dependent cartilage anisotropy or topographical and zonal cartilage degradation is measured by the changes in T2 (or T2* in some cases). To measure T2 in MRI, sequences such Spin Echo, Gradient Echo or UTE are used in a way where independent images with incrementally varying echo times are acquired. The desired intensity in the images, such as cartilage, tendon, or other musculoskeletal tissues with varying T2 properties, have an intensity decaying property that follows a single or double exponential decay. For a single exponential decay, the most basic form of equation to describe the decay is shown below.

$$S = S_0 * \exp(-\tau/T2) \tag{B.1}$$

where S_0 is the maximum intensity measured at τ equal to 0 or in the practical case would be the shortest echo time. Equation B.1 can also be represented in a linear format.

$$\ln (S/ S_0) = -\tau/T2 \tag{B.2}$$

which is linear representation of $y = mx$, where m represents the slope. With a linear representation, the inverse slope represents the desired T2. But in most biological tissues and the limitations on resolution, the voxel in an image may have multiple T2 that can be represented as two slopes in a linear plot.

Most experimental data have intrinsic noise which present themselves in the form of random (positive) noise fluctuations that are well below the signal amplitude measured from a tissue sample. However, in some cases where the signal from the tissue is weak due to relaxation properties, the signal and noise are much closer in range. For the purpose of a more accurate calculated T2, an addition of noise level or baseline is required in Equation B.1.

$$S = S_0 * \exp(-\tau/T2) + \text{noise} \quad \text{(B.3)}$$

The noise here represents the baseline level where at longer echo time points (τ), the signal from the tissue is around the noise level of the image. With the added noise as a baseline, the fitted T2 calculated for each pixel of the tissue is an accurate measure regardless of the intensity with respect to noise.

Since, acquisitions of the MRI experiments take a long time in our MRI studies, an addition of measurements for the purpose of noise seems to be a waste as it is implicit that at longer echo times the signal is around the level of the noise. For this scenario, a strategy was applied where an averaged noise range was measured from the actual intensity image using a ROI away from the tissue where the signal is essentially representing noise. This averaged noise is applied to echo times in ranges of 500 and 1000ms (for canine samples), which are much higher than the actual experimental echo times (i.e., 2, 8. 20, 50 and 100ms).

To apply this methodology on an actual dataset, a program was written using MATLAB ® and Scilab (opensource) software, where intensity images were entered in the program as image matrices. Using the exponential function (Equation B.3), a single exponential fitting code was written to calculate a T2 image matrix. Using Scilab, a similar exponential fitting program was written that calculated T2. Similarly using the linear fit method shown in Equation B.2, a T2 matrix was calculated. The code is written in a such a manner that the exponential function (or linear function) is fit to a dataset of images, one pixel at a time. The time taken to calculate one T2 image from a five (or more) intensity images takes a relatively long time. In recent years, ImageJ ® has allowed users in the imaging field to write macros or use already written macros and

apply them on multiple images for calculation or modification purposes. One such macro is called '*MRI processor'* that takes intensity images from MRI that are measured using a SE/GE sequence and calculates the T2 using the Equation B.3. Figure B.1(a-d) represents the calculated T2 maps of articular cartilage using echo times (τ) in the range of 2, 8, 20, 50 and 100ms with the added noise at 500 and 1000ms.

To show the difference between the four methods and the reliability of the exponential fit versus the linear fit, ROIs were selected from the exact same location on the cartilage-bone plug. Figure B.1e, represents the depth-dependent T2 profile plot of the same ROI using four different methods, with the ImageJ method with shortest computing time.

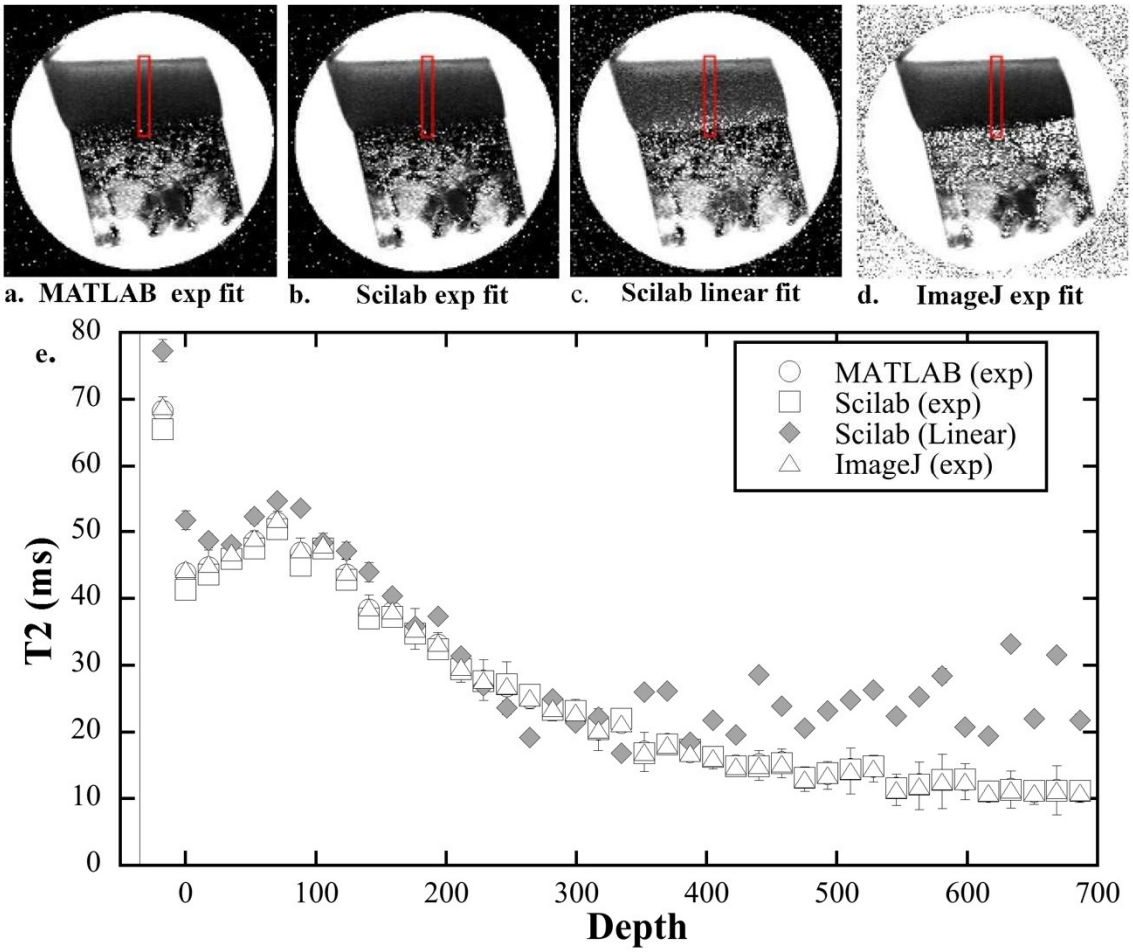

Figure B.1 Calculated T2 maps of articular cartilage-bone plugs using μMRI Spin Echo sequence. Four images were calculated from the sample intensity image set: a) MATLAB ® exponential fit, b) Scilab ® exponential fit, c) Scilab ® linear fit and d) ImageJ ® using exponential fit. T2 profiles (Spin Echo sequence) (e) of articular cartilage-bone plug using the three independent methods of exponential fit and linear fit (SciLab ®)

The MATLAB ® code was written to calculate the T2 map using five (or more) intensity images that were acquired using either a Mprep.SE (Spin Echo) or GE sequence where the intensity decay can be calculated using Equation B.3.

```
%---------------------------------------
% T2 calculation - created by Farid Badar
% Exponential fit: y = A + B*exp(-tau/T2)
%---------------------------------------
warning off all;
clear all;
tic;

%---------------------------------------
% Enter file location of the Bruker sequence raw data%
main = input('Enter main directory: ', 's');      % i.e., /Volumes/Data/uMRIrawdata'
study = input('Enter Study name: ', 's');
scan = input('Enter Scan number: ', 's');
pdata = 'pdata/1/2dseq';
data = strcat(main,'/',study,'/',scan,'/',pdata);
bloc = input('Enter Bloc and exp name: ', 's');
X = input('Enter the X dimension of the image: ');              % X is rows
Y = input('Enter the Y dimension of the image: ');              % Y is columns

%---------------------------------------
Num_Noise = input('Enter the Noise Pixel Size: ');        % Noise matrix size
          NoiseX=2;
%         NoiseY=128;      % for surface rotation
          NoiseY=2;        % for normal case

%---------------------------------------
T2_Default=0.0;                          % A default T2 matrix of 0 values
% Input the tau values with the base noise echo time of 500 and 1000
xap = input('Enter tau values [2 8 20 50 100 500 1000]: ');

%---------------------------------------
% Open file
fid = fopen(data, 'r', 'l');
bimg = fread(fid, [X,(5*Y)],'uint16');
fclose(fid);
bimg = bimg';

%---------------------------------------
% create the bias noise data
```

```
noise=0;
for I = NoiseX:(Num_Noise+NoiseX-1)
        for j = NoiseY:(Num_Noise+NoiseY-1)
        noise=noise+bimg(i,j);
        end
end
noise=noise/(Num_Noise*Num_Noise)
%---------------------------------------
% Create separate images

for i = 1:X
        for j = 1:Y
        t0(i,j) = bimg(i,j);
         t1(i,j) = bimg(i,j+Y);
         t2(i,j) = bimg(i,j+2*Y);
         t3(i,j) = bimg(i,j+3*Y);
         t4(i,j) = bimg(i,j+4*Y);
        end
end
%---------------------------------------

% T2 fitting using exponential fitting function
for i = 1:X
        for j = 1:Y
                 T2(i,j) = T2_Default;
        end
end

for i = 1:X
        for j = 1:Y
                if t0(i,j)>(2*noise)              % Skip pixels that have large noise values

                yap = [t0(i,j) t1(i,j) t2(i,j) t3(i,j) t4(i,j) noise noise];
                [estimates, model] = fitcurve5P(xap, yap, noise);
                A(i,j) = estimates(1,1);
                B(i,j) = estimates(1,2);
                T2(i,j) = estimates(1,3);
                end
        end
end
toc
beep

%---------------------------------------
% Create a directory to save the data
```

```
calc = strcat(main,'/',study,'/',scan,'/','pdata');
mkdir (calc,'2');
result = strcat(calc,'/','2');
%---------------------------------------
% Save the T2 map
T2image = strcat(result,'/','T2-',bloc);
coeffA = strcat(result,'/','A-',bloc);
coeffB = strcat(result,'/','B-',bloc);

fid = fopen(T2image, 'w');
fwrite(fid, T2,'float');
fclose(fid);

fid = fopen(coeffA, 'w');
fwrite(fid, A,'float');
fclose(fid);

fid = fopen(coeffB, 'w');
fwrite(fid, B,'float');
fclose(fid);

 %---------------------------------------
clims = (Wirth et al.);
imagesc(T2',clims);
 %---------------------------------------
```

The code below is the function code that takes the five intensity values (pixel by pixel) with the two noise values and uses the model expfun and calculates the T2, A and B in the exponential equation (y = A + B*exp(-tau/T2)). The calculated values are sent back to main code for image creations. The most important value is the T2 and the sum of errors.

```
function [estimates, model] = fitcurve5P(xap, yap, noise)

MaxInt = yap(1,1)-noise;
Est_T2 = xap(1,7);

for i = 1:7
 if ( (yap(1,i)-noise) < (MaxInt/2.72) )
  Est_T2 = xap(1,i);
 end
end

start_point = [noise MaxInt Est_T2];

model = @expfun;
options = optimset('TolX', 0.01, 'Display','off', 'MaxIter', 255);
estimates = fminsearch(model, start_point, options);

   function [sse, FittedCurve] = expfun(params)
      A = params(1);
      B = params(2);
      T2 = params(3);
      FittedCurve = A + B.* exp(- xap / T2);
      ErrorVector = FittedCurve - yap;
      sse = sum(ErrorVector .^ 2);
   end
end
```

Using Scilab ® to calculate T2 using equation B.3.

```
//---------------------------------------
warning('off');
clear;
tic();
X = 256;
Y = 256;
Num_Noise = 10;
NoiseX = 2;
NoiseY = 2;
T2_Default = 0;
x = input("Enter tau values [2 8 20 50 100 500 1000]: ");

//---------------------------------------

   t0 = read("2dseq-0001.txt",X,Y);
   t1 = read("2dseq-0002.txt",X,Y);
   t2 = read("2dseq-0003.txt",X,Y);
   t3 = read("2dseq-0004.txt",X,Y);
   t4 = read("2dseq-0005.txt",X,Y);

//---------------------------------------

//Noise
//---------------------------------------
noise = 0;

for i = NoiseX:Num_Noise+NoiseX-1
  for j = NoiseY:Num_Noise+NoiseY-1
    noise = noise+t1(i,j);
  end;
end;
noise = noise/(Num_Noise*Num_Noise);
//noise = noise;
//---------------------------------------

// image analysis
//---------------------------------------
for i = 1:X
  for j = 1:Y
    T(i,j) = T2_Default;
  end;
end;
```

```
for i = 1:X
  disp (i/X*100)
  for j = 1:Y
    if t0(i,j)>(2*noise) then
      y = [t0(i,j);t1(i,j);t2(i,j);t3(i,j);t4(i,j);noise;noise];
      w=[2;2;2;2;2;1;1];



function y=yth(x,a)
    y=a(1)+a(2)*exp(-x/a(3))
endfunction

a=[1.0;1.0;1.0]

function e=myfun(a,x,y,w)
    e=w.*(yth(x,a)-y)
endfunction

[f,xopt,gopt]=leastsq(list(myfun,x,y,w),a);

T(i,j) = xopt(3);

else T(i,j)=T(i,j);
    end;
  end;
end;


toc();

write("T2map-Scilabtest-v1",T);
beep
```

APPENDIX C

ARTIFACTS IN UTE IMAGES REFLECT THE DIFFERENCES IN THE EDDY-CURRENT COMPENSATION BETWEEN CHANGING THE APPLIED SHIM CURRENTS VERSUS SHIFTING THE RF FREQUENCY

C.1 Introduction

Ultra-short echo (UTE) MRI can visualize biological tissues and porous media that have very short T2 relaxation times (Fabich et al., 2016; Shao et al., 2016). The reduction of TE is generally done by shortening the time delay between the rf excitation pulses and the signal acquisition. This reduction makes the signals susceptible to the residual eddy currents and other imperfections in the imaging hardware, which can result in various artifacts in the UTE images. In the two Bruker systems, the effects of the eddy currents compensation are compared done by changing the applied shim currents or shifting the rf frequency. This study was performed to measure the differences qualitatively and quantitatively in two Bruker hardware systems by comparing the effects of the B0 correction by either changing the applied shim currents (AVII) or shifting the rf frequency (AVIII HD).

C.2 Materials and Methods

Single and multiple glass tubes containing doped solutions (0.1 and 1% $CuSO_4$) were imaged using a 2D UTE sequence and Spin-Echo (SE) sequence. Two Bruker consoles were used: an AVANCE II (AVII) and an AVANCE IIIHD (AVIIIHD), both using the same 7T/9 cm magnet and same Bruker 25mm rf coil and running the same Paravision 6.0.1 software. The Spin Echo sequence had a TR of 2000ms, TE of ~ 8ms, and a 256-matrix size with 25mm field of view and a bandwidth of 50kHz. The UTE sequence had the same geometry setting except for a TR of 100ms and a minimum TE of ~270μs. The premeasured gradient trajectory was acquired on a glass sphere phantom on both systems.

C.3 Results

C.3.1 Sphere Tube/Single Tube Phantom

A uniform doped solution (0.1% CuSO4) in a spherical glass tube was imaged using a Bruker 25mm saddle coil. The SE images showed uniform signal intensity with the edges of the glass/solution interface showing a sharp edge. AVII UTE image showed a bright ring on the outside of the glass tubes where there is a glass/solution interface. The line profiles across the center of the image (phantoms) clearly show the signal variation and differences of SE and UTE using AVII and AVIII HD systems (Figure C.1).

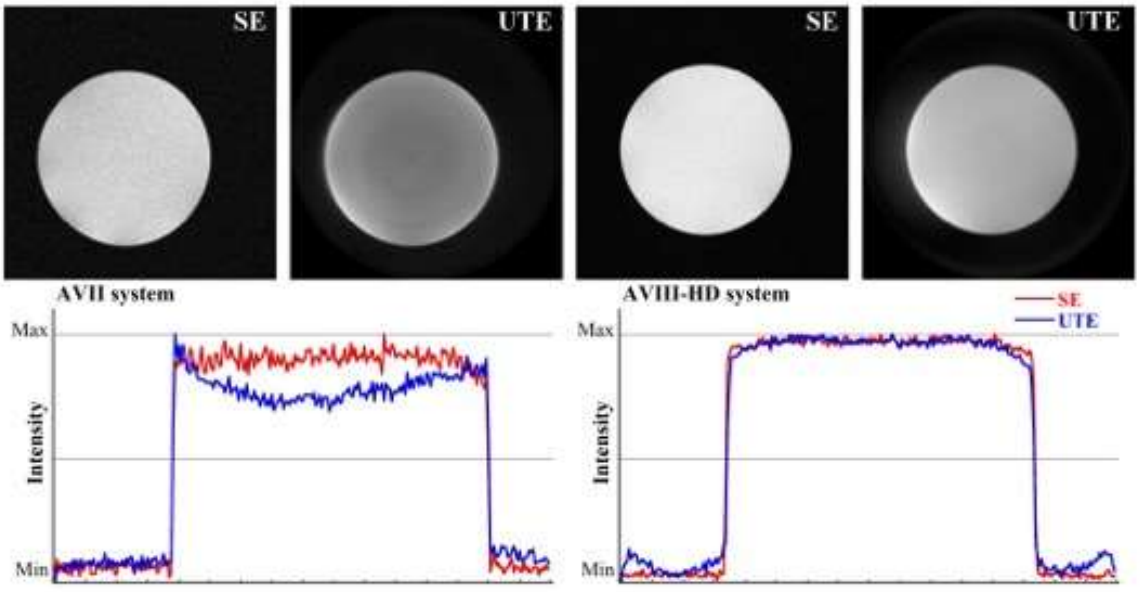

Figure C.1 SE and UTE intensity images and profiles of a single tube with a doped solution using AVII and AVIII HD systems.

C.3.2 Multi-Tube Phantom

A multi-tube setup with doped solution (0.1% and 0.01% CuSO4) in NMR glass tubes was imaged using a Bruker 25mm coil. The SE images showed uniform signal intensity with the signal intensity changes between the edges of the glass/solution interface showing a sharp edge. However, the UTE images showed a bright ring on the outside of the glass tubes where there is a glass/solution interface. The line profiles across the center of the image (phantoms) clearly show the signal variation and differences of SE and UTE using AVII and AVIII HD systems.

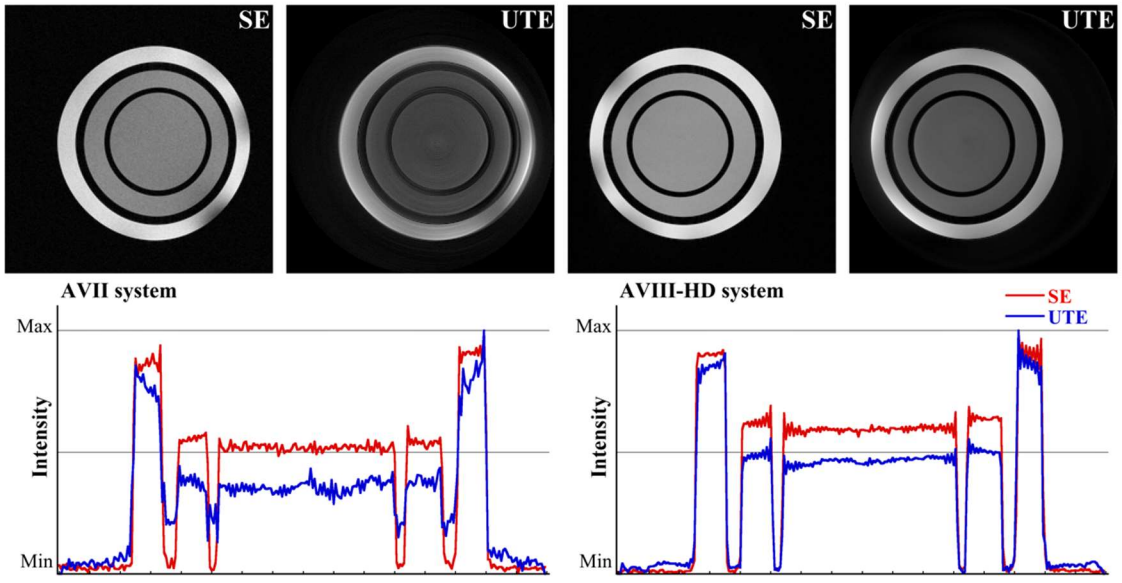

Figure C.2 SE and UTE intensity images and profiles of a multi-tube with a doped solution using AVII and AVIII HD systems.

C.3.3 UTE Decay Errors

Examination of the UTE sequence imaged a tube of saline, on both AVII and AVIIIHD at four different echo times showed the difference in the decay curves due to the artifacts in AVII versus AVIIIHD. AVII showed an unreliable decay ($R^2 = 0.4$) at the edge of the tube (green ROI) versus the inner of the tube (red ROI). AVIIHD showed different yet reliable decay ($R^2 = 0.9$) at both ROIs. From the slopes of the linear decay, it is clear that in regions where neighboring voxels have a drastic intensity change from high to low (i.e., edge of the tube or bone-cartilage interfaces), the measurement of short T2 decay would be unreliable when using the AVII system.

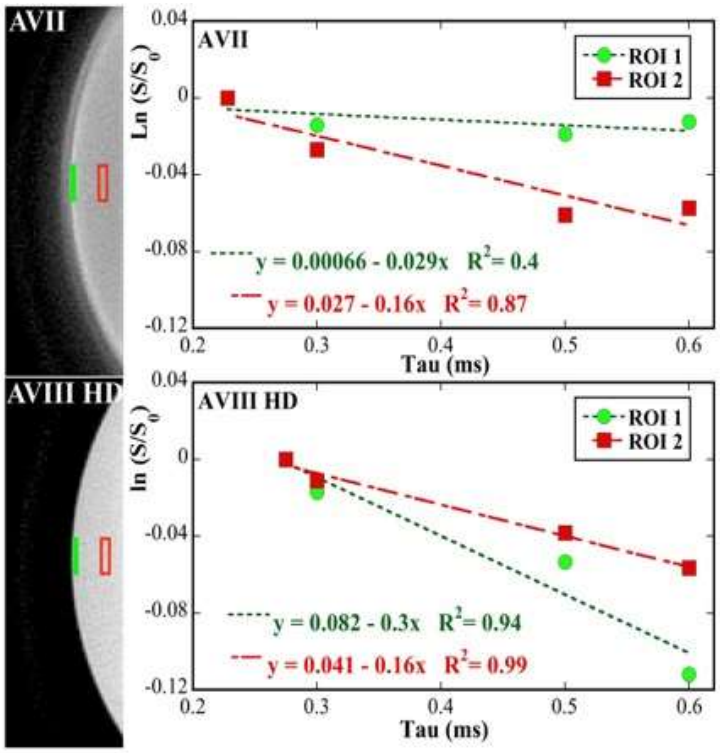

Figure C.3 UTE decay of two ROIs using signal intensity measured from a tube of saline measured by both AVII and AVIII HD systems.

C.4 Discussion

The key differences between the two imaging systems are in the hardware architecture of the consoles, especially as the application of the B0 compensation. AVII analogically adds the correction current to the shim coils for the B0 uniformity correction. AVIIIHD, in contrast, digitally shifts the spectrometer rf frequency during data acquisition (via the FRED unit). AVII UTE (2D) sequences produce a bright ring shown around the outside edge of all glass tubes. This is due to the improper B0 correction method implemented. UTE images on AVIIIHD have minimal artifacts, which result in more reliable measure of the intensity-based quantitative MRI parameters such as the relaxation times and diffusion constants. UTE in the AVIII-HD (and AVIII) systems using the same phantoms produce a better intensity profile much like its SE sequence counterpart. The reason being that the gradient synchronization together with better radial sampling method helps in improving the reconstructed radial FID to image. To improve the signal variations, additional work is in progress which involves regridding method with deapodization has been found to be the reason for the sharp arc in the UTE (2D) with the dip in the intensity of the center of the image. Proper K-space trajectory re-gridding patterns without deapodization improves the effect caused by the improper grid space in radial k-space. These findings were important to better improve the quantitative imaging of articular-bone cartilage to study the calcified cartilage using a UTE 2D sequence. Using UTE in the AVIII HD system was quantitatively more accurate for the study of dipolar interaction in the calcified cartilage (Chapter 6).

REFERENCE

Aizah, N., Chong, P. P., & Kamarul, T. (2019). Early Alterations of Subchondral Bone in the Rat Anterior Cruciate Ligament Transection Model of Osteoarthritis. *Cartilage*, 1947603519878479. doi:10.1177/1947603519878479

Alhadlaq, H. A., & Xia, Y. (2004). The structural adaptations in compressed articular cartilage by microscopic MRI (microMRI) T(2) anisotropy. *Osteoarthritis Cartilage, 12*, 887-894. doi:10.1016/j.joca.2004.07.006

Alhadlaq, H. A., Xia, Y., Moody, J. B., & Matyas, J. R. (2004). Detecting structural changes in early experimental osteoarthritis of tibial cartilage by microscopic magnetic resonance imaging and polarised light microscopy. *Ann Rheum Dis, 63*(6), 709-717. doi:10.1136/ard.2003.011783

Appleyard, R., Burkhardt, D., Ghosh, P., Read, R., Cake, M., Swain, M., & Murrell, G. (2003). Topographical analysis of the structural, biochemical and dynamic biomechanical properties of cartilage in an ovine model of osteoarthritis. *Osteoarthritis and Cartilage, 11*(1), 65-77.

Armstrong, C. G., & Mow, V. C. (1982). Variations in the intrinsic mechanical properties of human articular cartilage with age, degeneration, and water content. *J Bone Joint Surg Am, 64*(1), 88-94.

Armstrong, S. J., Read, R. A., & Price, R. (1995). Topographical variation within the articular cartilage and subchondral bone of the normal ovine knee joint: a histological approach. *Osteoarthritis Cartilage, 3*(1), 25-33.

Badar, F., Lee, J. H., Qu, X., & Xia, Y. (2021). Topographical and zonal patterns of T2 relaxation in osteoarthritic tibial cartilage by low- and high-resolution MRI. *Magnetic Resonance Imaging, 78*(5), 98-108. doi:10.1016/j.mri.2021.01.002

Badar, F., & Xia, Y. (2017). Image interpolation improves the zonal analysis of cartilage T2 relaxation in MRI. *Quant Imaging Med Surg, 7*(2), 227-237. doi:10.21037/qims.2017.03.04

Badar, F., & Xia, Y. (2021). The interface region between articular cartilage and bone by μMRI and PLM at microscopic resolutions. *Microsc Res Tech*. doi:10.1002/jemt.24011

Bae, W. C., Biswas, R., Chen, K., Chang, E. Y., & Chung, C. B. (2014). UTE MRI of the Osteochondral Junction. *Curr Radiol Rep, 2*(2), 35. doi:10.1007/s40134-013-0035-7

Bae, W. C., Dwek, J. R., Znamirowski, R., Statum, S. M., Hermida, J. C., D'Lima, D. D., . . . Chung, C. B. (2010). Ultrashort echo time MR imaging of osteochondral junction of the knee at 3 T: identification of anatomic structures contributing to signal intensity. *Radiology, 254*(3), 837-845.

Bangerter, N. K., Taylor, M. D., Tarbox, G. J., Palmer, A. J., & Park, D. J. (2016). Quantitative techniques for musculoskeletal MRI at 7 Tesla. *Quant Imaging Med Surg, 6*(6), 715-730. doi:10.21037/qims.2016.12.12

Barbour, K. E., Helmick, C. G., Boring, M., & Brady, T. J. (2017). Vital Signs: Prevalence of Doctor-Diagnosed Arthritis and Arthritis-Attributable Activity Limitation - United States, 2013-2015. *MMWR Morb Mortal Wkly Rep, 66*(9), 246-253. doi:10.15585/mmwr.mm6609e1

Basser, P. J., Schneiderman, R., Bank, R. A., Wachtel, E., & Maroudas, A. (1998). Mechanical properties of the collagen network in human articular cartilage as measured by osmotic stress technique. *Arch Biochem Biophys, 351*(2), 207-219. doi:10.1006/abbi.1997.0507

Batool, S., Mahar, R., Badar, F., Tetmeyer, A., & Xia, Y. (2020). Quantitative μMRI and PLM study of rabbit humeral and femoral head cartilage at sub-10 μm resolutions. *J Orthop Res, 38*(5), 1052-1062. doi:10.1002/jor.24547

Benjamin, M., & Evans, E. J. (1990). Fibrocartilage. *J Anat, 171*, 1-15.

Benninghoff, A. (1925). Form und Bau der Gelenkknorpel in ihren Beziehungen zur Funktion. Zweiter Teil: Der aufbau des gelenkknorpels in seinen beziehungen zur funktion. *Zeitschrift für Zellforschung und Mikroskopische Anatomie, 2*(5), 783-862.

Bernstein, M. A., Fain, S. B., & Riederer, S. J. (2001). Effect of windowing and zero‐filled reconstruction of MRI data on spatial resolution and acquisition strategy. *Journal of Magnetic Resonance Imaging, 14*(3), 270-280. doi:10.1002/jmri.1183

Binks, D. A., Hodgson, R. J., Ries, M. E., Foster, R. J., Smye, S. W., McGonagle, D., & Radjenovic, A. (2013). Quantitative parametric MRI of articular cartilage: a review of progress and open challenges. *Br J Radiol, 86*(1023), 20120163. doi:10.1259/bjr.20120163

Biswas, R., Bae, W., Diaz, E., Masuda, K., Chung, C. B., Bydder, G. M., & Du, J. (2012). Ultrashort echo time (UTE) imaging with bi-component analysis: bound and free water evaluation of bovine cortical bone subject to sequential drying. *Bone, 50*(3), 749-755. doi:10.1016/j.bone.2011.11.029

Bjelle, A. (1975). Content and composition of glycosaminoglycans in human knee joint cartilage: variation with site and age in adults. *Connective tissue research, 3*(2-3), 141-147.

Bjelle, A. (1976). Glycosaminoglycans in human articular cartilage of the lower femoral epiphysis in osteoarthrosis. *Scandinavian journal of rheumatology, 6*(1), 37-44.

Blumenkrantz, G., Stahl, R., Carballido-Gamio, J., Zhao, S., Lu, Y., Munoz, T., . . . Majumdar, S. (2008). The feasibility of characterizing the spatial distribution of cartilage T(2) using texture analysis. *Osteoarthritis Cartilage, 16*(5), 584-590. doi:10.1016/j.joca.2007.10.019

Brama, P., TeKoppele, J., Bank, R., Van Weeren, P., & Barneveld, A. (1999). Influence of site and age on biochemical characteristics of the collagen network of equine articular cartilage. *American journal of veterinary research, 60*(3), 341-345.

Brama, P. A. J., Holopainen, J., Weeren, P. R., Firth, E. C., Helminen, H. J., & Hyttinen, M. M. (2009). Influence of exercise and joint topography on depth-related spatial distribution of proteoglycan and collagen content in immature equine articular cartilage. *Equine Veterinary Journal, 41*(6), 557-563. doi:10.2746/042516409x424162

Brandt, K. D., Braunstein, E. M., Visco, D. M., O'Connor, B., Heck, D., & Albrecht, M. (1991). Anterior (Cranial) Cruciate Ligament Transection in the Dog: A Bona Fide Model of Osteoarthritis, Not Merely of Cartilage Injury and Repair. *J Rheumatol, 18*(3), 436-446.

Brandt, K. D., Radin, E. L., Dieppe, P. A., & van de Putte, L. (2006). Yet more evidence that osteoarthritis is not a cartilage disease. *Annals of the Rheumatic Diseases, 65*(10), 1261-1264. doi:10.1136/ard.2006.058347

Brighton, C. T., Kitajima, T., & Hunt, R. M. (1984). Zonal Analysis of Cytoplasmic Components of Articular Cartilage Chondrocytes. *Arthritis and Rheumatism, 27*(11), 1290-1299.

Buckland-Wright, J. C., Macfarlane, D. G., Lynch, J. A., Jasani, M. K., & Bradshaw, C. R. (1995). Joint space width measures cartilage thickness in osteoarthritis of the knee: high resolution plain film and double contrast macroradiographic investigation. *Annals of the rheumatic diseases, 54*(4), 263-268. doi:10.1136/ard.54.4.263

Buckland-Wright, J. C., Macfarlane, D. G., Williams, S. A., & Ward, R. J. (1995). Accuracy and precision of joint space width measurements in standard and macroradiographs of osteoarthritic knees. *Ann Rheum Dis, 54*, 872-880.

Buckwalter, J. A., & Mankin, H. J. (1998a). Articular cartilage repair and transplantation. *Arthritis & Rheumatism, 41*(8), 1331-1342. doi:10.1002/1529-0131(199808)41:8<1331::aid-art2>3.0.co;2-j

Buckwalter, J. A., & Mankin, H. J. (1998b). Articular cartilage: tissue design and chondrocyte-matrix interactions. *Instr Course Lect, 47*, 477-486.

Buckwalter, J. A., Mankin, H. J., & Grodzinsky, A. J. (2005). Articular cartilage and osteoarthritis. *Instr. Course Lect., 54*, 465-480.

Buckwalter, J. A., & Martin, J. (1995). Degenerative Joint Disease. *Clin Symp., 47*(2), 1-32.

Buckwalter, J. A., & Mow, V. C. (1992). Cartilage Repair in Osteoarthritis. In R. W. Moskowitz, D. S. Howell, V. M. Goldberg, & H. J. Mankin (Eds.), *Osteoarthritis: Diagnosis and Medical /Surgical Management.* (2nd ed., pp. 71-107). Philadelphia: W. B. Saunders.

Bullough, P. G., Yawitz, P. S., Tafra, L., & Boskey, A. L. (1985). Topographical variations in the morphology and biochemistry of adult canine tibial plateau articular cartilage. *J Orthop Res, 3*(1), 1-16. doi:10.1002/jor.1100030101

Burstein, D., & Gray, M. L. (2006). Is MRI fulfilling its promise for molecular imaging of cartilage in arthritis? *Osteoarthritis Cartilage, 14*(11), 1087-1090. doi:10.1016/j.joca.2006.07.001

Chang, G., Xia, D., Sherman, O., Strauss, E., Jazrawi, L., Recht, M. P., & Regatte, R. R. (2013). High resolution morphologic imaging and T2 mapping of cartilage at 7 Tesla: comparison of cartilage repair patients and healthy controls. *MAGMA, 26*, 539-548. doi:10.1007/s10334-013-0379-2

Choi, J. A., & Gold, G. E. (2011). MR imaging of articular cartilage physiology. *Magn Reson Imaging Clin N Am, 19*(2), 249-282. doi:10.1016/j.mric.2011.02.010

Collins, N. J., Hart, H. F., & Mills, K. A. G. (2019). Osteoarthritis year in review 2018: rehabilitation and outcomes. *Osteoarthritis and cartilage, 27*(3), 378-391. doi:10.1016/j.joca.2018.11.010

Conaghan, P. (2006). Is MRI useful in osteoarthritis? *Best Pract Res Clin Rheumatol, 20*, 57-68. doi:10.1016/j.berh.2005.08.003

Conaghan, P. G., Felson, D., Gold, G., Lohmander, S., Totterman, S., & Altman, R. (2006). MRI and non-cartilaginous structures in knee osteoarthritis. *Osteoarthritis Cartilage, 14 Suppl A*, A87-94. doi:10.1016/j.joca.2006.02.028

Cook, J. L., Kuroki, K., Visco, D., Pelletier, J. P., Schulz, L., & Lafeber, F. P. (2010). The OARSI histopathology initiative - recommendations for histological assessments of osteoarthritis in the dog. *Osteoarthritis Cartilage, 18 Suppl 3*, S66-S79. doi:10.1016/j.joca.2010.04.017

Dedrick, D. K., Goldstein, S. A., Brandt, K. D., O'Connor, B. L., Goulet, R. W., & Albrecht, M. (1993). A longitudinal study of subchondral plate and trabecular bone in cruciate-deficient dogs with osteoarthritis followed up for 54 months. *Arthritis Rheum, 36*(10), 1460-1467. doi:10.1002/art.1780361019

Deng, B., Wang, F., Yin, L., Chen, C., Guo, L., Chen, H., . . . Yang, L. (2016). Quantitative study on morphology of calcified cartilage zone in OARSI 0∼4 cartilage from osteoarthritic knees. *Curr Res Transl Med, 64*(3), 149-154. doi:10.1016/j.retram.2016.01.009

Disler, D. G., Recht, M. P., & McCauley, T. R. (2000). MR imaging of articular cartilage. *Skeletal Radiology, 29*, 367-377.

Du, J., Carl, M., Bae, W. C., Statum, S., Chang, E. Y., Bydder, G. M., & Chung, C. B. (2013). Dual inversion recovery ultrashort echo time (DIR-UTE) imaging and quantification of the zone of calcified cartilage (ZCC). *Osteoarthritis Cartilage, 21*(1), 77-85.

Du, Y. P., Parker, D. L., Davis, W. L., & Cao, G. (1994). Reduction of partial‐volume artifacts with zero‐filled interpolation in three‐dimensional MR angiography. *J Magn Reson Imaging, 4*, 733-741.

Eckstein, F., Burstein, D., & Link, T. M. (2006). Quantitative MRI of cartilage and bone: degenerative changes in osteoarthritis. *NMR Biomed, 19*(7), 822-854. doi:10.1002/nbm.1063

Eyre, D. R. (1991). The collagens of articular cartilage. *Semin Arthritis Rheum, 21*(3 Suppl 2), 2-11. doi:10.1016/0049-0172(91)90035-x

Fabich, H. T., Sederman, A. J., & Holland, D. J. (2016). Development of ultrafast UTE imaging for granular systems. *J Magn Reson, 273*, 113-123. doi:10.1016/j.jmr.2016.10.016

Farquhar, T., Bertram, J., Todhunter, R., Burton-Wurster, N., & Lust, G. (1997). Variations in composition of cartilage from the shoulder joints of young adult dogs at risk for developing canine hip dysplasia. *Journal of the American Veterinary Medical Association, 210*(10), 1483-1485.

Ficat, C., & Maroudas, A. (1975). Cartilage of the patella. Topographical variation of glycosaminoglycan content in normal and fibrillated tissue. *Annals of the Rheumatic Diseases, 34*(6), 515-519. doi:10.1136/ard.34.6.515

Findlay, D. M., & Kuliwaba, J. S. (2016). Bone-cartilage crosstalk: a conversation for understanding osteoarthritis. *Bone Res, 4*, 16028. doi:10.1038/boneres.2016.28

Flores, R. H., & Hochberg, M. C. (1998). Definition and classification of osteoarthritis. In K. Brandt, M. Doherty, & L. Lohmander (Eds.), *Osteoarthritis* (2nd ed., Vol. 2, pp. 1-12).

Fragonas, E., Mlynarik, V., Jellus, V., Micali, F., Piras, A., Toffanin, R., . . . Vittur, F. (1998). Correlation between biochemical composition and magnetic resonance appearance of articular cartilage. *Osteoarthritis Cartilage, 6*(1), 24-32.

Gold, G. E., Burstein, D., Dardzinski, B., Lang, P., Boada, F., & Mosher, T. (2006). MRI of articular cartilage in OA: novel pulse sequences and compositional/functional markers. *Osteoarthritis Cartilage, 14 Suppl A*, A76-86. doi:10.1016/j.joca.2006.03.010

Gold, G. E., Chen, C. A., Koo, S., Hargreaves, B. A., & Bangerter, N. K. (2009). Recent advances in MRI of articular cartilage. *AJR Am J Roentgenol, 193*(3), 628-638. doi:10.2214/ajr.09.3042

Gray, M. L., Burstein, D., Lesperance, L. M., & Gehrke, L. (1995). Magnetization transfer in cartilage and its constituent macromolecules. *Magn Reson Med, 34*(3), 319-325. doi:10.1002/mrm.1910340307

Greaves, L. L., Gilbart, M. K., Yung, A., Kozlowski, P., & Wilson, D. R. (2009). Deformation and recovery of cartilage in the intact hip under physiological loads using 7T MRI. *J Biomech, 42*(3), 349-354. doi:10.1016/j.jbiomech.2008.11.025

Guermazi, A., Hayashi, D., Eckstein, F., Hunter, D. J., Duryea, J., & Roemer, F. W. (2013). Imaging of osteoarthritis. *Rheum Dis Clin North Am, 39*(1), 67-105. doi:10.1016/j.rdc.2012.10.003

Hall, A. C., Horwitz, E. R., & Wilkins, R. J. (1996). The cellular physiology of articular cartilage. *Exp Physiol, 81*(3), 535-545. doi:10.1113/expphysiol.1996.sp003956

Hannila, I., Raina, S. S., Tervonen, O., Ojala, R., & Nieminen, M. T. (2009). Topographical variation of T2 relaxation time in the young adult knee cartilage at 1.5 T. *Osteoarthritis Cartilage, 17*(12), 1570-1575. doi:10.1016/j.joca.2009.05.011

Hanninen, N., Rautiainen, J., Rieppo, L., Saarakkala, S., & Nissi, M. J. (2017). Orientation anisotropy of quantitative MRI relaxation parameters in ordered tissue. *Sci Rep, 7*(1), 9606. doi:10.1038/s41598-017-10053-2

Hardingham, T. E. (1999). Proteoglycans and glycosaminoglycans. In M. J. Seibel, S. P. Robins, & J. P. Bilezikian (Eds.), *Dynamics of bone and cartilage metabolism* (Vol. 2, pp. 71-80). San Diego: Academic Press.

Huang, M., & Schweitzer, M. E. (2014). The Role of Radiology in the Evolution of the Understanding of Articular Disease. *Radiology, 273*(2S), S1-22.

Huber, M., Trattnig, S., & Lintner, F. (2000). Anatomy, biochemistry, and physiology of articular cartilage. *Invest Radiol, 35*(10), 573-580. doi:10.1097/00004424-200010000-00003

Hunter, D. J., Altman, R. D., Cicuttini, F., Crema, M. D., Duryea, J., Eckstein, F., . . . Gold, G. E. (2015). OARSI Clinical Trials Recommendations: Knee imaging in clinical trials in osteoarthritis. *Osteoarthritis Cartilage, 23*, 698-715. doi:10.1016/j.joca.2015.03.012

Hunter, D. J., Guermazi, A., Lo, G. H., Grainger, A. J., Conaghan, P. G., Boudreau, R. M., & Roemer, F. W. (2011). Evolution of semi-quantitative whole joint assessment of knee OA: MOAKS (MRI Osteoarthritis Knee Score). *Osteoarthritis and cartilage, 19*(8), 990-1002.

Hunter, W. (1743). Of the Structure and Disease of Articulating Cartilages. *Philosophical Transactions, 42*, 514-521.

Hunziker, E. B., Quinn, T. M., & Häuselmann, H. J. (2002). Quantitative structural organization of normal adult human articular cartilage. *Osteoarthritis and Cartilage, 10*(7), 564-572. doi:10.1053/joca.2002.0814

Hwang, W. S., Li, B., Jin, L. H., Ngo, K., Schachar, N. S., & Hughes, G. N. (1992). Collagen fibril structure of normal, aging, and osteoarthritic cartilage. *J Pathol, 167*, 425-433. doi:10.1002/path.1711670413

Jurvelin, J. S., Arokoski, J. P., Hunziker, E. B., & Helminen, H. J. (2000). Topographical variation of the elastic properties of articular cartilage in the canine knee. *J Biomech, 33*(6), 669-675.

Kahn, D., Mittelstaedt, D., Matyas, J., Qu, X., Lee, J. H., Badar, F., . . . Xia, Y. (2016). Meniscus Induced Cartilaginous Damage and Non-linear Gross Anatomical Progression of Early-stage Osteoarthritis in a Canine Model. *The Open Orthopaedics Journal, 10*, 690-705.

Kincaid, S., & Van Sickle, D. (1981). Regional histochemical and thickness variations of adult canine articular cartilage. *American journal of veterinary research*.

Kiviranta, I., Tammi, M., Jurvelin, J., & Helminen, H. J. (1987). Topographical variation of glycosaminoglycan content and cartilage thickness in canine knee (stifle) joint cartilage. Application of the microspectrophotometric method. *J Anat, 150*, 265-276.

Kliger, D. S., Lewis, J. W., & Randall, C. E. (1990a). CHAPTER 2 - Polarization Properties of Light. In D. S. Kliger, J. W. Lewis, & C. E. Randall (Eds.), *Polarized Light in Optics and Spectroscopy* (pp. 9-26). Boston: Academic Press.

Kliger, D. S., Lewis, J. W., & Randall, C. E. (1990b). CHAPTER 3 - Devices for Control of Polarized Light. In D. S. Kliger, J. W. Lewis, & C. E. Randall (Eds.), *Polarized Light in Optics and Spectroscopy* (pp. 27-58). Boston: Academic Press.

Kon, E., Filardo, G., & Marcacci, M. (2011). Early osteoarthritis. *Knee Surgery, Sports Traumatology, Arthroscopy, 20*(3), 399-400. doi:doi:10.1007/s00167-011-1858-5

Koo, S., & Andriacchi, T. P. (2007). A comparison of the influence of global functional loads vs. local contact anatomy on articular cartilage thickness at the knee. *J Biomech, 40*(13), 2961-2966. doi:10.1016/j.jbiomech.2007.02.005

Korvick, D., & Athanasiou, K. (1997). Variations in the mechanical properties of cartilage from the canine scapulohumeral joint. *American journal of veterinary research, 58*(9), 949-953.

Kuo, R., Panchal, M., Tanenbaum, L., & Crues, J. V., 3rd. (2007). 3.0 Tesla imaging of the musculoskeletal system. *J Magn Reson Imaging, 25*(2), 245-261. doi:10.1002/jmri.20815

Kurkijarvi, J. E., Nissi, M. J., Kiviranta, I., Jurvelin, J. S., & Nieminen, M. T. (2004). Delayed Gadolinium-Enhanced MRI of Cartilage (dGEMRIC) and T2 Characteristics of Human Knee Articular Cartilage: Topographical Variation and Relationships to Mechanical Properties. *Magn Reson Med, 52*, 41-46. doi:10.1002/mrm.20104

Lee, J. H., Badar, F., Kahn, D., Matyas, J., Qu, X., Chen, C. T., & Xia, Y. (2014). Topographical variations of the strain-dependent zonal properties of tibial articular cartilage by microscopic MRI. *Connect Tissue Res, 55*(3), 205-216. doi:10.3109/03008207.2014.894997

Lee, J. H., Badar, F., Kahn, D., Matyas, J., Qu, X., & Xia, Y. (2015). Loading-induced changes on topographical distributions of the zonal properties of osteoarthritic tibial cartilage - A study by magnetic resonance imaging at microscopic resolution. *J Biomech, 48*(13), 3634-3642. doi:10.1016/j.jbiomech.2015.08.011

Lee, J. H., Badar, F., Matyas, J., Qu, X., & Xia, Y. (2016). Topographical variations in zonal properties of canine tibial articular cartilage due to early osteoarthritis: a study using 7-T magnetic resonance imaging at microscopic resolution. *Magnetic Resonance Materials in Physics, Biology and Medicine, 29*, 681-690. doi:10.1007/s10334-016-0528-5

Lee, J. H., & Xia, Y. (2013). Quantitative zonal differentiation of articular cartilage by microscopic magnetic resonance imaging, polarized light microscopy, and Fourier-transform infrared imaging. *Microsc Res Tech, 76*(6), 625-632. doi:10.1002/jemt.22209

Ley, C. J., Bjornsdottir, S., Ekman, S., Boyde, A., & Hansson, K. (2016). Detection of early osteoarthritis in the centrodistal joints of Icelandic horses: Evaluation of radiography and low-field magnetic resonance imaging. *Equine Vet J, 48*, 57-64. doi:10.1111/evj.12370

Li, G., Yin, J., Gao, J., Cheng, T. S., Pavlos, N. J., Zhang, C., & Zheng, M. H. (2013). Subchondral bone in osteoarthritis: insight into risk factors and microstructural changes. *Arthritis Res Ther, 15*(6), 223. doi:10.1186/ar4405

Li, X., Benjamin Ma, C., Link, T. M., Castillo, D. D., Blumenkrantz, G., Lozano, J., . . . Majumdar, S. (2007). In vivo T(1rho) and T(2) mapping of articular cartilage in osteoarthritis of the knee using 3 T MRI. *Osteoarthritis Cartilage, 15*, 789-797. doi:10.1016/j.joca.2007.01.011

Liu, F., Chaudhary, R., Block, W. F., Samsonov, A., & Kijowski, R. (2015). Multicomponent T2 analysis of articular cartilage with synovial fluid partial volume correction. *Journal of Magnetic Resonance Imaging, 3*, 197-204.

Mahar, R., Batool, S., Badar, F., & Xia, Y. (2018). Quantitative measurement of T2, T1ρ and T1 relaxation times in articular cartilage and cartilage-bone interface by SE and UTE imaging at microscopic resolution. *Journal of Magnetic Resonance, 297*, 76-85. doi:10.1016/j.jmr.2018.10.008

Mankin, H. J. (1994). Chondrocyte transplantation--one answer to an old question. *N Engl J Med, 331*(14), 940-941. doi:10.1056/NEJM199410063311410

Mankin, H. J., & Buckwalter, J. A. (1996). Restoration of the osteoarthrotic joint. *J Bone Joint Surg Am, 78*(1), 1-2. doi:10.2106/00004623-199601000-00001

Maroudas, A. (1979). Physico-chemical properties of articular cartilage. In M. A. S. Freeman (Ed.), *Adult articular cartilage* (pp. 215-290). Tunbridge Wells: Pitman Medical.

Maroudas, A., Bayliss, M. T., & Venn, M. F. (1980). Further studies on the composition of human femoral head cartilage. *Ann Rheum Dis, 39*(5), 514-523. doi:10.1136/ard.39.5.514

Maroudas, A., & Venn, M. (1977). Chemical composition and swelling of normal and osteoarthrotic femoral head. II. Swelling. *Ann Rheum Dis, 36*(5), 399-406.

Maroudas, A., Wachtel, E., Grushko, G., Katz, E. P., & Weinberg, P. (1991). The effect of osmotic and mechanical pressures on water partitioning in articular cartilage. *Biochim Biophys Acta, 1073*(2), 285-294. doi:10.1016/0304-4165(91)90133-2

Maroudas, A. I. (1976). Balance between swelling pressure and collagen tension in normal and degenerate cartilage. *Nature, 260*(5554), 808-809. doi:10.1038/260808a0

Matyas, J. R., Atley, L., Ionescu, M., Eyre, D. R., & Poole, A. R. (2004). Analysis of cartilage biomarkers in the early phases of canine experimental osteoarthritis. *Arthritis Rheum, 50*(2), 543-552.

Matyas, J. R., Ehlers, P. F., Huang, D., & Adams, M. E. (1999). The early molecular natural history of experimental osteoarthritis. I. Progressive discoordinate expression of aggrecan and type II procollagen messenger RNA in the articular cartilage of adult animals. *Arthritis Rheum, 42*(5), 993-1002.

Matzat, S. J., Kogan, F., Fong, G. W., & Gold, G. E. (2014). Imaging strategies for assessing cartilage composition in osteoarthritis. *Curr Rheumatol Rep, 16*(11), 462. doi:10.1007/s11926-014-0462-3

Matzat, S. J., van Tiel, J., Gold, G. E., & Oei, E. H. (2013). Quantitative MRI techniques of cartilage composition. *Quant Imaging Med Surg, 3*, 162-174. doi:10.3978/j.issn.2223-4292.2013.06.04

Mayerhoefer, M. E., Szomolanyi, P., Jirak, D., Berg, A., Materka, A., Dirisamer, A., & Trattnig, S. (2009). Effects of magnetic resonance image interpolation on the results of texture-based pattern classification: a phantom study. *Investigative radiology, 44*, 405-411.

Mazzuca, S. A., Brandt, K. D., German, N. C., Buckwalter, K. A., Lane, K. A., & Katz, B. P. (2003). Development of radiographic changes of osteoarthritis in the "Chingford knee" reflects progression of disease or non-standardised positioning of the joint rather than incident disease. *Ann Rheum Dis, 62*(11), 1061-1065. doi:10.1136/ard.62.11.1061

McDevitt, C., Gilbertson, E., & Muir, H. (1977). An experimental model of osteoarthritis; early morphological and biochemical changes. *Bone & Joint Journal, 59*(1), 24-35.

McDevitt, C. A. (1973). Biochemistry of articular cartilage. Nature of proteoglycans and collagen of articular cartilage and their role in ageing and in osteoarthritis. *Ann Rheum Dis, 32*(4), 364-378.

Meachim, G. (1971). Effect of age on the thickness of adult articular cartilage at the shoulder joint. *Annals of the rheumatic diseases, 30*(1), 43.

Millington, S. A., Li, B., Tang, J., Trattnig, S., Crandall, J. R., Hurwitz, S. R., & Acton, S. T. (2007). Quantitative and topographical evaluation of ankle articular cartilage using high resolution MRI. *J Orthop Res, 25*(2), 143-151. doi:10.1002/jor.20267

Mitrovic, D., Quintero, M., Stankovic, A., & Ryckewaert, A. (1983). Cell density of adult human femoral condylar articular cartilage. Joints with normal and fibrillated surfaces. *Laboratory investigation; a journal of technical methods and pathology, 49*(3), 309-316.

Mittelstaedt, D., Kahn, D., & Xia, Y. (2016). Topographical and depth-dependent glycosaminoglycan concentration in canine medial tibial cartilage 3 weeks after anterior cruciate ligament transection surgery-a microscopic imaging study. *Quant Imaging Med Surg, 6*(6), 648-660. doi:10.21037/qims.2016.06.12

Mittelstaedt, D., Kahn, D., & Xia, Y. (2018). Detection of early osteoarthritis in canine knee joints 3 weeks post ACL transection by microscopic MRI and biomechanical measurement. *Journal of Orthopaedic Surgery, 26*(2), 2309499018778357.

Mosher, T. J., Walker, E. A., Petscavage-Thomas, J., & Guermazi, A. (2013). Osteoarthritis year 2013 in review: imaging. *Osteoarthritis Cartilage, 21*, 1425-1435. doi:10.1016/j.joca.2013.07.010

Módis, L. (1991). *Organization of the Extracellular Matrix: a Polarization Microscopic Approach*. Boca Raton, Fla: CRC press.

Nakasa, T., Adachi, N., Kato, T., & Ochi, M. (2014). Correlation between subchondral bone plate thickness and cartilage degeneration in osteoarthritis of the ankle. *Foot Ankle Int, 35*(12), 1341-1349. doi:10.1177/1071100714548061

Nemec, U., Oberleitner, G., Nemec, S. F., Gruber, M., Weber, M., Czerny, C., & Krestan, C. R. (2011). MRI versus radiography of acromioclavicular joint dislocation. *American Journal of Roentgenology, 197*, 968-973.

Newbould, R. D., Miller, S. R., Tielbeek, J. A., Toms, L. D., Rao, A. W., Gold, G. E., . . . Brown, A. P. (2012). Reproducibility of sodium MRI measures of articular cartilage of the knee in osteoarthritis. *Osteoarthritis Cartilage, 20*(1), 29-35. doi:10.1016/j.joca.2011.10.007

Newbould, R. D., Miller, S. R., Toms, L. D., Swann, P., Tielbeek, J. A., Gold, G. E., . . . Brown, A. P. (2012). T2* measurement of the knee articular cartilage in osteoarthritis at 3T. *J Magn Reson Imaging, 35*, 1422-1429. doi:10.1002/jmri.23598

Novakofski, K. D., Pownder, S. L., Koff, M. F., Williams, R. M., Potter, H. G., & Fortier, L. A. (2015). High-Resolution Methods for Diagnosing Cartilage Damage In Vivo. *Cartilage, 7*, 39-51. doi:10.1177/1947603515602307

Nykänen, O., Leskinen, H. P., Finnilä, M. A., Karhula, S. S., Turunen, M. J., Töyräs, J., . . . Nissi, M. J. (2020). Bright ultrashort echo time SWIFT MRI signal at the osteochondral junction is not located in the calcified cartilage. *Journal of Orthopaedic Research, 38*(12), 2649-2656.

Oldenbourg, R., & Mei, G. (1995). New polarized light microscope with precision universal compensator. *Journal of microscopy, 180*(2), 140-147.

Pakin, S. K., Cavalcanti, C., La Rocca, R., Schweitzer, M. E., & Regatte, R. R. (2006). Ultra-high-field MRI of knee joint at 7.0T: preliminary experience. *Acad Radiol, 13*(9), 1135-1142. doi:10.1016/j.acra.2006.06.007

Pond, M. J., & Nuki, G. (1973). Experimentally-induced osteoarthritis in the dog. *Ann Rheum Dis, 32*(4), 387-388. doi:10.1136/ard.32.4.387

Radin, E. L., & Rose, R. M. (1986). Role of subchondral bone in the initiation and progression of cartilage damage. *Clinical orthopaedics and related research, 213*, 34-40.

Redler, I., Mow, V., Zimny, M., & Mansell, J. (1975). The ultrastructure and biomechanical significance of the tidemark of articular cartilage. *Clinical orthopaedics and related research*(112), 357-362.

Regatte, R. R., Akella, S. V., Lonner, J. H., Kneeland, J. B., & Reddy, R. (2006). T1rho relaxation mapping in human osteoarthritis (OA) cartilage: comparison of T1rho with T2. *J Magn Reson Imaging, 23*, 547-553. doi:10.1002/jmri.20536

Regatte, R. R., & Schweitzer, M. E. (2007). Ultra-high-field MRI of the musculoskeletal system at 7.0T. *J Magn Reson Imaging, 25*(2), 262-269. doi:10.1002/jmri.20814

Rogers, B. A., Murphy, C. L., Cannon, S. R., & Briggs, T. W. (2006). Topographical variation in glycosaminoglycan content in human articular cartilage. *J Bone Joint Surg Br, 88*(12), 1670-1674. doi:10.1302/0301-620x.88b12.18132

Ross, K. A., Williams, R. M., Schnabel, L. V., Mohammed, H. O., Potter, H. G., Bradica, G., . . . Fortier, L. A. (2012). Comparison of Three Methods to Quantify Repair Cartilage Collagen Orientation. *Cartilage, 4*, 111-120. doi:10.1177/1947603512461440

Seibel, M. J., Robins, S. P., & Bilezikian, J. P. (1999). *Dynamics of bone and cartilage metabolism*. San Diego: Academic Press.

Shao, H., Chang, E. Y., Pauli, C., Zanganeh, S., Bae, W., Chung, C. B., . . . Du, J. (2016). UTE bi-component analysis of T2* relaxation in articular cartilage. *Osteoarthritis Cartilage, 24*(2), 364-373. doi:10.1016/j.joca.2015.08.017

Shao, H., Pauli, C., Li, S., Ma, Y., Tadros, A. S., Chang, E. Y., . . . Du, J. (2017). Magic Angle Effect Plays a Major Role in Both T1rho and T2 Relaxation in Articular Cartilage. *Osteoarthritis Cartilage, 25*(12), 2022-2030. doi:10.1016/j.joca.2017.01.013

Smith, H. E., Mosher, T. J., Dardzinski, B. J., Collins, B. G., Collins, C. M., Yang, Q. X., . . . Smith, M. B. (2001). Spatial variation in cartilage T2 of the knee. *Journal of magnetic resonance imaging, 14*, 50-55.

Spandonis, Y., Heese, F. P., & Hall, L. D. (2004). High resolution MRI relaxation measurements of water in the articular cartilage of the meniscectomized rat knee at 4.7 T. *Magn Reson Imaging, 22*, 943-951. doi:10.1016/j.mri.2004.02.010

Stahl, R., Blumenkrantz, G., Carballido-Gamio, J., Zhao, S., Munoz, T., Hellio Le Graverand-Gastineau, M. P., . . . Link, T. M. (2007). MRI-derived T2 relaxation times and cartilage morphometry of the tibio-femoral joint in subjects with and without osteoarthritis during a 1-year follow-up. *Osteoarthritis Cartilage, 15*, 1225-1234. doi:10.1016/j.joca.2007.04.018

Terukina, M., Fujioka, H., Yoshiya, S., Kurosaka, M., Makino, T., Matsui, N., & Tanaka, J. (2003). Analysis of the thickness and curvature of articular cartilage of the femoral condyle. *Arthroscopy, 19*(9), 969-973.

Torzilli, P. A., Rose, D. E., & Dethmers, D. A. (1982). Equilibrium water partition in articular cartilage. *Biorheology, 19*(4), 519-537. doi:10.3233/bir-1982-19404

Turkiewicz, A., Petersson, I. F., Björk, J., Hawker, G., Dahlberg, L. E., Lohmander, L. S., & Englund, M. (2014). Current and future impact of osteoarthritis on health care: a population-based study with projections to year 2032. *Osteoarthritis and Cartilage, 22*, 1826-1832.

United States Bone and Joint Initiative: The Burden of Musculoskeletal Diseases in the United States (BMUS). (2020). Fourth Edition. Retrieved from http://www.boneandjointburden.org

Urban, J. P. G. (1994). The chondrocyte: A cell under pressure. *Rheumatology, 33*(10), 901-908. doi:10.1093/rheumatology/33.10.901

Venn, M., & Maroudas, A. (1977). Chemical composition and swelling of normal and osteoarthrotic femoral head. I. Chemical Composition. *Ann Rheum Dis, 36*(2), 121-129.

Vignon, E., Piperno, M., Le Graverand, M. P., Mazzuca, S. A., Brandt, K. D., Mathieu, P., . . . Conrozier, T. (2003). Measurement of radiographic joint space width in the tibiofemoral compartment of the osteoarthritic knee: comparison of standing anteroposterior and Lyon schuss views. *Arthritis Rheum, 48*, 378-384. doi:10.1002/art.10773

Wang, N., Badar, F., & Xia, Y. (2015). MRI properties of a unique hypo-intense layer in degraded articular cartilage. *Phys Med Biol, 60*(22), 8709-8721. doi:10.1088/0031-9155/60/22/8709

Wang, N., Badar, F., & Xia, Y. (2018). Experimental Influences in the Accurate Measurement of Cartilage Thickness in MRI. *Cartilage, 10*(3), 278-287. doi:10.1177/1947603517749917

Wang, N., & Xia, Y. (2012). Depth and orientational dependencies of MRI T(2) and T(1rho) sensitivities towards trypsin degradation and Gd-DTPA(2-) presence in articular cartilage at microscopic resolution. *Magn Reson Imaging, 30*(3), 361-370. doi:10.1016/j.mri.2011.10.004

Wang, N., & Xia, Y. (2013). Experimental issues in the measurement of multi-component relaxation times in articular cartilage by microscopic MRI. *J Magn Reson, 235*, 15-25. doi:10.1016/j.jmr.2013.07.001

Wang, Y., Teichtahl, A. J., & Cicuttini, F. M. (2016). Osteoarthritis year in review 2015: imaging. *Osteoarthritis Cartilage, 24*, 49-57. doi:10.1016/j.joca.2015.07.027

Wang, Y.-X. J., Wang, J., Deng, M., Liu, G., & Ling, Q. (2015). In vivo three-dimensional magnetic resonance imaging of rat knee osteoarthritis model induced using meniscal transection. *J Orthop Translat, 3*(3), 134-141. doi:10.1016/j.jot.2015.06.002

Watson, P. J., Carpenter, T. A., Hall, L. D., & Tyler, J. A. (1996). Cartilage swelling and loss in a spontaneous model of osteoarthritis visualized by magnetic resonance imaging. *Osteoarthritis and Cartilage, 4*(3), 197-207. doi:10.1016/S1063-4584(96)80016-1

Wei, B., Zong, M., Yan, C., Mao, F., Guo, Y., Yao, Q., . . . Wang, L. (2015). Use of quantitative MRI for the detection of progressive cartilage degeneration in a mini-pig model of osteoarthritis caused by anterior cruciate ligament transection. *J Magn Reson Imaging, 42*, 1032-1038. doi:10.1002/jmri.24862

Weiss, C., Rosenberg, L., & Helfet, A. J. (1968). An ultrastructural study of normal young adult human articular cartilage. *J Bone Joint Surg Am, 50*(4), 663-674.

Welsch, G. H., Mamisch, T. C., Hughes, T., Zilkens, C., Quirbach, S., Scheffler, K., . . . Trattnig, S. (2008). In vivo biochemical 7.0 Tesla magnetic resonance: preliminary results of dGEMRIC, zonal T2, and T2* mapping of articular cartilage. *Invest Radiol, 43*(9), 619-626. doi:10.1097/RLI.0b013e31817e9122

Welsch, G. H., Mamisch, T. C., Marlovits, S., Glaser, C., Friedrich, K., Hennig, F. F., . . . Trattnig, S. (2009). Quantitative T2 mapping during follow-up after matrix-associated autologous chondrocyte transplantation (MACT): full-thickness and zonal evaluation to visualize the maturation of cartilage repair tissue. *J Orthop Res, 27*, 957-963. doi:10.1002/jor.20835

Wenham, C. Y. J., & Conaghan, P. G. (2013). New horizons in osteoarthritis. *Age and Ageing, 42*(3), 272-278. doi:10.1093/ageing/aft043

Wyatt, C., Guha, A., Venkatachari, A., Li, X., Krug, R., Kelley, D. E., . . . Majumdar, S. (2015). Improved differentiation between knees with cartilage lesions and controls using 7T relaxation time mapping. *Journal of Orthopaedic Translation, 3*(4), 197-204. doi:10.1016/j.jot.2015.05.003

Xia, Y. (1998). Relaxation anisotropy in cartilage by NMR microscopy (uMRI) at 14-micron. *Magn Reson Med, 39*(6), 941-949.

Xia, Y. (2000a). Heterogeneity of cartilage laminae in MR imaging. *J Magn Reson Imaging, 11*(6), 686-693.

Xia, Y. (2000b). Magic-Angle Effect In Magnetic Resonance Imaging Of Articular Cartilage: A Review. *Invest Radiol, 35*(10), 602-621.

Xia, Y. (2003). The Total Volume and the Complete Thickness of Articular Cartilage Determined by MRI. *Osteoarthritis Cartilage, 11*, 473-474.

Xia, Y. (2005). Averaged Properties of Articular Cartilage from Multidisciplinary Microscopic Imaging Study. *Conf Proc IEEE Eng Med Biol Soc, 3*, 3161-3164.

Xia, Y. (2007). Resolution 'Scaling Law' in MRI of Articular Cartilage. *Osteoarthritis Cartilage, 15*(4), 363–365.

Xia, Y. (2008). Averaged and depth-dependent anisotropy of articular cartilage by microscopic imaging. *Semin Arthritis Rheum, 37*(5), 317-327. doi:10.1016/j.semarthrit.2007.07.001

Xia, Y., Farquhar, T., Burton-Wurster, N., & Lust, G. (1997). Origin Of Cartilage Laminae In MRI. *J Magn Reson Imaging, 7*(5), 887-894.

Xia, Y., Moody, J. B., & Alhadlaq, H. (2002). Orientational dependence of T2 relaxation in articular cartilage: A microscopic MRI (microMRI) study. *Magn Reson Med, 48*(3), 460-469. doi:10.1002/mrm.10216

Xia, Y., Moody, J. B., Alhadlaq, H., Burton-Wurster, N., & Lust, G. (2002). Characteristics of topographical heterogeneity of articular cartilage over the joint surface of a humeral head. *Osteoarthritis Cartilage, 10*(5), 370-380. doi:10.1053/joca.2002.0523

Xia, Y., Moody, J. B., Alhadlaq, H., & Hu, J. (2003). Imaging the physical and morphological properties of a multi-zone young articular cartilage at microscopic resolution. *J Magn Reson Imaging, 17*(3), 365-374. doi:10.1002/jmri.10269

Xia, Y., Moody, J. B., Burton-Wurster, N., & Lust, G. (2001). Quantitative in situ correlation between microscopic MRI and polarized light microscopy studies of articular cartilage. *Osteoarthritis Cartilage, 9*(5), 393-406. doi:10.1053/joca.2000.0405

Xia, Y., Wang, N., Lee, J., & Badar, F. (2011). Strain-dependent T1 relaxation profiles in articular cartilage by MRI at microscopic resolutions. *Magn Reson Med, 65*(6), 1733-1737. doi:10.1002/mrm.22933

Xia, Y., Zheng, S., Szarko, M., & Lee, J. (2012). Anisotropic properties of bovine nasal cartilage. *Microsc Res Tech, 75*(3), 300-306. doi:10.1002/jemt.21058

Zernia, G., & Huster, D. (2006). Collagen dynamics in articular cartilage under osmotic pressure. *NMR Biomed, 19*(8), 1010-1019. doi:10.1002/nbm.1061

Zheng, S., & Xia, Y. (2009a). Effect of phosphate electrolyte buffer on the dynamics of water in tendon and cartilage. *NMR Biomed, 22*(2), 158-164. doi:10.1002/nbm.1294

Zheng, S., & Xia, Y. (2009b). Multi-components of T2 relaxation in ex vivo cartilage and tendon. *J Magn Reson, 198*(2), 188-196.

Zheng, S., Xia, Y., & Badar, F. (2011). Further studies on the anisotropic distribution of collagen in articular cartilage by μMRI. *Magn Reson Med, 65*(3), 656-663. doi:10.1002/mrm.22648

Zhuang, Z., Lee, J. H., Badar, F., Xu, J., & Xia, Y. (2016). The influences of different spatial resolutions on the characteristics of T2 relaxation times in articular cartilage: A coarse-graining study of the microscopic magnetic resonance imaging data. *Microsc Res Tech, 79*, 754-765. doi:10.1002/jemt.22694

Zimny, M. L., & Redler, I. (1974). Morphological variations within a given area of articular surface of cartilage. *Zeitschrift für Zellforschung und Mikroskopische Anatomie, 147*(2), 163-167.

LIST OF PUBLICATIONS

Chapters four, five, and six in this dissertation are based on the following published articles referred by their Roman numerals respectively:

I **F Badar**, Y Xia, "Image interpolation improves the zonal analysis of cartilage T2 relaxation in MRI" *Quantitative Imaging in Medicine and Surgery*, 7(2): 227-37 (2017).

II **F Badar**, JH Lee, X Qu, Y Xia, "Topographical and zonal patterns of T2 relaxation in osteoarthritic tibial cartilage by low-and high-resolution MRI" *Magnetic Resonance Imaging*, 78: 98-108 (2021).

III **F Badar**, Y Xia, "The Interface Region between Articular Cartilage and Bone by μMRI and PLM at Microscopic Resolutions" *Microscopy Research & Technique*, (2021).

The original articles have been reproduced with permission of the copyright holders. The dissertation contains also some previously unpublished data.

RELATED WORK

The author has also contributed to the following published work:

1 Xia Y, Alhadlaq H, Ramakrishnan N, Bidthanapally A, **Badar F**, Lu M. Molecular and morphological adaptations in compressed articular cartilage by polarized light microscopy and Fourier-transform infrared imaging. *J Struct Biol* 164(1):88-95 (2008)

2 Zheng S, Xia Y, Bidthanapally A, **Badar F**, Ilsar I, Duvoisin N. Damages to the extracellular matrix in articular cartilage due to cryopreservation by microscopic magnetic resonance imaging and biochemistry. *Magnetic Resonance Imaging* 27(5):648-655 (2009)

3 Cicek E, **Badar F**, Li J, Tian X, Xia Y. Morphological changes of chondrocytes in compressed articular cartilage using polarized light microscopy. *Bioinformatics and Biomedical Engineering (iCBBE), 2010 4th International Conference on IEEE* :1-4 (2010)

4 Xia Y, Wang N, Lee J, **Badar F**. Strain-dependent T1 relaxation profiles in articular cartilage by MRI at microscopic resolutions. *Magn Reson Med* 65(6):1733-1737 (2011)

5 Zheng S, Xia Y, **Badar F**. Further studies on the anisotropic distribution of collagen in articular cartilage by μMRI. *Magn Reson Med* 65(3):656-663 (2011)

6 Lee JH, **Badar F**, Kahn D, et al. Topographical variations of the strain-dependent zonal properties of tibial articular cartilage by microscopic MRI. *Connect Tissue Research* 55(3):205-216 (2014)

7 Lee JH, **Badar F**, Kahn D, Matyas J, Qu X, Xia Y. Loading-induced changes on topographical distributions of the zonal properties of osteoarthritic tibial cartilage - A study by magnetic resonance imaging at microscopic resolution. *J Biomech* 48(13):3634-3642 (2015)

8 Wang N, **Badar F**, Xia Y. MRI properties of a unique hypo-intense layer in degraded articular cartilage. *Phys Med Biol* 60(22):8709-8721 (2015)

9 Wang N, Kahn D, **Badar F**, Xia Y. Molecular origin of a loading-induced black layer in the deep region of articular cartilage at the magic angle. *J Magn Reson Imaging* 41(5):1281-1290 (2015)

10 Lee JH, **Badar F**, Matyas J, Qu X, Xia Y. topographical Variations of the zonal properties of canine tibial articular cartilage due to early osteoarthritis – a study by 7t magnetic resonance imaging at microscopic resolution. *Magnetic Resonance Materials in Physics, Biology and Medicine* 29(4):681-690 (2016)

11 Xia Y, Momot K.I., Chen Z, Chen C.T., Kahn D, **Badar F**, CHAPTER 1: Introduction to Cartilage, in *Biophysics and Biochemistry of Cartilage by NMR and MRI*: 1-43 (2016)

12 Zhuang Z, Lee JH, **Badar F**, Xu J, Xia Y. The influences of different spatial resolutions on the characteristics of T2 relaxation times in articular cartilage: A coarse-graining study of the microscopic magnetic resonance imaging data. *Microscopy Research and Technique* 79(8):754-765 (2016)

13 Jia H, Ma X, Tong W, Doyran B, Sun Z, Wang L, Zhang X, Zhou Y, **Badar F**, Chandra A, Lu X, Xia Y, Han L, Enomoto-Iwamoto M, Qin L. EGFR signaling is critical for maintaining the superficial layer of articular cartilage and preventing osteoarthritis initiation. *Proceedings of the National Academy of Sciences* 2016;113 (50):4360-14365.

14 Kahn D, Mittelstaedt D, Matyas J, Qu X, Lee JH, **Badar F**, Les C, Zhuang Z, Xia Y. meniscus induced cartilaginous damage and non-linear gross anatomical progression of early-stage osteoarthritis in a canine model. *The Open Orthopaedics Journal* 10: 690-705 (2016).

15 Jia H, Ma X, Wei Y, Tong W, Tower RJ, Chandra A, Wang L, Sun Z, Yang Z, **Badar F**, Zhang K, Tseng W, Kramer I, Kneissal M, Xia Y, Liu X. S, James H. C. W, Han L, Enomoto-Iwamoto M, Qin L. loading-induced reduction in sclerostin as a mechanism of subchondral bone plate sclerosis in mouse knee joints during late-stage osteoarthritis. *Arthritis & Rheumatology* 70 (2):230-241 (2018)

16 Wang N, **Badar F**, Xia Y. Compressed sensing in quantitative determination of GAG concentration in cartilage by microscopic MRI. *Magn Reson Med* 79(6): 3163-3171 (2018)

17 Mahar R, Batool S, **Badar F**, Xia Y. Quantitative measurement of T2, T1ρ and T1 relaxation times in articular cartilage and cartilage-bone interface by SE and UTE imaging at microscopic resolution. *J Magn Reson* 297:76-85 (2018)

18 Wang N, **Badar F**, Xia Y. Experimental Influences in the Accurate Measurement of Cartilage Thickness in MRI. *Cartilage* 10(3):278-287 (2019)

19 Batool S, Mahar R, **Badar F**, Tetmeyer A, Xia Y. Quantitative μMRI and PLM study of rabbit humeral and femoral head cartilage at sub-10 μm resolutions. *Journal of Orthopaedic Research* 38(5): 1052-1062 (2020)

20 Wang N, **Badar F**, Xia Y. Resolution-dependent influences of compressed sensing in quantitative T2 mapping of articular cartilage. *NMR in Biomedicine* 33(12): e4260 (2020)

21 Mantebea H, Batool S, Singh A, Hammami M, **Badar F**, Xia Y. Structural differences between immature and mature articular cartilage of rabbits by microscopic MRI and polarized light microscopy. *Journal of Anatomy* (2022)

22 Batool S, Hammami M, Mantebea H, **Badar F**, Xia Y. Location-Specific Study of Young Rabbit Femoral Cartilage by Quantitative μMRI and Polarized Light Microscopy *Cartilage* (2022)